

Universität
Rostock



Traditio et Innovatio

Nonclassical Light from Semiconductor Micro- and Nanostructures

Dissertation

zur

Erlangung des akademischen Grades

doctor rerum naturalium (Dr. rer. nat.)

der Mathematisch-Naturwissenschaftlichen Fakultät

der Universität Rostock

vorgelegt von

Dipl.-Phys. Peter Grünwald, geboren am 23.09.1985 in Rostock

Gutachter: 1.) Prof. Dr. Werner Vogel,
Universität Rostock
2.) Prof. Dr. Mackillo Kira,
Philipps-Universität Marburg

Datum der Einreichung: 28.02.2014

Datum der Verteidigung: 14.07.2014

Selbstständigkeitserklärung

Hiermit erkläre ich an Eides statt, dass ich die hier vorliegende Dissertation selbstständig und ohne fremde Hilfe verfasst habe, bis auf die in der Bibliographie angegebenen Quellen keine weiteren Quellen benutzt habe und die den Quellen wörtlich oder inhaltlich entnommenen Stellen als solche kenntlich gemacht habe.

Peter Grünwald

Rostock, den _____

Acknowledgements. I wish to thank Prof. Werner Vogel (Theoretical Quantum Optics Group) and Prof. Heinrich Stolz (Semiconductor Optics Group, both University of Rostock) for giving me the opportunity to study the quantum-optical phenomena of semiconductor light sources. Many discussions helped me a great deal to understand the physics of this complex topic as well as to appreciate the theoretical and experimental efforts connected to it. From the the experimental side, I want to thank, in particular, Dr. Gerolf K. G. Bura and Thomas Ahrens, who provided experimental data on the different structures under study. Likewise, I am grateful for the theoretical discussions on solid-state physics with Dr. Günter Manzke, Dr. Felix Richter, Dr. Dirk Semkat, and Siegfried Sobkowiak. I want to thank all the colleagues of the Theoretical Quantum Optics group in Rostock, with whom I had the pleasure to work with: Dr. Christian Di Fidio, Dr. Dmytro Vasyliev, Dr. Evgeny Shchukin, Dr. Andrii Seminov, Dr. Shailendra Kr. Singh, Dr. Thomas Kiesel, Dr. Jan Sperling, Elizabeth Agudelo, Melanie Mraz, Falk Töppel, Frank E. S. Steinhoff, Saleh Rahimi-Keshari, and Farid Shahandeh. Last but not least, I am deeply thankful to my family for supporting me before and throughout the time of this thesis.

This work has been supported by the Deutsche Forschungsgemeinschaft through SFB 652.

Abstract. Nonclassical light is characterized by explicit quantum properties. These properties are very interesting for many applications in future quantum technologies. Semiconductor micro- and nanostructures, where excitons form the dipole coupling to the electromagnetic fields, are seen as a possible source for nonclassical light. However, their quantum theoretical description is complicated due to the many-body nature of the considered system. This thesis studies the quantum properties of the light emitted from different semiconductor structures.

A single exciton in a quantum dot acts similar to an atom. However, it is subject to multiple environmental effects, such as incoherent pumping and phonon-induced dephasing. Including these environmental effects, the emitted fields from a quantum dot are theoretically obtained and studied. Inside a cavity of intermediate coupling, the fluorescence light of the quantum dot is squeezed, and this squeezing is exceptionally robust against the dissipative influence of the semiconductor material.

In a quantum well, multiple interacting excitons act as a single bosonic particle with a nonlinear coupling. Due to the spectral broadness of the exciton spectrum, the emission-fields of the quantum well are also connected to the absorption of the medium. Combining both aspects of light generation, experimentally determined spectra of a given well are interpreted. The description allows one to calculate arbitrary quantum correlations of both the exciton and the quantum-well emission. Different nonclassical features are revealed.

In the experiments, the broad emission spectrum of the semiconductor structures necessitates the filtering of the fields before they are analyzed. The filtering changes the fields drastically and, therefore, has to be taken into account to describe the detected fields correctly. A general overview on the theory of filtering quantum fields is given.

Zusammenfassung. Nichtklassisches Licht ist charakterisiert durch eindeutige Quanteneigenschaften. Diese Eigenschaften sind hochinteressant für viele Anwendungen in künftigen Quantentechnologien. Halbleiter Mikro- und Nanostrukturen, in welchen Exzitonen die an elektromagnetische Lichtfeld koppelnden Dipole formen, werden als eine mögliche Quelle für nichtklassisches Licht angesehen. Allerdings ist ihre quantentheoretische Beschreibung aufgrund der Vielteilchennatur des betrachteten Systems kompliziert. Diese Dissertation untersucht die Quanteneigenschaften von Licht, welches von verschiedenen Halbleiterstrukturen emittiert wird.

Ein einzelnes Exziton in einem Quantenpunkt verhält sich ähnlich zu einem Atom. Allerdings ist es zusätzlich vielen Umgebungseinflüssen ausgesetzt, wie inkohärentes Pumpen und Phononen-induzierte Dephasierung. Unter Berücksichtigung dieser Umgebungseinflüsse werden die emittierten Felder eines Quantenpunktes theoretisch gewonnen und studiert. Innerhalb eines Resonators mit mittelstarker Kopplung ist das Fluoreszenzlicht des Quantenpunktes gequetscht, und diese Quetschung ist außergewöhnlich stabil gegen dissipative Einflüsse des Halbleitermaterials.

In einem Quantenfilm verhalten sich viele Exzitonen wie ein kollektives bosonisches Teilchen mit einer nichtlinearen Kopplung. Aufgrund der spektralen Breite des Exzitonenspektrums sind die Emissionsfelder des Quantenfilms auch an die Absorption des Mediums gekoppelt. Indem beide Aspekte der Lichterzeugung kombiniert werden, können experimentell bestimmte Spektren eines gegebenen Quantenfilms interpretiert werden. Die Beschreibung erlaubt es, beliebige Quantenkorrelationen sowohl von der Exzitonen- als auch der Quantenfilmemission zu berechnen. Verschiedene nichtklassische Effekte werden dabei sichtbar.

Im Experiment macht das breite Emissionsspektrum der Halbleiterstrukturen eine Filterung der Felder vor deren Analyse notwendig. Die Filterung verändert die Felder drastisch und muss daher berücksichtigt werden, um die detektierten Felder korrekt zu beschreiben. Es wird ein allgemeiner Überblick zur Theorie der Filterung in Quantenfeldern gegeben.

Contents

Introduction	13
1. Excitons	17
1.1. Excitons as bound electron-hole states	18
1.2. Multi-exciton systems	19
2. Quantum dots in semiconductor microcavities	23
2.1. Raman-assisted Rabi resonances in quantum-dot-cavity systems	25
2.1.1. Spontaneous emission from an excited quantum dot	25
2.1.2. Phonon-assisted Rabi flipping	26
2.1.3. Two-mode cavity	27
2.1.4. Dynamics of Raman-assisted Rabi resonances	29
2.1.5. Spectral properties of the external field	31
2.2. Squeezing of quantum-dot fluorescence	34
2.2.1. Fluorescence of quantum dots in cavities	34
2.2.2. Nonclassical light from single-photon emitters	36
2.2.3. Squeezing of single-photon-emitter fluorescence	37
2.2.4. Cavity induced purification	40
2.2.5. Approximate analytical description	43
2.2.6. Stability against dissipative environments	45
2.2.7. A method for observing single-photon-emitter-fluorescence squeezing	51
3. Excitons in quantum wells	55
3.1. Experiments on the multiple-quantum-well sample	55
3.2. Theoretical description of emission spectra	59
3.2.1. Exciton Hamiltonian	59
3.2.2. Input-output formalism and quantum-well-emission spectrum . . .	61
3.2.3. Superfluorescence of the quantum well	65
3.3. Quantum correlations	67
3.3.1. General correlations	67
3.3.2. Examples of correlations	69

4. Filtering of broadband light fields	75
4.1. Spectrally filtered light	75
4.1.1. Spectral filtering of light with a single filter	76
4.1.2. Spectral filtering of light with two filters	79
4.2. Photocurrent filtering	81
4.2.1. Photocurrent filtering with one filter frequency	81
4.2.2. Filtered current using two filter frequencies	83
5. Conclusions	87
5.1. Summary	87
5.2. Outlook	88
Appendix	91
A. Publications and Conference Contributions	93
A.1. List of own Publications	93
A.2. Conference Contributions	94

List of Abbreviations

cw	-	continuous wave
rf	-	radio frequency
<hr/>		
AIAs	-	aluminium arsenide
GaAs	-	gallium arsenide
<hr/>		
CCD	-	charge-coupled device
ES	-	exciton spot
FWHM	-	full width half maximum
PARR	-	phonon-assisted Rabi resonance
QED	-	quantum electrodynamics
RARR	-	Raman-assisted Rabi resonance
SPE	-	single-photon emitter
TLS	-	two-level system

List of Figures

2.1. Vibronic Structure	28
2.2. Occupation Probabilities for Raman-Resonance and RARR	30
2.3. Emission probabilities of the decay channels	32
2.4. Spontaneous emission of cavity in Raman resonance and RARR	34
2.5. Cavity-SPE Setup	41
2.6. Parameters of the SPE in free-space and the optimized cavity	42
2.7. Purification rate for different dephasings	47
2.8. Squeezing for different dephasings	48
2.9. Squeezing for different incoherent quantum-dot pumpings	49
2.10. Squeezing for different incoherent cavity pumpings	51
2.11. Homodyne cross-correlation setup	52
3.1. Structure and spatial intensity distribution of the quantum well probe . . .	57
3.2. Experimental Fluorescence Spectra	57
3.3. Spectrum: Excitons and Quantum Well	63
3.4. Fluorescence Spectra: Theory and Experiment	64
3.5. Coherence and intensity of exciton- and quantum-well emission	70
3.6. Squeezing of exciton- and quantum-well emission	71
3.7. $g^{(2)}(0)$ of exciton emission	72
4.1. Four-detector correlation setup	76
4.2. Four-detector spectral setup, with two frequencies	79
4.3. Four-detector setup currents	81
4.4. Four-detector setup currents, with two frequencies	84

Introduction

Quantum electromagnetic fields, whose properties cannot be described with Maxwell's classical field theory, are called nonclassical light fields. Sudarshan and Glauber formalized this notion in 1963 [1, 2], based on the close analogy of coherent states to classical field modes. The study of these nonclassical properties has become a focus of research. Photon-antibunching, one of the first nonclassical light features to be discussed in theory [3, 4] and shown in experiments [5], can be seen as a direct proof for the existence of the photon. Likewise, the strong light-matter coupling of atoms with lasers [6, 7] and cavity-field modes [8] unsettled the classical notion, that light and matter would always be separated entities. Instead, in these systems, a combined quantum state emerges with properties not given for either emitter or photon. Besides these examples of fundamental quantum physics, different kinds of nonclassical states of light have become irreplaceable for applications. Squeezed light, where the quantum fluctuations are below the shot noise level, is used to increase the sensitivity of interferometric measurements, such as the gravitational wave detector GEO600 at Hanover [9]. Another important example of nonclassical states of light are the entangled states, where two or more different subsystems are correlated [10, 11]. Entangled states are at the basis of quantum communication and quantum information processing.

Due to the plethora of phenomena and potential applications for nonclassical light, sources for such light are of particular interest. The strong squeezing in the gravitational wave detector is generated by sending a classical light source through a nonlinear medium [12]. Single atoms or molecules provide very good nonclassical light sources, as they only emit single photons at a time. They are isolated and thus relatively simple to describe in theory, and can be adjusted in ion traps. In optical cavities, their emission has shown antibunching and sub-Poisson photo statistics [13, 14]. Multiple atoms also emit squeezed light in different scenarios [15, 16], while a single atom was predicted to emit squeezed light [17]. However, these systems are limited by their fixed system parameters. Especially atoms suffer from the fact, that only a certain amount of different atoms or molecules exist with given properties like, e.g., resonance frequency, natural linewidth, dipole moment. In general, no atom is 'perfect' as a source for any specific kind of nonclassical light. Similarly, each nonlinear crystal has a specific reaction to incoming light

fields.

A possible solution for the limited variety of established sources of nonclassical light are artificial atoms and in particular excitons in semiconductors. Excitons are bound states of an electron and a hole in an excited semiconductor. For the time of their existence, they constitute a dipole allowing interaction with photons. In semiconductors with a direct band gap, this interaction is dominant, as applied in LEDs. The internal parameters and dynamics of excitons are governed by the semiconductor material, the level of confinement and excitation (exciton-density), temperature of the sample, roughness of the materials boundaries, and many others. Hence, these parameters even for a given semiconductor sample are variable and can be tailored to suit the needs for applications.

The versatility of excitons made them an interesting topic for research on nonclassical light sources. Quantum dots, where excitons are confined in all dimensions, were already shown to emit antibunched light and have a sub-Poisson photo statistics [18, 19, 20, 21]. Also in quantum dots in cavities strong light-matter coupling was achieved in a few systems [22, 23, 24, 25]. Semiconductor lasers emit weakly squeezed light [26, 27].

As stated above, exciton dynamics are sensitive to environmental influences of all kinds. While this can be used to tailor the emission fields, it also implies, that any realistic description of excitons needs to incorporate these influences. For example, a quantum dot in a semiconductor medium may be subject not only to the spontaneous emission of an atom, but also radiationless dephasing and incoherent pumping [28]. This can be caused by phonons, whose density is dependent both on the excitation of the quantum dot, and the temperature of the medium. They may also lead to new resonances when the coupling to the quantum dot is sufficiently strong.

This thesis deals with the quantum optical properties of light fields emitted from semiconductor micro- and nanostructures. For this purpose two major questions will be addressed. What are the emitted quantum fields from these structures, and what quantum (nonclassical) features do they possess? The results of this work are given in the published articles [I-V], as well as two articles in preparation [VI,VII]. The published articles are attached at the end of the thesis.

In Chap. 1, we motivate the quantum-optical exciton models, which will be used in the later chapters. Chaps. 2 and 3 are dedicated to the study of exciton emission fields in different systems and their quantum-optical properties. In Chap. 2, quantum dots in semiconductor microcavities are analyzed. In the first part we study the active influence of a phonon based on a model of an atom with an electronic and a vibronic degree of freedom in a two-mode cavity. In the second part of the chapter, the resonance fluorescence of quantum dots is analyzed with respect to the question of optimization of squeezing. The subsequent Chap. 3, considers quantum wells and, in particular, a quantum well which was

studied in the experimental Group of Prof. Stolz. We analyze the fluorescence spectrum of the excitons, combining the Hamiltonian of the excitons with quantum optical methods for light fields propagating through the medium for the interpretation of the experimental spectra. Furthermore, based on these findings we are able to compute the quantum optical properties of the exciton- and the quantum-well emission. Chap. 4 deals with the filtering of quantum fields. The broadband nature of the emission fields requires the fields to be spectrally filtered at some point. The filtering procedure heavily influences the quantum fields, so that the detected fields have to be calculated as functionals of the actual signal fields and the filter response. Finally, in Chap. 5, a brief outlook on further research in the discussed topics is given.

1. Excitons

In classical electrodynamics, electromagnetic fields emitted from condensed matter systems are described by the polarization P (projected onto the direction of detection) of the medium. In quantum optics, these fields are represented by so called source fields \hat{E}_s . In general, they are not equal to the overall fields \hat{E} , as the source-field operators do not fulfill the canonical commutation relations of the quantized electromagnetic fields, see e.g. [29]. The full field \hat{E} is a sum of the source fields and free fields \hat{E}_f to ensure the commutation relation. Free fields are generators of quantum noise, for example in amplifying structures, see [30] for details. The relation between free- and source-field correlations will become relevant in the later chapters.

In case of a non-dispersive, non-absorbing medium, the Maxwell equations can be quantized directly. If dispersion and absorption are taken into account on the other hand, quantum noise sources have to be included [31, 32], which are coupled to the polarization of the medium. From a quantum point of view, these noise sources are represented by resonances of the medium, its constituent particles or quasiparticles, absorbing and emitting photons. In strong light-matter-coupling systems, the photons and the resonances form dressed states, so-called polaritons. The main sources of light emitted from excited semiconductor micro- and nanostructures are excitons. In the following the general conceptions of these bound electron-hole states shall be shortly discussed. The focus is on obtaining the relevant Hamiltonian components for excitons in different structures. This allows a first analysis of the exciton dynamics, which also governs the source part of the emitted fields [28]. In contrast to elementary particles which obey either fermion or boson statistics, excitons, composed of two fermions, may have complicated commutation relations. Depending on the level of excitation and localization (or, equivalently, density), they experience a plethora of different regimes, including the atom-like multi-level structure, in case of resonant pumping a fermionic two-level system, a low-density bosonic behavior [33] (and possibly a Bose-Einstein-condensate [34, 35]), and the dissolving of excitons into an electron-hole plasma due to the Mott-effect [36, 37]. The cases of a two-level system and low-density bosonic behavior with interaction will be considered in Chaps. 2, and 3, respectively.

1.1. Excitons as bound electron-hole states

The periodic alignment of atoms in regular crystals (in semiconductors) provides the well-known band structure. Relevant for the discussion are the valence band, the band of highest energy, which is fully occupied by the electrons; and the conduction band, the lowest unoccupied band. The energy difference between the two bands, the band gap, is crucial to the electronic conduction properties. In case of semiconductors, it is usually of the order of 1 eV. Due to environmental influences, such as light irradiation (a photon of wavelength $\lambda = 615$ nm has an energy of 2.00 eV), an electron may overcome the band gap and fill an empty state in the conduction band. At the same time a hole state is generated in the valence band, where the electron has been. A current is generated in the semiconductor, which is the fundamental principle in diodes and transistors.

As long as an electron is in the conduction band, a polarization between the electron and the corresponding hole arises forming a dipole, with a negative (electron) and a positive (hole) charge of amplitude e . This bound state is called Wannier-Mott exciton. Similar polarization structures in molecules, called Frenkel-excitons, will not be discussed here. Hence, we call Wannier-Mott excitons just excitons from now on. For the purpose of describing the dynamics of the exciton, we consider the time-independent Schrödinger equation for the polarization eigenstates, given by [38]

$$E|\psi\rangle = \left[\frac{\hat{p}^2}{2m_X} - \frac{e^2}{4\pi\epsilon_0\hat{r}} \right] |\psi\rangle = \hat{H}|\psi\rangle. \quad (1.1)$$

Herein m_X is the effective exciton mass and \hat{r} represents the relative distance between electron and hole. Equation (1.1) is called Wannier-equation. Comparing with standard quantum mechanics reveals, that the structure of the polarization eigenstates is identical to that of the energy eigenstates of the hydrogen-atom, see e.g. [39, 40]. The main difference is the mass, which scales the parameters of the system (Bohr radius, Rydberg energy, etc.). However, in contrast to the well defined three dimensional hydrogen atom, excitons can be confined in different dimensions. Therefore the structure of the operators varies and with it the specific energy eigenvalues. For example, in two dimensions (quantum well) the 1s energy of the exciton is four times as high as in the three dimensional case [38]. Hence, when comparing different quantum wells with decreasing thickness, the resonance energy of the exciton should increase, as observed in [41].

For each energy level λ with energy $\hbar\omega_\lambda$ of an exciton with momentum \vec{K} , creation and annihilation operators, $\hat{B}_{\lambda,\vec{K}}^\dagger$ and $\hat{B}_{\lambda,\vec{K}}$, respectively, can be defined [38]. In all scenarios discussed here, the excitons are well localized, thus having a negligible momentum, and we omit the index \vec{K} . With the exciton creation- and annihilation operators, a kinetic

Hamiltonian for a single exciton can be given as

$$\hat{H}_{\text{kin}} = \hbar \sum_{\lambda} \omega_{\lambda} \hat{B}_{\lambda}^{\dagger} \hat{B}_{\lambda}. \quad (1.2)$$

For the purpose of simplicity we omit the vacuum term $\hbar\omega_0$, such that $\hbar\omega_{\lambda}$ is actually the difference from the state λ to the vacuum. Furthermore, as the excitons have a dipole moment, they also have, at least, a dipolar coupling to an incoming laser field with a pumping Hamiltonian

$$\hat{H}_{\text{pump}} = \hbar \sum_{\lambda} \left(\Omega_{\text{R},\lambda} e^{-i\omega_{\text{L}}t} \hat{B}_{\lambda}^{\dagger} + \Omega_{\text{R},\lambda}^* e^{i\omega_{\text{L}}t} \hat{B}_{\lambda} \right), \quad (1.3)$$

where ω_{L} is the laser frequency, and $\Omega_{\text{R},\lambda} \propto \vec{d}_{\lambda} \cdot \vec{E}_{\text{L}}$ is the Rabi frequency of the laser field coupling to an exciton on level λ . We will only consider cw-single-mode laser fields, so that $\Omega_{\text{R},\lambda}$ is time-independent. The Rabi frequency is proportional to the dipole moment \vec{d}_{λ} of the exciton being excited to this state and the amplitude of the laser field \vec{E}_{L} . Going into the rotating frame of the laser frequency ω_{L} , we can write the full single-exciton Hamiltonian as

$$\hat{H}_{\text{exc}} = \hat{H}_{\text{kin}} + \hat{H}_{\text{pump}} = \hbar \sum_{\lambda} \delta_{\lambda} \hat{B}_{\lambda}^{\dagger} \hat{B}_{\lambda} + \hbar \sum_{\lambda} \left(\Omega_{\text{R},\lambda} \hat{B}_{\lambda}^{\dagger} + \Omega_{\text{R},\lambda}^* \hat{B}_{\lambda} \right), \quad (1.4)$$

with $\delta_{\lambda} = \omega_{\lambda} - \omega_{\text{L}}$. In most cases, the different levels λ are spectrally far separated, and only a single level ζ may be reasonably excited by the laser. In that case, applying the rotating wave approximation, we are limited to

$$\hat{H}_{\text{exc}} = \hbar \delta_{\zeta} \hat{B}_{\zeta}^{\dagger} \hat{B}_{\zeta} + \hbar \Omega_{\text{R},\zeta} \hat{B}_{\zeta}^{\dagger} + \hbar \Omega_{\text{R},\zeta}^* \hat{B}_{\zeta}. \quad (1.5)$$

In an atom, each energy level can be occupied only once, as they are energy levels of the fermion electron and obey the Pauli exclusion principle. The same principle applies for single excitons. In quantum dots, the number of excitable excitons is limited to one as in (1.5), yielding a very good approximation to single atoms. However, a more realistic description of quantum dots has to include further environmental influences, which will be discussed in Chap. 2, compare also [28, 29]. It is well established, that single atoms as single-photon emitters provide nonclassical features such as photon-antibunching and sub-Poisson photon statistics. The potential for squeezed-light emission from quantum-dot excitons will be considered in Chap. 2.

1.2. Multi-exciton systems

So far we considered the energy-level structure of a single exciton, which resembles an atom. Now let us turn to multiple excitons. In the high-density limit, as for atoms,

1. Excitons

excitons are subject to the Mott-effect, reducing the electron-hole binding energy to zero and yielding an electron-hole plasma [36, 37]. In this system, the correlations become weak, as the kinetic energy of its constituents is dominant. Hence, it is of less interest for our discussions and we focus on the low-density regime. For very low densities the excitonic operators acquire a bosonic commutation relation, $[\hat{B}_\lambda, \hat{B}_\lambda^\dagger] \approx \hat{1}$. The first order correction for higher densities can be described by a Kerr-nonlinear contribution in the Hamiltonian, while still attaining bosonic operator structure [33]. As in the single-exciton scenario discussed above, we may only take into account one excitation level, which is relevant for the interaction with fields, and omit the index $\lambda = \zeta$. Assume a system of identical excitons that can be in that excited state or the corresponding ground state. The eigenstate $|n\rangle$ of the Hamiltonian, with eigenenergy $E_n = \hbar\omega_n$, describes n excitons within the excited state. Hence, the multi-exciton kinetic Hamiltonian can be written as

$$\hat{H}_{\text{kin}} = \sum_{n=0}^{\infty} E_n |n\rangle\langle n| = \hbar \sum_{n=0}^{\infty} \omega_n |n\rangle\langle n| = \hbar\Lambda \hat{B}^\dagger \hat{B}. \quad (1.6)$$

Herein $\Lambda = \omega_1$ represents the single-exciton energy for that state. We already subtracted the ground-state energy, thus, $\omega_0 = 0$ in our system. Including the case of zero excitons will simplify the following calculations.

If the excitons would not interact, adding one exciton, i.e. $n \rightarrow n + 1$, just adds the same single-exciton energy $\hbar\omega_1 = \hbar\Lambda$ to the overall energy. The increase of the energy is linear in that case and Eq. (1.6) becomes

$$\hat{H}_{\text{kin}} = \hbar\omega_1 \sum_{n=1}^{\infty} n |n\rangle\langle n| \Rightarrow \hat{B}^\dagger \hat{B} = \sum_{n=0}^{\infty} n |n\rangle\langle n|. \quad (1.7)$$

This result is exactly the same as for ideal bosons, where $\hat{B}^\dagger \hat{B} = \hat{n}$ represents the number operator of the excitons. For interacting excitons, on the other hand, ω_n may have a nonlinear dependence on n . The influence of the interaction on the energy spacing is then encoded in \hat{B} and \hat{B}^\dagger , while $\hat{B}^\dagger \hat{B}$ is not directly related to the number of excitons $\langle \hat{n} \rangle$ anymore.

Let us introduce bosonic creation and annihilation operators for the states $|n\rangle$:

$$\hat{X} = \sum_{n=1}^{\infty} \sqrt{n} |n-1\rangle\langle n| \Rightarrow \hat{X}^\dagger \hat{X} = \sum_{n=0}^{\infty} n |n\rangle\langle n| = \hat{n} \Rightarrow [\hat{X}, \hat{X}^\dagger] = 1. \quad (1.8)$$

The orthogonality of the states $|n\rangle$, necessary for $[\hat{X}, \hat{X}^\dagger] = 1$, follows directly from the different number of constituent particles for the creation of n and m ($m \neq n$) excitons. As ω_n is a discrete function, with the arguments being the natural numbers, it can be expanded to a continuous, entire function $\omega(n)$ on \mathbb{R}^+ with the correct energy values for n being integer. This smooth function can be developed into a Taylor-series to yield for

the Hamiltonian

$$\hat{H}_{\text{kin}} = \hbar \sum_{n=0}^{\infty} \sum_{k=0}^{\infty} \frac{\omega^{(k)}(0)}{k!} n^k |n\rangle \langle n| = \hbar \sum_{k=0}^{\infty} \frac{\omega^{(k)}(0)}{k!} \underbrace{\sum_{n=0}^{\infty} n^k |n\rangle \langle n|}_{=(\hat{X}^\dagger \hat{X})^k} = \hbar \omega (\hat{X}^\dagger \hat{X}). \quad (1.9)$$

In this way we can rewrite the Hamiltonian (1.6) of the interacting system in terms of bosonic excitations. Note, that we do not require the excitons themselves to be bosonic, we just developed the Hamiltonian within this notation. Nevertheless, the identity $\langle \hat{X}^\dagger \hat{X} \rangle = n$ is conserved, giving us the average number n of excitons.

Now, we can expand \hat{B} from Eq. (1.6) in powers of the bosonic operators \hat{X} by applying (1.8) and

$$\hat{B}^\dagger \hat{B} = \sum_{n=1}^{\infty} \frac{\omega_n}{\Lambda} |n\rangle \langle n|, \quad \Rightarrow \quad \hat{B}^\dagger = \sum_{n=1}^{\infty} \sqrt{\frac{\omega_n}{\Lambda}} |n\rangle \langle n-1|, \quad (1.10)$$

$$\hat{X}^{\dagger k} \hat{X}^k = \sum_{n=k}^{\infty} \frac{n!}{(n-k)!} |n\rangle \langle n|, \quad \Rightarrow \quad \hat{X}^{\dagger k} \hat{X}^{k-1} = \sum_{n=k}^{\infty} \frac{(n-1)!}{(n-k)!} \sqrt{n} |n\rangle \langle n-1|, \quad (1.11)$$

$$\hat{B}^\dagger \hat{B} = \sum_{k=1}^{\infty} \alpha_k \hat{X}^{\dagger k} \hat{X}^k, \quad \& \quad \hat{B}^\dagger = \sum_{k=1}^{\infty} \beta_k \hat{X}^{\dagger k} \hat{X}^{k-1}. \quad (1.12)$$

In the first line, the global phase for \hat{B}^\dagger was chosen to be zero. Equation (1.12) yields recursive formulas for the prefactors α_k and β_k , which determine the expansion of the exciton operators \hat{B}^\dagger and $\hat{B}^\dagger \hat{B}$. For α_k we find

$$\frac{\omega_n}{\Lambda} = \sum_{k=1}^n \frac{n!}{(n-k)!} \alpha_k. \quad (1.13)$$

Using $\Lambda = \omega_1$, which is equivalent to the normalization $\hat{B}^\dagger |0\rangle = |1\rangle$, we find for the first three coefficients

$$\alpha_1 = 1, \quad \alpha_2 = \frac{\omega_2 - 2\omega_1}{2\omega_1}, \quad \alpha_3 = \frac{\omega_3 - 3\omega_2 + 3\omega_1}{6\omega_1}. \quad (1.14)$$

For the bosonic case, all higher order terms vanish for $\omega_n = n\omega_1$ and we have $\alpha_k = \delta_{k,1}$. The first order correction for the low-density kinetic Hamiltonian, thus, reads as

$$\hat{H}_{\text{kin}} = \hbar \omega_1 \hat{X}^\dagger \hat{X} + \hbar G \hat{X}^{\dagger 2} \hat{X}^2, \quad G = \omega_1 \alpha_2 = \frac{1}{2}(\omega_2 - 2\omega_1). \quad (1.15)$$

Thus we obtain the Kerr-nonlinearity proportional to G as stated in [33] as the first-order correction to the bosonic case. For Eq. (1.15) to be a valid approximation we must request $G \ll \omega_1$. The nonlinearity obtained in [V] is of the order of the exciton linewidth, i.e. lower than 1 meV. As the optical frequency ω_1 is of the order of 1 eV, the validity is given.

Kerr-nonlinearities are used in nonlinear crystals to create higher-order light fields, compare, e.g., [12]. Therefore, one application of such crystals is the generation of squeezed

1. Excitons

light. In Chap. 3, we will discuss, if the fluorescence of excitons in a quantum well, described by the above model, is squeezed. Another system, where Kerr-nonlinearity becomes relevant, are the optomechanical structures, where microscopic mechanical cantilevers are driven by a light field [42]. This model resembles very well a phonon interaction with a bosonic particle, as it also occurs in semiconductor micro- and nanostructures.

A final note should be given on the correction of the pump Hamiltonian, Eq. 1.3. Applying the same recurrence formalism, as to the coefficients α_k we find $\beta_1 = 1$ and

$$\beta_2 = \sqrt{\frac{\omega_2}{\omega_1}} - \sqrt{2} = \sqrt{2 + 2\alpha_2} - \sqrt{2} \approx \frac{\alpha_2}{\sqrt{2}}, \quad (1.16)$$

where we used $\alpha_2 \ll 1$. The amplitude of the correction is of the same order as for the kinetic part. However, in the Hamiltonian this would yield a term

$$\hat{H}_{\text{pump}} = \hbar\Omega_{\text{R}}\hat{X}^\dagger + \hbar\Omega_{\text{R}}^*\hat{X} + \hbar\Omega_{\text{R}}\beta_2\hat{X}^{\dagger 2}\hat{X} + \hbar\Omega_{\text{R}}^*\beta_2\hat{X}^\dagger\hat{X}^2, \quad (1.17)$$

where β_2 is scaled with Ω_{R} , instead of ω_1 . As the Rabi frequency is in the same order of magnitude as the nonlinearity G , it follows $|\Omega_{\text{R}}|\beta_2 \approx G\alpha_2 \ll G$. The correction acts on an even smaller frequency scale than the coupling constants in the Hamiltonian. There are no relevant dynamics of the emitted fields on this frequency scale. The correction is thus not needed for a good approximation. The overall Hamiltonian of interacting excitons coupling to a cw-laser field can be written as

$$\hat{H}_{\text{exc}} = \hat{H}_{\text{kin}} + \hat{H}_{\text{pump}} = \hbar\omega_1\hat{X}^\dagger\hat{X} + \hbar G\hat{X}^{\dagger 2}\hat{X}^2 + \hbar\Omega_{\text{R}}\hat{X}^\dagger + \hbar\Omega_{\text{R}}^*\hat{X}. \quad (1.18)$$

2. Quantum dots in semiconductor microcavities

The rate of interaction between a single photon and a single atomic dipole, a two-level system (TLS), is, in general, too weak to be applied for experiments on light-matter interaction. Thus, either a large number of identical photons is brought into the region of the TLS as is done with a laser, or the same photon is put in a resonator (a cavity) to allow multiple interactions with the TLS as long as the photon is trapped. Nowadays, cavity setups are possible that create very large interaction strengths, changing the dynamics of the atomic emission of an excited dipole fundamentally. In cavity-QED, three regimes of atom-cavity coupling are usually distinguished. Weak coupling describes coupling strengths below the dissipation rates of the TLS and the cavity mode, where the atomic emission is only perturbed by the interaction, yielding the well-known Purcell-effect [43]. In strongly coupled atom-cavity systems, where the coupling strength is larger than the dissipation rates, the TLS and the cavity mode become a combined system described by dressed states (polaritons). This system has been intensively studied in cavity QED [44]. Ultrastrong coupling is given when the coupling strength becomes comparable to the transition frequency of the TLS or the cavity (for optical cavities in the optical frequency range). These systems require a fully different treatment, as neither the rotating wave approximation, nor the dipole approximation yield reasonable results [45, 46].

Cavity QED has become one of the main areas of quantum optical research over the last decades [47]. To encompass just a few of the results connected to nonclassical light and quantum correlations: for both weakly, and strongly coupled atom-cavity systems, it was predicted that the emission fields are squeezed and antibunched [48], that the atom shows stationary occupation inversion [49], or has a reduced resonance linewidth below its natural value [50], and that the cavity slows down or even freezes internal light fields on macroscopic time scales [51]. Methods have been developed to determine the dynamics of the intracavity field from measurements of the cavity output field [52, 53]. Applying quantum-nondemolition measurements allowed to determine the photon statistics of the intracavity field without destroying the state of that field [54, 55]. Based on the possibilities of manipulating the state of cavity field and atom, as well as their

2. Quantum dots in semiconductor microcavities

emitted fields, atom-cavity systems are seen as one of the most important resources for implementing algorithms in quantum-information sciences.

Historically, the first strong atom-radiation coupling regimes studied were microwave and rf cavities coupled to Rydberg atoms [56, 57]. At that time, the atoms still propagated through the cavity, allowing only a limited interaction time. The same method was later applied to optical cavities [8]. Nowadays, the atom can be kept inside the cavity for macroscopic times with the help of an ion-trap [58, 59]. This step, along with advances in precise fabrication for both cavities and traps, allowed to increase the interaction to macroscopic times [60]. Ultrastrong coupling is achieved in more complex systems such as Josephson junctions as TLS in a superconducting circuit cavity [61, 62, 63].

Semiconductor microcavities are based on Fabry-Perot interferometry [64]. Quantum dots, acting as artificial atoms [65, 66], are fixed inside one material, the active layer, of cavity thickness. An alternating structure of two semiconductor materials serves as the cavity mirrors, reducing the emitted light due to the interferences. The microcavity system used in the group of Prof. Stolz is a cylindrical micropillar, see [67] for details.

Semiconductor microcavities with quantum dots as atoms have two advantages over atomic cavities. On one hand, the dot is always fixed inside the active layer, thus, making the trapping inside an ion trap or similar measures obsolete. This is especially interesting, as long time interaction in an applied scenario would not only require the energy of processes to keep the atom fixed for at least the same time. Also, the atom would either have to be stored, when it is not needed, or produced out of a source for every single use, if it cannot be stored.

On the other hand, the main potential advantage of semiconductor microcavities is the versatility of their parameters. Atomic microcavities are fixed, due to the fixed system parameters of the atom being also given. This includes the resonance frequency, the natural linewidth, the atom-cavity coupling and the dipole moment (i.e. the coupling to incoming light fields). Of course, also a more precise description of the atomic energy eigenstates may play a role for optical processes. Quantum dots are not fixed in their internal parameters, but can be tailor-made for specific applications, making semiconductor microcavities very interesting for applications. Furthermore, they are influenced by the environment in the active layer. One of the most famous effects is best explained via the Huang-Rhys model [68], see Subsec. 2.1.2. The quantum dot couples to the lattice vibrations (phonons), which in turn are governed by the sample temperature. Increasing the temperature induces a resonance shift of the quantum-dot resonance. As the cavity mode is not directly coupled to the phonons, this effect allows tuning the quantum dot resonance through a cavity mode resonance.

While the environmental coupling may manipulate the quantum dot parameters, in

general it is detrimental to the coherent interplay between matter and light. Hence, the transition from weak to strong coupling in semiconductor microstructures has proven difficult and only been achieved in a few systems [22, 23, 24, 25]. Two questions arise from the quantum optical point of view. How can the quantum-dot-cavity system be modeled sufficiently accurate to describe the emitted light fields on a quantum level? What kind of nonclassical phenomena can we expect from such a system if strong dissipative effects persist? Applying an atomic model for the quantum dot and a bath description for the environment, these questions have been discussed in [II, III, IV]. In [II] the influence of a phonon bridging the energy gap between different cavity modes on the spontaneous emission of quantum dot and cavity is modeled with a vibrational excitation of the atom. In [III, IV] the fluorescence light of a driven quantum dot in the environment of a micro-cavity is analyzed with respect to the possibility of squeezing.

2.1. Raman-assisted Rabi resonances in quantum-dot-cavity systems

2.1.1. Spontaneous emission from an excited quantum dot

In order to analyze the dynamics of a quantum dot in a cavity, let us first consider the unpumped system of a TLS and a quantized harmonic oscillator describing the atom and the intra-cavity light field, respectively. The atomic ground and excited states may be defined as $|1\rangle$ and $|2\rangle$, respectively, with the corresponding energies $\hbar\omega_1$ and $\hbar\omega_2$. We can use the atomic operators $\hat{A}_{ij} = |i\rangle\langle j|$, $i, j = 1, 2$ for the dynamical description, implying $\hat{B}_\zeta = \hat{A}_{12}$, cf. Eq. (1.5). The cavity mode is described by bosonic creation and annihilation operators \hat{a}^\dagger and \hat{a} , respectively, and has the energy-level separation $\hbar\omega_c$. Using the atomic completeness relation $\hat{A}_{11} + \hat{A}_{22} = \hat{1}$, subtracting the constant energy terms, and applying the rotating wave approximation for the dipole coupling between atom and cavity-mode, we obtain the famous Jaynes-Cummings Hamiltonian [69]:

$$\hat{H} = \hbar\omega_{21}\hat{A}_{22} + \hbar\omega_c\hat{a}^\dagger\hat{a} + \hbar g(\hat{a}^\dagger\hat{A}_{12} + \hat{A}_{21}\hat{a}). \quad (2.1)$$

Here we used $\omega_{21} = \omega_{22} - \omega_{11}$ and g is the atom-cavity coupling. A global phase has been adjusted in the interaction part for g to be real. The dynamics of this Hamiltonian is well established [70, 29]. It can be diagonalized using dressed states

$$|\psi_n\rangle = \alpha_n|1, n\rangle + \beta_n|2, n-1\rangle, \quad (2.2)$$

where the product state $|i, n\rangle$ means the atom being in state i and the cavity mode having n excitations. In case of resonance between atom and cavity ($\omega_c = \omega_{21}$), the prefactors

2. Quantum dots in semiconductor microcavities

simplify to $\alpha_n = \pm\beta_n$ and the eigenenergies read as

$$E_n = \hbar\omega_c n \pm \hbar g\sqrt{n}. \quad (2.3)$$

The dressed-state energies of the system are different from the energies of the atom or the cavity, revealing the necessity to view the atom-cavity system as one quantum structure.

Both, the atom and the cavity mode are coupled to the electromagnetic vacuum, a source for dissipation. These dissipative processes will be described within the framework of the master equation [29] using Lindblad terms of the form

$$\mathcal{L}_{\hat{u}}[\hat{\rho}] = 2\hat{u}\hat{\rho}\hat{u}^\dagger - \hat{\rho}\hat{u}^\dagger\hat{u} - \hat{u}^\dagger\hat{u}\hat{\rho}. \quad (2.4)$$

Herein \hat{u} is an arbitrary system operator and $\hat{\rho}$ is the density operator. We will make extensive use of this notation throughout this and the following chapter. The coupling to a bath causes a flow of energy to and from the system. Hence, we experience dissipation as well as incoherent pumping, expressed in the master equation via terms proportional to $\mathcal{L}_{\hat{u}}[\hat{\rho}]$ and $\mathcal{L}_{\hat{u}^\dagger}[\hat{\rho}]$, respectively. The rates of these relaxations and pumpings are Γ_u and P_u , respectively, with $\Gamma_u = P_u$ being the saturation case. In general, we have $0 < P_u \leq \Gamma_u$. Yet, in most scenarios the incoherent pumping in vacuum is very small and can be neglected for the calculations. The situation changes drastically for a quantum dot in a semiconductor, where the rates are also connected to thermal excitations in the medium, such as the phonons. The quantum-dot exciton can couple strongly to the phonons yielding an increased incoherent pumping for increasing temperatures. In the Lindblad notation the relevant operators for energy dissipation are $\hat{u} = \hat{A}_{12}$ for the atom and $\hat{u} = \hat{a}$ for the cavity mode.

The dissipation of energy levels also causes the phase coherence of each subsystem (dot and cavity mode) to decay, a process called dephasing. In terms of the density matrix, energy relaxation induces a decay of all matrix elements, while dephasing affects solely the nondiagonal elements. An energy decay of the atom with rate Γ coincides a radiative dephasing of rate $\Gamma/2$. However, due to the phonon bath, there occurs nonradiative or pure dephasing. An additional dephasing rate Γ_D has to be introduced into the master equation with $\hat{u} = \hat{A}_{22}$ for that matter. Pure dephasing of the cavity mode is negligible. Other proposals for further environment-induced dissipative processes exist, such as [71], but will not be discussed here.

2.1.2. Phonon-assisted Rabi flipping

The action of phonons on a quantum dot can be described with the Huang-Rhys model [68, 72]. In this model the phonons are described by bosonic annihilation and creation operators \hat{f}_k and \hat{f}_k^\dagger , respectively, and have frequencies ν_k . They couple to the excited atomic

state $|2\rangle$ with strength λ_k , yielding the new Hamiltonian

$$\hat{H}_{\text{ph}} = \hbar\omega_{21}\hat{A}_{22} + \hbar\omega_c\hat{a}^\dagger\hat{a} + \hbar g(\hat{a}^\dagger\hat{A}_{12} + \hat{A}_{21}\hat{a}) + \hbar\sum_k\nu_k\hat{f}_k^\dagger\hat{f}_k + \hbar\hat{A}_{22}\sum_k\lambda_k(\hat{f}_k^\dagger + \hat{f}_k). \quad (2.5)$$

Using the Huang-Rhys unitary transformation $\hat{U} = \exp[\hat{A}_{22}\sum_k\eta_k(\hat{f}_k^\dagger - \hat{f}_k)]$, with $\eta_k = \frac{\lambda_k}{\nu_k}$, yields

$$\hat{H}'_{\text{ph}} = \hbar(\omega_{21} - \Delta)\hat{A}_{22} + \hbar\omega_c\hat{a}^\dagger\hat{a} + \hbar\sum_k\nu_k\hat{f}_k^\dagger\hat{f}_k + \hbar g(\hat{a}^\dagger\hat{Y}\hat{A}_{12} + \hat{Y}^\dagger\hat{A}_{21}\hat{a}). \quad (2.6)$$

Herein, $\Delta = \sum_k\lambda_k^2/\nu_k$ describes a phonon-induced shift of the dot-resonance frequency, which becomes stronger with increasing phonon-dot coupling. Hence, for increasing temperature of the sample surrounding the quantum dot, its transition frequency can be shifted, see e.g. [22]. Furthermore, phonon-assisted Rabi-flippings are described via $\hat{Y} = \exp[-\sum_k\eta_k(\hat{f}_k^\dagger - \hat{f}_k)]$. Depending on the value of η_k , multiple phonons can be excited or relaxed via the Rabi flipping process. For lower temperatures with $\eta_k \ll 1$, it is sufficient to develop the exponent in \hat{Y} up to first order [73]. The zeroth order gives the standard Jaynes-Cummings model, while the first order yields single-phonon-assisted Rabi transitions. In case of these transitions, the energy of an excited dot and an excited phonon add up, and vice-versa for the relaxation.

It has been shown [74, 75], that such a model also describes the vibronic coupling (Raman coupling) of an atom to different field modes as given for an ion in a trap. While the phonons allow transitions in a broad spectrum, most of the transitions are offresonant to any electronic transition or Rabi transition of the atom-cavity system. Hence, only the resonant modes are relevant for the discussion. For only a few modes also the kinetic energy $\hbar\sum_k\nu_k\hat{f}_k^\dagger\hat{f}_k$ is very small and can be omitted from the discussion. Based on this argument we discussed a TLS in a two mode cavity with the electronic transition resonant to one mode a and a vibronic transition quasi-resonant to the second mode b in [II]. In such a system the influence of the phonons in a semiconductor micro-cavity can be studied, concerning offresonant dot-cavity coupling. This knowledge is essential when the parameters of both, dot and cavity mode (resonance frequencies, linewidths, couplings) are determined.

2.1.3. Two-mode cavity

The vibronic system (without the cavity) to be studied is shown in Fig. 2.1. The two cavity modes a and b are described by bosonic ladder operators \hat{a} , \hat{b} and their adjoints, and have mode-transition frequencies ω_a and ω_b , respectively. The main electronic transition of the atom is resonant with the a -mode, $\omega_{21} = \omega_a$. The vibrational transition is given by operators \hat{v} and \hat{v}^\dagger and has transition frequency ω_ν . The vibronic transition is detuned

2. Quantum dots in semiconductor microcavities

from the b -mode by $\delta\omega$. Finally, the a -mode couples to the electronic transition with rate g_a and the b -mode to the vibronic transition with rate g_b , while all other transitions are considered far offresonant and negligible. As we are interested in a phonon-like situation, $g_b = \eta_k g_a \ll g_a$. The Hamiltonian of the undamped system then reads as

$$\hat{H} = \hbar\omega_{21}(\hat{A}_{22} + \hat{a}^\dagger\hat{a} + \hat{b}^\dagger\hat{v}^\dagger\hat{b}\hat{v}) - \hbar\delta\omega\hat{b}^\dagger\hat{v}^\dagger\hat{b}\hat{v} + \hbar\hat{A}_{21}(g_a\hat{a} + g_b\hat{b}\hat{v}) + \hbar\hat{A}_{12}(g_a\hat{a}^\dagger + g_b\hat{b}^\dagger\hat{v}^\dagger), \quad (2.7)$$

with $\delta\omega = \omega_{21} - \omega_b - \omega_\nu$.

The Fock space of this quantum system is described by four quantum numbers $|i, n_a, n_b, k\rangle$ where i is the atomic state, n_a and n_b give the photon numbers of the respective cavity mode and k the vibrational excitation. As the system is not pumped, and we limit ourselves to one electronic excitation, there are only three excited states occurring. First, $|E\rangle = |2, 0, 0, 0\rangle$, is the excited atom with all other modes in the vacuum state. Second, the Rabi-flipped state of the a -mode is given by $|G\rangle = |1, 1, 0, 0\rangle$. Finally the vibration-assisted excitation of the b -mode is described by $|F\rangle = |1, 0, 1, 1\rangle$.

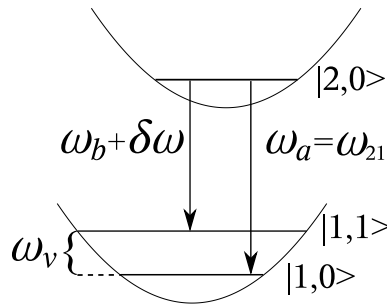


Figure 2.1.: Structure of the vibronic system. The Fock states $|j, k\rangle$ label the electronic and vibrational states, $j = 1, 2$ and $k = 0, 1$, respectively; after [II].

An initial state evolves unitarily under the Hamiltonian influence. Assuming the pure state $|E\rangle$ as initial state $|\psi(0)\rangle$, it remains pure, and we can write for times $t > 0$ as

$$|\psi(t)\rangle = e^{-i\omega_{21}t} [C_E(t)|E\rangle + C_G(t)|G\rangle + C_F(t)|F\rangle], \quad (2.8)$$

with $C_K(t)$ ($K = E, G, F$) being the amplitudes of the states as defined above. We separated the fast oscillation of the kinetic part of each state, so that the $C_K(t)$ only include the slowly varying amplitudes. The Schrödinger equation for $|\psi(t)\rangle$ yields a simple system of differential equations for the probability amplitudes:

$$i \begin{pmatrix} \dot{C}_E(t) \\ \dot{C}_G(t) \\ \dot{C}_F(t) \end{pmatrix} = \begin{pmatrix} 0 & g_a & g_b \\ g_a & 0 & 0 \\ g_b & 0 & -\delta\omega \end{pmatrix} \cdot \begin{pmatrix} C_E(t) \\ C_G(t) \\ C_F(t) \end{pmatrix}, \quad \text{with } C_K(0) = \delta_{K,E}. \quad (2.9)$$

Let us first consider the scenario of perfect Raman resonance ($\delta\omega = 0$), which is akin to a system of two degenerate cavity modes with different coupling strengths. In this case the Hamiltonian (2.7) reduces to

$$\hat{H} = \hbar\omega_{21}(\hat{A}_{22} + \hat{a}^\dagger\hat{a} + \hat{b}^\dagger\hat{v}^\dagger\hat{b}\hat{v}) + \hbar\hat{A}_{21} \left(g_a\hat{a} + g_b\hat{b}\hat{v} \right) + \hbar\hat{A}_{12} \left(g_a\hat{a}^\dagger + g_b\hat{b}^\dagger\hat{v}^\dagger \right) \quad (2.10)$$

and Eq. (2.9) can be easily solved to obtain

$$C_E(t) = \cos(\Omega_R t), \quad (2.11)$$

$$C_G(t) = -i \frac{g_a}{\Omega_R} \sin(\Omega_R t), \quad (2.12)$$

$$C_F(t) = -i \frac{g_b}{\Omega_R} \sin(\Omega_R t), \quad (2.13)$$

$$\Omega_R^2 = g_a^2 + g_b^2. \quad (2.14)$$

We find the same dynamics for the probability amplitudes of each cavity mode, scaled by the different couplings to the quantum dot. Though two cavity modes couple to the quantum dot, the system only experiences a single Rabi-oscillation with a combined Rabi-frequency Ω_R , as described in [76]. The occupation probabilities of the two cavity modes, P_a and P_b , respectively, are given by

$$\frac{P_b}{P_a} = \frac{|\langle F|\psi(t)\rangle|^2}{|\langle G|\psi(t)\rangle|^2} = \frac{|C_F(t)|^2}{|C_G(t)|^2} = \frac{g_b^2}{g_a^2}. \quad (2.15)$$

As $g_b \ll g_a$, Rabi-oscillation between the atomic excitation and the a -mode is almost unperturbed, while the Rabi-oscillation between the vibronic excitation and the b -mode is very weak. Depending on the limitations in an experimental setup, this oscillation might not be detectable even for a clearly visible a -mode Rabi-oscillation.

2.1.4. Dynamics of Raman-assisted Rabi resonances

The second scenario we consider, is the case of the Raman-assisted transition to the b -mode being detuned by the coupling strength of the a -mode to the electronic transition, i.e. $\delta\omega = g_a$. Contrary to the resonant case (2.10), for $\delta\omega \neq 0$, the excitation of state $|F\rangle$ starts to nutate. For large detuning $|\delta\omega| \gg g_a$, the fast oscillation would yield $C_F(t) \rightarrow 0$ within the rotating wave approximation. However, if the detuning matches the Rabi oscillation frequency of the a -mode to the atom, the nutation becomes resonant with the main Rabi-transition. Then, the Raman-assisted transition to the b -mode is fed by the Rabi-transition to the a -mode and increases with every Rabi-cycle, while draining energy out of the a -mode Rabi-cycle. This scenario is called Raman-assisted Rabi resonance (RARR).

There has been some mathematical discussion about a lossless two-mode cavity [77], yet an explicit physical system was not given. Furthermore, a physical interpretation of

2. Quantum dots in semiconductor microcavities

the simulated effects, as in the above discussion, was also absent. Based on the explicit solutions of the system (2.9) for $C_K(0) = \delta_{K,E}$, we could show in [II], that around RARR, $\delta\omega \approx g_a$, two oscillation cycles occur: the fast Rabi oscillation with $\Omega_R \approx g_a$, and the slow Raman-assisted transition with g_b .

The dynamics of the occupation probabilities $|C_K(t)|^2$ for both considered scenarios are depicted in Fig. 2.2. In case of perfect Raman-resonance ($\delta\omega = 0$), we obtain the equivalent behavior of both modes with the different scaling. For RARR ($\delta\omega = g_a$) on the other hand, we see the slow increase of the b -mode with every Rabi cycle of the a -mode transition, while both the a -mode excitation and the atomic excitation decrease at the same rate. This decrease is due to the limited energy in the system, $\sum_K |C_K(t)|^2 = 1$. Hence, the b -mode occupation probability $|C_F(t)|^2$ reaches a maximum, where half of the occupation is in the b -mode, while a -mode and atom each have one quarter of the excitation. After the primary Rabi oscillations with g_a nearly die out, the process is inverted, and the b -mode drives the Rabi cycle between $|E\rangle$ and $|G\rangle$.

It has to be stressed, how these two scenarios appear in the view of either the separated subsystems and the dressed-states picture. From the point of view of the separated subsystems, by tuning the weakly coupled b -mode away from the vibronic resonance, we increase the occupation probability for that cavity mode by a factor of 50. In the dressed states picture, on the other hand, we tune a single-mode resonant scheme (a) to a two-mode resonant scheme (b) and observe two Rabi oscillations, one between the electronic transition and the a -mode and one between the dressed state of atom and a -mode and the dressed state of vibronic system and b -mode.

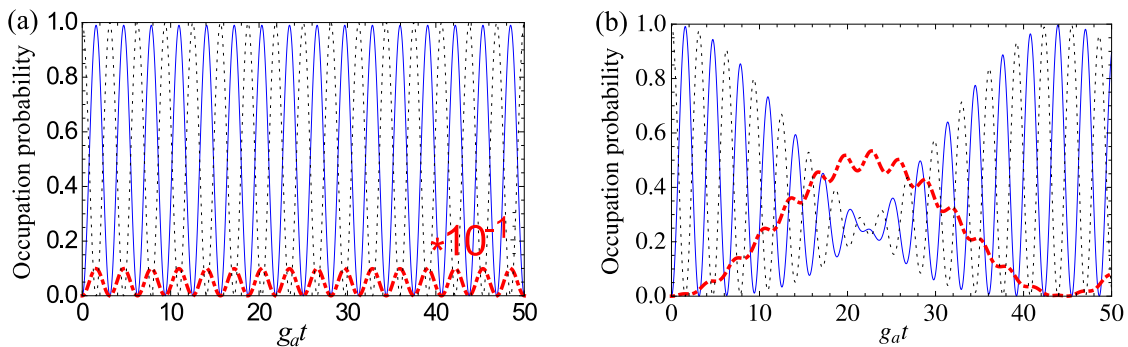


Figure 2.2.: Occupation probabilities of the states $|E\rangle$ (atom, black, dotted line), $|G\rangle$ (a -mode, blue, solid line), and $|F\rangle$ (b -mode plus vibration, thick, red, dashed-dotted line) over time for $g_a/g_b = 10$. (a) perfect Raman-resonance ($\delta\omega = 0$), where the b -mode is magnified by a factor of 10 to be clearly visible. (b) RARR ($\delta\omega = g_a$) without magnification; after [II].

The effect of driving one mode of light on the dressed state resonance of another is well known in laser physics for two-mode laser beams. One laser mode is resonant to an atomic

transition while the second is shifted to the Rabi side band of the first transition, leading to an enhanced atomic excitation [78, 79, 80, 81]. Within laser-physics, the phenomenon is called Rabi resonance. In cavity QED it is of limited recognition.

Let us compare the studied RARR scenario with the case of phonons in a semiconductor microcavity. In these structures a situation like RARR should be common. Phonons have a continuous spectrum, different intracavity modes are present due to the roughness of the cavity surface, and the quantum dots are tuned via the coupling to the phonon bath. Therefore, phonon-assisted Rabi resonances (PARR) can be expected for most quantum-dot scenarios. Due to RARR and PARR the dynamics of cavity modes and atom/quantum dot are highly sensitive to the different frequencies and couplings, and so should be the emitted light fields observed in experiments.

2.1.5. Spectral properties of the external field

In order to analyze the emitted light fields from the cavity mode or the atom, we have to include dissipation. As the phonons are directly included in the Hamiltonian, and we only have a single optical excitation, we limit these processes to the incoherent decay of atom and cavity mode. Furthermore, we are only interested in the decay of the different probability amplitudes $C_K(t)$ ($K = E, G, F$) from the single excitation state, and thus we do not need the full master-equation formalism. Instead we revert to the quantum trajectory approach, describing solely the decay of the state $|\psi(t)\rangle$ [50, 44]. For this purpose, we introduce the non-hermitian lossy Hamiltonian \hat{H}_L , which reads as

$$\hat{H}_L = \hat{H} - i\hbar\frac{\Gamma}{2}\hat{A}_{22} - i\hbar\frac{\kappa}{2}\hat{a}^\dagger\hat{a} - i\hbar\frac{\kappa}{2}\hat{b}^\dagger\hat{b}, \quad (2.16)$$

with \hat{H} being the lossless Hamiltonian in Eq. (2.7). Herein Γ is the spontaneous emission rate of the atom, while κ is the decay rate of both cavity modes. As κ is determined solely by geometrical factors for $|\omega_a - \omega_b| \ll \omega_a$ [29], we assume them to be equal. The vibrational quantum relaxation was neglected as it decays on a much longer timescale.

The equations of motion for the probability amplitudes $C_K(t)$ resemble those in Eq. (2.9) and read as

$$i \begin{pmatrix} \dot{C}_E(t) \\ \dot{C}_G(t) \\ \dot{C}_F(t) \end{pmatrix} = \begin{pmatrix} -i\frac{\Gamma}{2} & g_a & g_b \\ g_a & -i\frac{\kappa}{2} & 0 \\ g_b & 0 & -i\frac{\kappa}{2} - \delta\omega \end{pmatrix} \cdot \begin{pmatrix} C_E(t) \\ C_G(t) \\ C_F(t) \end{pmatrix}, \quad \text{with } C_K(0) = \delta_{K,E}. \quad (2.17)$$

Comparing with Eqs. (2.9) the dissipative terms on the main diagonal induce an exponential decay of all probabilities, as for $t \rightarrow \infty$ the probabilities for all excited states should tend to zero. For $\Gamma, \kappa < g_a, g_b$, as considered in [II], we are in the strong-coupling

2. Quantum dots in semiconductor microcavities

regime where the Rabi oscillations of both cycles prevail while the system excitation decays. Their Rabi frequencies are only slightly varied due to the damping rates. Hence, in the spontaneous-emission spectrum, we expect Rabi splitting on the cavity modes, which will help interpreting the effects of RARR.

The two cavity modes as well as the atom provide three different decay channels with emission probabilities P_K from the three excited states $|K\rangle = |E\rangle, |G\rangle, |F\rangle$. The emissions from the two cavity modes are spectrally separated by approximately the vibrational frequency ω_v , and can thus be independently detected in the cavity-output field. The atomic emission on the other hand is on the same frequency (or Rabi-split frequencies) as the a -mode. It may be detected out the side of the cavity and then subtracted from the output on the a -mode, or simply seen as a perturbation on the one cavity mode. We will focus on the intracavity fields in the following.

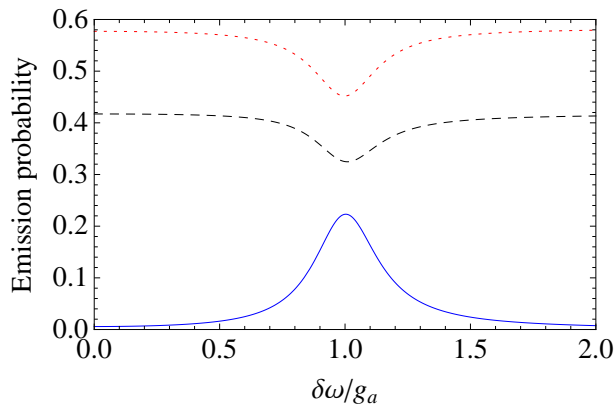


Figure 2.3.: Emission probabilities P_K for the photon from the a -mode (red, dotted curve), the b -mode (blue, solid curve) or the spontaneous emission from the atom (black, dashed curve) as a function of $\delta\omega$. The parameters are chosen as $\Gamma/g_a = 0.05$, $\kappa/g_a = 0.07$, and $g_b/g_a = 0.1$; after [II].

With the solution of Eq. (2.17) and applying the quantum-trajectory method [52], the probability $p_K(t)$ of emitting the photon between time 0 and t through the channel K is given by

$$p_K(t) = \gamma_K \int_0^t dt' |C_K(t')|^2, \quad \text{with } \gamma_E = \Gamma, \gamma_G = \gamma_F = \kappa. \quad (2.18)$$

The overall emission probability of each decay channel is then given in the limit for infinite time t : $P_K = \lim_{t \rightarrow \infty} p_K(t)$. We plot the three emission probabilities as functions of $\delta\omega/g_a$ for strong coupling parameters in Fig. 2.3. At the left end $\delta\omega = 0$ is the perfect Raman resonant scenario while the right end $\delta\omega = 2g_a$ depicts the far detuned vibration assisted b -mode coupling. In both cases, the emission from the b -mode is negligibly small. For all detunings, P_E and P_G remain above P_F . However, around RARR, the probability of emission from the b -mode has a maximum of around 25%. In an experiment, where

repeatedly a single-photon excitation of the atom is studied, every fourth photon would be emitted at a significantly different frequency than the dressed state frequencies of a -mode and atom. The influence of the phonons thus creates strong excitation on spectrally different modes, that have to be taken into account due to the dressed state resonances of the overall system.

Let us turn to the time-integrated spontaneous emission spectrum of the cavity [50]. It is given by the modulus of the positive frequency Fourier-transform of the probability amplitude of the two-mode cavity field, that is

$$S_{\text{cav}}(\omega) = \frac{\kappa}{2\pi} \left| \int_0^{\infty} dt e^{-i\omega t} [C_G^*(t)e^{i\omega_a t} + C_F^*(t)e^{i\omega_b t}] \right|^2, \quad (2.19)$$

The fast oscillations on each term reproduce the resonance frequencies of each cavity mode as resonance. Note that, contrary to the coefficients introduced in Eq. (2.8), the fast oscillation frequencies are different, as the vibration excitation does not decay in our scheme. Due to the modulus square, there appears an interference term in the overall spectrum. For spectrally separated modes $|\omega_a - \omega_b| \gg g_a, g_b, \kappa$, this term is negligible, as each cavity mode has only weak excitation on the resonance frequency of the other mode. Hence, we can approximate the spectrum as the sum of each cavity-mode spectrum as

$$\begin{aligned} S_{\text{cav}}(\omega) &\approx \frac{\kappa}{2\pi} [S_a(\omega) + S_b(\omega)] \\ &= \frac{\kappa}{2\pi} \left(\left| \int_0^{\infty} dt e^{-i(\omega-\omega_a)t} C_G^*(t) \right|^2 + \left| \int_0^{\infty} dt e^{-i(\omega-\omega_b)t} C_F^*(t) \right|^2 \right), \end{aligned} \quad (2.20)$$

where $S_a(\omega)$ and $S_b(\omega)$ are the respective single-mode spectra of the cavity modes. The spectrum of the atomic emission is given by

$$S_{\text{atom}}(\omega) = \frac{\Gamma}{2\pi} \left| \int_0^{\infty} dt e^{-i(\omega-\omega_{21})t} C_E^*(t) \right|^2. \quad (2.21)$$

Due to the structural similarity between $C_E(t)$ and $C_G(t)$, the atomic spectrum mainly resembles the a -mode spectrum and will not be depicted here.

The spectra for both Raman-resonant scheme and RARR are depicted in Fig. 2.4. As expected from the same behavior of the cavity modes in the first scenario, compare Eqs. (2.12,2.13), both modes show the identical Rabi-splitting with $2\Omega_R$. In the RARR scenario, on the other hand, the two Rabi-cycles between the different states become apparent, as each mode is split into a triplet due to $g_b > \kappa$. We only have one vibrational quantum; thus only one sideband is split. More importantly, the b -mode spectral amplitude on that side band is actually higher than the a -mode spectral amplitude. Thus, the

2. Quantum dots in semiconductor microcavities

emission of the b -mode becomes essential to the observed spectrum. In an experiment the impression may be, that while tuning an atom or a quantum dot through the resonance of one cavity mode, another mode may be enhanced strongly, or even show Rabi-splitting, though there is no atom or quantum dot in the spectral vicinity of the latter mode. Taking into account limitations of an applied detector due to white noise, the second mode may arise 'out of nowhere', indicating, falsely, a strongly coupling emitter nearby.

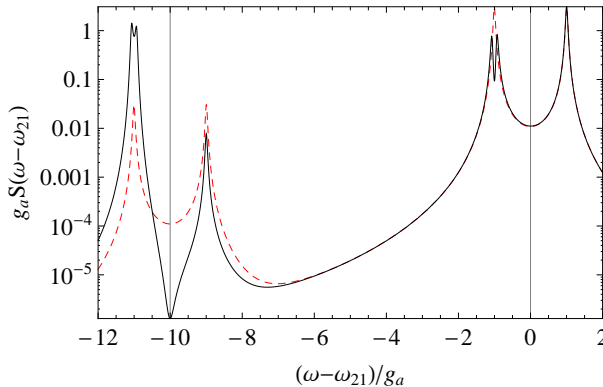


Figure 2.4.: Spontaneous emission spectrum of the intra-cavity fields of the two-mode cavity. For the sake of visibility $\omega_a - \omega_b$ was chosen to be $10g_a$. Shown are the perfect Raman resonance ($\delta\omega = 0$, red, dashed curve) and RARR ($\delta\omega = g_a$, black, solid curve) for the same parameters as in Fig. 2.3. The two vertical lines indicate the bare cavity frequencies ω_a and ω_b ; after [II].

We used strong coupling to clearly show the effects of RARR. Even for $\kappa > g_b$, at least the Purcell-effect [43] would be visible and increase the emission of the cavity mode. In the, not explicitly studied, case of PARR in a semiconductor microcavity, these effects are to be expected. Hence, it is necessary to make a very detailed analysis of the multimode-multi-quantum-dot cavity structure at hand in order to obtain the correct system parameters. These parameters are essential to study nonclassical effects of the emitted fields. At the end of this analysis it should be possible to consider a single-mode, single quantum-dot cavity system with established parameters. In the following we consider such a system given, where we studied the resonance fluorescence of the quantum dot and its capacity to emit squeezed light [III, IV].

2.2. Squeezing of quantum-dot fluorescence

2.2.1. Fluorescence of quantum dots in cavities

In the quantum-optical scenarios under study, the coupling between the light and matter is usually described within the dipole approximation. Within this regime, a photon may

be annihilated to excite one quantum of the source, e.g. the quantum dot being excited, or vice versa [28]. Already in the Jaynes-Cummings Hamiltonian, Eq. (2.1), this became evident with one excitation of the cavity field mode exchanging with the excitation of a single TLS. We considered the pump or laser Hamiltonian for a single exciton in Chap. 1, see Eq. (1.3). However, in a semiconductor micropillar, the incoming laser field hits an active medium, which is between the cavity mirrors. In this case due to interaction with the medium, scattering, or absorption and reemission, both a cavity mode a and the dot will in general be pumped. Going into the frame of the cw-laser frequency yields two pumping terms with two Rabi-frequencies:

$$\hat{H} = \hbar[\delta_x \hat{A}_{22} + \delta_c \hat{a}^\dagger \hat{a} + g \hat{a}^\dagger \hat{A}_{12} + g^* \hat{a} \hat{A}_{21}] + \hat{H}_{L,\text{mode}} + \hat{H}_{L,\text{dot}} \quad (2.22)$$

$$\hat{H}_{L,\text{mode}} = \hbar \Omega_{R,\text{mode}} \hat{a} + \hbar \Omega_{R,\text{mode}}^* \hat{a}^\dagger, \quad (2.23)$$

$$\hat{H}_{L,\text{dot}} = \hbar \Omega_{R,\text{dot}} \hat{A}_{12} + \hbar \Omega_{R,\text{dot}}^* \hat{A}_{21}. \quad (2.24)$$

Here the kinetic terms δ_j , $j = x, c$ are the resonance frequencies of dot and cavity mode, respectively, with respect to the laser frequency ω_L . It was shown [49], that the pumping of either the cavity mode or the dot can be transformed away, yielding a combined Rabi-frequency for the other subsystem. Applying the displacement-operator $\hat{D}(\alpha) = \exp[\alpha \hat{a}^\dagger - \alpha^* \hat{a}]$ ($\alpha \in \mathbb{C}$), we find

$$\hat{a}' = \hat{D}(\alpha) \hat{a} \hat{D}^\dagger(\alpha) = \hat{a} - \alpha, \quad (2.25)$$

$$\begin{aligned} \hat{H}'/\hbar = & \delta_x \hat{A}_{22} + \delta_c \hat{a}'^\dagger \hat{a}' + g \hat{a}'^\dagger \hat{A}_{12} + g^* \hat{a}' \hat{A}_{21} + \delta_c |\alpha|^2 - \Omega_{R,\text{mode}} \alpha^* - \Omega_{R,\text{mode}}^* \alpha \\ & + \left[(\Omega_{R,\text{dot}} - \alpha g^*) \hat{A}_{21} + (\Omega_{R,\text{mode}} - \alpha \delta_c) \hat{a}'^\dagger + \text{h.c.} \right] \end{aligned} \quad (2.26)$$

$$\mathcal{L}_{\hat{a}'}[\hat{\rho}] = \mathcal{L}_{\hat{a}}[\hat{\rho}] + [\alpha \hat{a}^\dagger, \hat{\rho}] + [\alpha^* \hat{a}, \hat{\rho}]. \quad (2.27)$$

The Lindblad-term of the emission of the quantum dot is obviously not affected. The absolute energy terms only shift the overall system and are not relevant in the master equation and can be omitted. For $g = 0$, the cavity field would tend to a coherent state with amplitude $\beta = \frac{-i\Omega_{R,\text{mode}}}{i\delta_c + \frac{\kappa}{2}}$ for $t \rightarrow \infty$. By setting $\alpha = \beta$, the pumping of the cavity mode becomes zero, and we obtain

$$\hat{H}'/\hbar = \delta_x \hat{A}_{22} + \delta_c \hat{a}'^\dagger \hat{a}' + g \hat{a}'^\dagger \hat{A}_{12} + g^* \hat{a}' \hat{A}_{21} + \tilde{\Omega}_{R,\text{dot}} \hat{A}_{21} + \tilde{\Omega}_{R,\text{dot}}^* \hat{A}_{12} \quad (2.28)$$

$$\frac{d\hat{\rho}}{dt} = \frac{1}{i\hbar} [\hat{H}', \hat{\rho}] + \frac{\Gamma}{2} \mathcal{L}_{\hat{A}_{12}}[\hat{\rho}] + \frac{\kappa}{2} \mathcal{L}_{\hat{a}}[\hat{\rho}], \quad (2.29)$$

with $\tilde{\Omega}_{R,\text{dot}} = \Omega_{R,\text{dot}} - \beta g^* = \Omega_{R,\text{dot}} + \frac{ig^*}{i\delta_c + \frac{\kappa}{2}} \Omega_{R,\text{mode}}$. Thus, we can restrict our discussion to the sole case of the emitter being pumped with an effective Rabi frequency $\Omega_R = \tilde{\Omega}_{R,\text{dot}}$. Finally choosing the absolute phases so that the coupling parameters Ω_R and g are real,

2. Quantum dots in semiconductor microcavities

we have the basic Hamiltonian for our study:

$$\hat{H}'/\hbar = \delta_x \hat{A}_{22} + \delta_c \hat{a}^\dagger \hat{a} + g(\hat{a}^\dagger \hat{A}_{12} + \hat{a} \hat{A}_{21}) + \Omega_R(\hat{A}_{21} + \hat{A}_{12}) \quad (2.30)$$

$$\frac{d\hat{\rho}}{dt} = \frac{1}{i\hbar} [\hat{H}', \hat{\rho}] + \frac{\Gamma}{2} \mathcal{L}_{\hat{A}_{12}}[\hat{\rho}] + \frac{\kappa}{2} \mathcal{L}_{\hat{a}}[\hat{\rho}]. \quad (2.31)$$

2.2.2. Nonclassical light from single-photon emitters

A quantum dot, modeled as a TLS with coherent pumping, cavity- and dissipative coupling to the environment, is a single photon emitter (SPE). SPEs are well established sources for nonclassical light. Two main features, that have been predicted and observed for different classes of SPEs are antibunching and sub-Poisson photon statistics. If a TLS emits a photon, it must first be re-excited, before it can emit another photon. Hence, the probability of emitting two photons simultaneously, is zero; the emitted photons are antibunched. In a more general sense, antibunching means, that the probability of one photon excitation after time t and another after time $t + \tau$ increases with τ . This corresponds to a positive slope of the second-order steady-state intensity-correlation function

$$g^{(2)}(\tau) = \lim_{t \rightarrow \infty} \frac{\langle \hat{E}^{(-)}(t) \hat{E}^{(-)}(t + \tau) \hat{E}^{(+)}(t + \tau) \hat{E}^{(+)}(t) \rangle}{\langle \hat{E}^{(-)}(t) \hat{E}^{(+)}(t) \rangle^2}. \quad (2.32)$$

Antibunching of photons was first predicted for a laser-driven two-level atom in [3, 4], and first observed with a low-density atomic beam by Kimble *et al.* [5].

For any physical system where correlations decay over time, $\lim_{\tau \rightarrow \infty} g^{(2)}(\tau) = 1$. Hence, antibunching is given, if for any finite τ we find $g^{(2)}(\tau) < 1$. A special case connected to the observation of antibunched light is the phenomenon of sub-Poisson photon statistics, $g^{(2)}(0) < 1$. At $\tau = 0$, we consider the variance of the photon statistics. If the variance of the photon-number distribution becomes smaller than for case of coherent light (Poisson) the light field is nonclassical. The special structure of a SPE as described above yields $g^{(2)}(0) = 0$. Sub-Poisson photon statistics was first shown in experiments with an atomic beam in [82]. Later, both antibunching and sub-Poisson photon statistics could be detected, first with trapped ions [13, 14] and then with quantum dots in different micro-systems, such as optical cavities [18, 19, 20, 21]. These latter experiments motivate the notion of quantum dots as SPEs.

Another nonclassical effect, which has attracted a lot of attention over the years, is squeezed light. A light field is called squeezed, if its variance falls below the shot noise level, i.e. the variance of the field in the vacuum state. Equivalently, squeezing of a light field is given, if the normally-ordered variance of the field $\langle : (\Delta \hat{E})^2 : \rangle$ becomes negative. Nowadays strong squeezing sources are based on nonlinear crystals acting on input-light fields [12]. However, squeezed light was also predicted to occur in the resonance

fluorescence of driven SPEs [17]. The squeezing can be enhanced for many atoms, by regularly aligning the atoms [83]; by detecting the fluorescence in the forward direction with respect to the driving laser beam [84]; or by utilizing the bistability of the system in a strong driving field [85]. Squeezing was found in experiments for the latter two cases [15, 16]. However, a direct observation of SPE- fluorescence squeezing is still missing.

The obstacle in observing SPE-fluorescence squeezing is the very small collection efficiency, which is too tiny in the usually applied balanced homodyne detection method, see [29] for details. To overcome this limitation, homodyne correlation measurement techniques were proposed in theory [86, 87, 88], where the collection efficiency becomes merely an overall factor in front of a desired correlation. These techniques were first demonstrated in the resonance fluorescence of a single trapped ion [89]. We will reconsider them for our system at the end of this chapter.

In a more recent experiment, the output field of a driven cavity, containing an atom, was shown to be weakly squeezed [90]. The advantage of analyzing the cavity field, instead of the atomic fluorescence itself, is the focused beam of light from the cavity mode, that can be easily collected by a detector. It was argued, that the cavity mode itself can not emit squeezed light, so the squeezing would be a direct consequence of the nonlinear atom-cavity coupling. However, in general, it is not possible to conclude in the other direction that the squeezing of the cavity field implies squeezing of the fluorescence.

2.2.3. Squeezing of single-photon-emitter fluorescence

While the observation of [90] only indicates a possible fluorescence squeezing, the experiments imply the possibility of optimizing the chances of observation of squeezing when applying the SPE to a cavity mode. In [III, IV], we showed, that a cavity mode of intermediate coupling parameters may serve as a passive environment. It optimizes the squeezing of the fluorescence, in terms of intensity-to-noise ratio as well as stability against dissipative environments.

Throughout the following analysis we suppress the arguments \vec{r} and t of the fields, unless they become necessary. Squeezing of a light field is given for a negative normally ordered variance of the field. Splitting the fields into positive and negative frequency parts $\hat{E}^{(+)}$, $\hat{E}^{(-)}$, respectively, we can write this variance as

$$\begin{aligned} \langle : (\Delta \hat{E})^2 : \rangle &= \langle : (\Delta [\hat{E}^{(-)} + \hat{E}^{(+)}])^2 : \rangle \\ &= 2 \langle (\Delta \hat{E}^{(-)}) (\Delta \hat{E}^{(+)} \rangle + \langle (\Delta \hat{E}^{(+)})^2 \rangle + \langle (\Delta \hat{E}^{(-)})^2 \rangle. \end{aligned} \quad (2.33)$$

Herein we used the notation $\Delta \hat{X} = \hat{X} - \langle \hat{X} \rangle$ as well as the normal ordering procedure $: \dots :$ which orders the operators $\hat{E}^{(-)}$ to the left of operators $\hat{E}^{(+)}$. In normal ordering, the source fields \hat{E}_s and the free fields \hat{E}_f can be separated and also the free fields become

2. Quantum dots in semiconductor microcavities

normally ordered. If the free fields are in the vacuum state, i.e., if only the signal field hits the detector, then the free fields do not contribute to normally-ordered correlation function. Hence, the discussion of squeezing is limited to the source fields

$$\langle : (\Delta \hat{E})^2 : \rangle = \langle : (\Delta \hat{E}_s)^2 : \rangle. \quad (2.34)$$

Consequently, we can omit the index 's' in the following description, as we only consider source fields.

Now let us turn to the case of a SPE, described by a TLS in an arbitrary environment [17, 29]. The source field operators are proportional to the flip operators of the TLS,

$$\hat{E}^{(-)} = \chi \hat{A}_{21}, \quad \hat{E}^{(+)} = (\hat{E}^{(-)})^\dagger = \chi^* \hat{A}_{12}, \quad (2.35)$$

where χ describes the dipole coupling between the flip-operators and the source fields, projected onto the direction of detection. It is impossible to simultaneously excite a SPE twice, so we have

$$\hat{E}^{(-)2} \propto \hat{A}_{21}^2 = 0, \quad (2.36)$$

which is exactly the core of the sub-Poisson and antibunched nature of SPEs. The normally-ordered field variance simplifies to

$$\begin{aligned} \langle : (\Delta \hat{E})^2 : \rangle &= 2|\chi|^2 (\langle \hat{A}_{22} \rangle - |\langle \hat{A}_{12} \rangle|^2) - 2\Re(\chi^* \langle \hat{A}_{12} \rangle^2) \\ &= 2|\chi|^2 \left(\langle \hat{A}_{22} \rangle - |\langle \hat{A}_{12} \rangle|^2 - |\langle \hat{A}_{12} \rangle|^2 \cos[\varphi(t)] \right), \end{aligned} \quad (2.37)$$

where $\varphi(t)$ contains the complex phases of $\langle \hat{A}_{12} \rangle$, χ^* , as well as the fast oscillation of the dipole with ω_x . For given system parameters, $\langle \hat{A}_{22} \rangle$ and $\langle \hat{A}_{12} \rangle$ are fixed, so that only the cosine term changes the variance. The minimal and maximal variance are obviously given for $\cos[\varphi(t)] = \pm 1$, respectively, and for minimal variance (maximal squeezing) we obtain

$$\langle : (\Delta \hat{E})^2 : \rangle_{\min} = 2|\chi|^2 (\langle \hat{A}_{22} \rangle - 2|\langle \hat{A}_{12} \rangle|^2). \quad (2.38)$$

The amplitude of squeezing (negative amplitude of minimal variance) for SPE fluorescence is connected to the excitation $\langle \hat{A}_{22} \rangle$ of the SPE and the coherence $|\langle \hat{A}_{12} \rangle|^2$ of that excitation.

What is the maximum coherence $|\langle \hat{A}_{12} \rangle|^2$ for a given excitation $\langle \hat{A}_{22} \rangle$? It can be seen using the density matrix σ for the state, which is connected to the density operator of the SPE $\hat{\sigma}$ via $\hat{\sigma} = \sum_{i,j=1}^2 \sigma_{i,j} \hat{A}_{ij}$ and has components $\sigma_{i,j} = \langle \hat{A}_{ji} \rangle$. As the density matrix describes a physical quantum state, we require that $\text{Tr}[\hat{\sigma}^2] \leq 1$, which gives

$$\langle \hat{A}_{11} \rangle^2 + \langle \hat{A}_{22} \rangle^2 + 2|\langle \hat{A}_{12} \rangle|^2 \leq 1. \quad (2.39)$$

Applying the completeness relation $\langle \hat{A}_{11} \rangle + \langle \hat{A}_{22} \rangle = 1$, we find

$$|\langle \hat{A}_{12} \rangle|^2 \leq \langle \hat{A}_{22} \rangle - \langle \hat{A}_{22} \rangle^2 = \langle \hat{A}_{11} \rangle \langle \hat{A}_{22} \rangle. \quad (2.40)$$

The result in Eq. (2.38) yields for the optimal minimal variance for a given SPE excitation

$$\frac{\langle : (\Delta \hat{E})^2 : \rangle_{\text{opt,min}}}{|\chi|^2} = 2\langle \hat{A}_{22} \rangle(2\langle \hat{A}_{22} \rangle - 1), \quad (2.41)$$

and the absolute minimal variance can be obtained for $\langle \hat{A}_{22} \rangle = 1/4$,

$$\frac{\langle : (\Delta \hat{E})^2 : \rangle_{\text{abs}}}{|\chi|^2} = -\frac{1}{4}. \quad (2.42)$$

The condition applied for maximal coherence, $\text{Tr}[\hat{\sigma}^2] = 1$, is equivalent to a pure state of the SPE. Hence, optimal squeezing of SPE fluorescence is only obtained if the subsystem of the SPE is in a pure quantum state. Let us compare this result with the squeezing available in free-space SPE fluorescence. Consider the system Eqs. (2.30) and (2.31) with $g = \kappa = 0$, which reads as

$$\hat{H}_{\text{fs}} = \hbar\delta_x \hat{A}_{22} + \hbar\Omega_R(\hat{A}_{12} + \hat{A}_{21}), \quad (2.43)$$

$$\dot{\hat{\sigma}}_{\text{fs}} = \frac{1}{i\hbar}[\hat{H}_{\text{fs}}, \hat{\sigma}_{\text{fs}}] + \frac{\Gamma}{2}\mathcal{L}_{\hat{A}_{12}}[\hat{\sigma}_{\text{fs}}]. \quad (2.44)$$

The index 'fs' labels free-space fluorescence. We are interested in the steady-state solution of this system, which can be given via one complex variable α and its modulus $z = |\alpha|^2$:

$$\alpha = \frac{-i\Omega_R}{\frac{\Gamma}{2} + i\delta_x}, \quad \langle \hat{A}_{22} \rangle = \frac{z}{1+2z}, \quad \langle \hat{A}_{12} \rangle = \frac{\alpha}{1+2z}, \quad |\langle \hat{A}_{12} \rangle|^2 = \frac{z}{(1+2z)^2}. \quad (2.45)$$

Comparing with the left hand side of Eq. (2.39), we find

$$\text{Tr}[\hat{\sigma}_{\text{fs}}^2] = 1 - 2\langle \hat{A}_{22} \rangle^2. \quad (2.46)$$

For increasing excitation, the purity of the atomic quantum state in a free-space-fluorescence scenario decreases. Hence, optimal squeezed emission can not be obtained in this case. To the contrary, for strong driving ($\Omega_R \rightarrow \infty$, $z \rightarrow \infty$), the state has no coherence at all ($\langle \hat{A}_{12} \rangle \rightarrow 0$). Consequently, squeezing is predicted to be only observable for low excitation [17, 29]. The phase-optimized free-space normally-ordered variance reads as

$$\frac{\langle : (\Delta \hat{E})^2 : \rangle_{\text{fs}}}{|\chi|^2} = 2\langle \hat{A}_{22} \rangle(4\langle \hat{A}_{22} \rangle - 1). \quad (2.47)$$

Squeezed light emission is limited to $\langle \hat{A}_{22} \rangle \leq 1/4$, which is actually the value of maximal squeezing in the optimal scenario. The maximal squeezing in free space follows as

$$\langle \hat{A}_{22} \rangle = \frac{1}{8}, \quad \frac{\langle : (\Delta \hat{E})^2 : \rangle_{\text{fs,min}}}{|\chi|^2} = -\frac{1}{8}. \quad (2.48)$$

2. Quantum dots in semiconductor microcavities

It can be stated, that squeezing of the SPE fluorescence in free space is possible, but limited due to the impurity induced on the quantum state. This impurity is based on the dissipative coupling to the vacuum modes, described by the Lindblad term $\mathcal{L}_{\hat{A}_{12}}$. As the excitation increases, so does the dissipative, or incoherent emission. However, in free space there is no other decay channel or coupling to control the dynamics of the SPE via external parameters. Optimal squeezing requires a purification of the SPE quantum state for non-vanishing excitation. It should be pointed out, that pure states of SPEs have become a major subject of interest more recently in quantum information theory. For that reason, protocols for purification [91, 92], and its determination [93, 94, 95] have been developed. However, these will be of less interest for us, as we consider fixed quantum dots in microcavities. Another possibility to purify a SPE quantum state is to couple it to an environment specifically tailored for purification. We have shown, that a cavity with intermediate coupling strength $g \approx \kappa$ can be sufficient for this purpose [III, IV]. In the following the principle of this purification scheme will be considered, as well as its robustness against further dissipative or incoherent channels.

2.2.4. Cavity induced purification

Let us first consider the driven SPE in a cavity scenario, described by Eqs. (2.30,2.31) and shown in Fig. 2.5. The resonance frequencies of SPE (ω_x), cavity mode (ω_c) and laser (ω_L) are all different and we are solely interested in the SPE fluorescence out the side of the cavity. In semiconductor microcavities, the emission of a quantum dot may also be observed through the cavity mirrors, but is then subject to the frequency dependent transmission coefficient of the cavity [96]. This system can not be solved analytically for all cases, but only approximately for different scenarios such as [50]. For numerical calculations we will compute the density matrix up to a sufficient cut-off number of cavity excitations.

The main idea behind the purification is, that the cavity provides a second incoherent decay channel, while the SPE-cavity coupling preserves the coherence of the SPE induced by the laser coupling. In this case most of the incoherent emission of the SPE-cavity system is channeled into the cavity, whereas the SPE remains more coherent than in free space. In general the setup should always provide a certain amount of purification. However, we are interested in a setup where mainly the SPE is excited, to compare with the free-space-fluorescence scenario. Hence, as in [III,IV], we choose a system of parameters, where the cavity does not directly affect the SPE dynamics. Let the SPE be in strongly pumped, offresonant setup: $\Gamma \ll \Omega_R, |\delta_x|$, and therefore $z \approx \Omega_R^2/\delta_x^2$. For a cavity-laser detuning $|\delta_c|$ large compared to the SPE-cavity coupling g , the cavity remains almost empty, $\langle \hat{a}^\dagger \hat{a} \rangle \ll 1$. In this case, we mainly observe fluorescence as in free space.

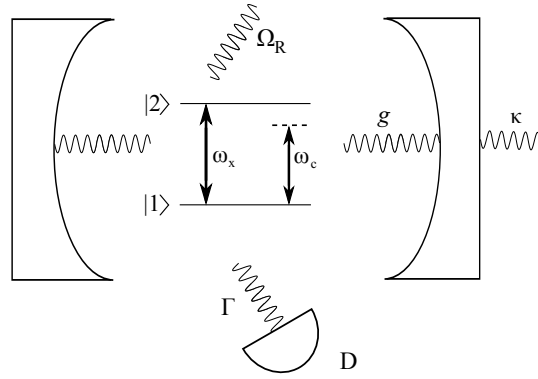


Figure 2.5.: Coherently pumped SPE inside a lossy cavity. The fluorescent light is detected (D) out the side of the cavity, in difference to the cavity emission through the cavity walls. All couplings between SPE, cavity mode, laser and the electromagnetic vacuum are pointed out by wavy lines. The arrows indicate the resonance frequencies of the SPE transition and the cavity mode; after [III].

Due to the strong SPE-laser coupling the SPE-emission has two sidebands [6, 7] besides the main emission on ω_x . As shown in [97, 98] the effective energy transport from the SPE to the cavity is enhanced, if the Mollow sideband is resonant to the cavity mode,

$$\delta_c^2 = (2\Omega_R)^2 + \delta_x^2. \quad (2.49)$$

This scenario is called cavity resonance. For the sake of clarity, we consider the lower energy sideband, which means that $\omega_c < \omega_x$.

Two effects come into play at a cavity resonance. On one hand, the cavity excitation rises because of the resonance, but only slightly due to the strong detuning δ_c . However, due to the strong cavity-emission rate $\kappa \gg \Gamma$, most of the energy is emitted from the cavity mode. Hence, the emission out of the cavity increases substantially. Consequently, the SPE excitation $\langle \hat{A}_{22} \rangle$ drops, as the pump energy is now split between SPE and cavity mode. This effect was recently also described in connection to steady-state inversion of a two-level-atom in a cavity [99]. It should be noted, that we do not need strong coupling between SPE and cavity. The main condition for purification is a strong cavity emission $\kappa \gg \Gamma$. On the other hand, the coherence of the SPE, $|\langle \hat{A}_{12} \rangle|^2$, increases. It serves as a measure for the radiative coupling of the energy levels of the SPE with each other. Increasing the energy transport between SPE and cavity also increases the rate of transitions between excited and ground state $|2\rangle$ and $|1\rangle$ and thus the coherence. Combining the decrease of $\langle \hat{A}_{22} \rangle$ and the simultaneous increase of $|\langle \hat{A}_{12} \rangle|^2$ with Eq. (2.39), it becomes clear, that tuning the SPE through a cavity resonance purifies the subsystem of the SPE.

2. Quantum dots in semiconductor microcavities

A consequence of the setup requirements is $g \gg \Gamma$, as the SPE-cavity coupling should be dominant in comparison with the spontaneous emission of the SPE. In experiments of atoms in microcavities, $g \approx 23\Gamma$ was found [100]; we will use $g = 23\Gamma$ in all calculations. Note, that the parameters in semiconductor microcavities may even be preferential in this respect [101]. Let us consider the other system parameters from the example in [III,IV]: $\Omega_R = 14g$, $\delta_c = -34g$, and $\kappa = 1.58g$. The steady-state expectation values and purity of the SPE as well as the squeezing of the fluorescence are shown in Fig. 2.6 as functions of δ_x . The cavity resonance occurs at approximately $\delta_x \approx -19.3g$, corresponding to $z \approx 0.54$.

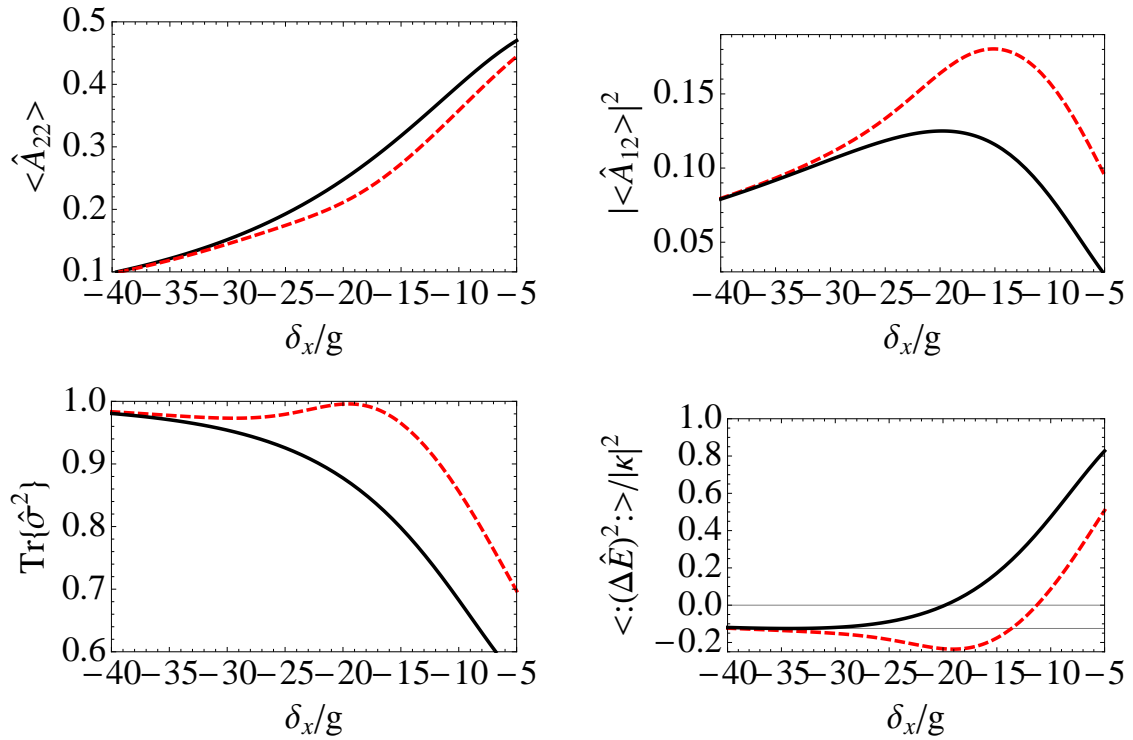


Figure 2.6.: Behavior of the SPE in free space (solid, black curve) and in the cavity (red, dashed curve) as a function of δ_x : excitation $\langle \hat{A}_{22} \rangle$ (left top), coherence $|\langle \hat{A}_{12} \rangle|^2$ (right top), purity $\text{Tr}[\hat{\sigma}^2]$ (left bottom) and the phase-optimized minimal-normally ordered field variance of the fluorescence (right bottom). In the last figure, the two straight lines indicate maximal free-space squeezing ($-1/8$) and vanishing squeezing 0. Note that the lower end of the ordinate for the last figure is equal to the absolute maximum of squeezing ($-1/4$); after [IV].

The decrease of $\langle \hat{A}_{22} \rangle$ and the increase of the coherence $|\langle \hat{A}_{12} \rangle|^2$ around the cavity resonance are clearly visible in the respective figures. The purity $\text{Tr}[\hat{\sigma}^2]$ of the SPE subsystem has a maximum value of about 99.5%. The minimal normally-ordered field variance around the cavity resonance is -0.236 , which is more than 94% of the maximum

possible squeezing of $-1/4$.

2.2.5. Approximate analytical description

Due to the very weak excitation of the cavity mode, it is possible to analyze the system Eqs. (2.30,2.31) analytically within some approximations. This will help to understand the underlying physics of the purification process. Furthermore, this approximation can also be applied when including other dissipative effects described above, and studying the stability of the squeezing against these effects.

Applying the master-equation formalism, we can derive the equations of motion for excitations and coherences of both the SPE and the cavity mode as follows

$$\partial_t \langle \hat{a} \rangle = -[i\delta_c + \frac{\kappa}{2}] \langle \hat{a} \rangle - ig \langle \hat{A}_{12} \rangle, \quad (2.50)$$

$$\partial_t \langle \hat{A}_{12} \rangle = -[i\delta_x + \frac{\Gamma}{2}] \langle \hat{A}_{12} \rangle - ig \langle \hat{a} \rangle + 2ig \langle \hat{A}_{22} \hat{a} \rangle, \quad (2.51)$$

$$\partial_t \langle \hat{a}^\dagger \hat{a} \rangle = -\kappa \langle \hat{a}^\dagger \hat{a} \rangle - ig \left[\langle \hat{a}^\dagger \hat{A}_{12} \rangle - \langle \hat{A}_{12} \hat{a} \rangle \right], \quad (2.52)$$

$$\partial_t \langle \hat{A}_{22} \rangle = -\Gamma \langle \hat{A}_{22} \rangle - ig \left[\langle \hat{A}_{12} \hat{a} \rangle - \langle \hat{a}^\dagger \hat{A}_{12} \rangle \right] - i\Omega_R \left[\langle \hat{A}_{21} \rangle - \langle \hat{A}_{12} \rangle \right]. \quad (2.53)$$

In the steady-state regime, we can substitute the term proportional to $\langle \hat{a} \rangle$ in Eq. (2.51) and the term proportional to g in Eq. (2.53) using the relations

$$\langle \hat{a} \rangle = \frac{-ig}{i\delta_c + \frac{\kappa}{2}} \langle \hat{A}_{12} \rangle, \quad (2.54)$$

$$\langle \hat{a}^\dagger \hat{a} \rangle = -\frac{ig}{\kappa} \left[\langle \hat{a}^\dagger \hat{A}_{12} \rangle - \langle \hat{A}_{12} \hat{a} \rangle \right]. \quad (2.55)$$

Equation (2.54) is the essence of the Purcell-effect [43, 44] for weak coupling, where the cavity field only scales the system parameters of the SPE. Comparing with our parameters in the example, we find

$$|\langle \hat{a} \rangle|^2 = \frac{g^2}{(\frac{\kappa}{2})^2 + \delta_c^2} |\langle \hat{A}_{12} \rangle|^2 \approx \frac{1}{1000} |\langle \hat{A}_{12} \rangle|^2. \quad (2.56)$$

The cavity-field coherence is three orders of magnitude smaller than the SPE coherence, implying the incoherent nature of the intracavity field as stated above. Equation (2.55) connects the excitation of the cavity field to the excitation of the SPE via the Rabi-flip operators $\hat{a}^\dagger \hat{A}_{12}$ and its adjoint that also appear in (2.53). Combining these equations with the equations of motion, we find new dynamical equations for SPE coherence and excitation, that read as

$$\left[i\delta_x + \frac{\Gamma}{2} + \frac{g^2}{i\delta_c + \frac{\kappa}{2}} \right] \langle \hat{A}_{12} \rangle = 2ig \langle \hat{A}_{22} \hat{a} \rangle - i\Omega_R (1 - 2\langle \hat{A}_{22} \rangle), \quad (2.57)$$

$$\langle \hat{A}_{22} \rangle = \frac{2\Omega_R}{\Gamma} \Im \langle \hat{A}_{21} \rangle - \frac{\kappa}{\Gamma} \langle \hat{a}^\dagger \hat{a} \rangle. \quad (2.58)$$

2. Quantum dots in semiconductor microcavities

We call the prefactor on the left hand side of Eq. (2.57) V . The free-space dynamics of $\langle \hat{A}_{12} \rangle$ are given by the second term on the right hand side, proportional to Ω_R . The first term on the right hand side, $\langle \hat{A}_{22} \hat{a} \rangle$, is a higher order term, requiring a state with both the SPE and the cavity mode being excited. In the limit of very weak cavity excitation, we can neglect this term to obtain

$$\langle \hat{A}_{12} \rangle = \frac{-i\Omega_R}{V}(1 - 2\langle \hat{A}_{22} \rangle). \quad (2.59)$$

The structure is the same as in free space, with different V due to $g \neq 0$. Because of the weakly pumped cavity, this correction is negligibly small, compare Eq. (2.56).

The term proportional to Ω_R in Eq. (2.58) is also identical to the structure in free-space. The other term,

$$R = \frac{\kappa}{\Gamma} \langle \hat{a}^\dagger \hat{a} \rangle > 0, \quad (2.60)$$

based on the SPE-cavity coupling, describes the energy sharing between the excitations of SPE and cavity mode discussed in the previous subsection. Though we argued $\langle \hat{a}^\dagger \hat{a} \rangle$ is low in our setup, we see the amount of excitation taken from the SPE is scaled by the prefactor $\kappa/\Gamma \approx 36$. Note that this term is always positive. It is responsible for the purification, so we denote R as the purification rate.

Considering R as a positive parameter in Eqs. (2.57) and (2.58) yields

$$\langle \hat{A}_{22} \rangle = \frac{2\Omega_R}{\Gamma} \Im \langle \hat{A}_{21} \rangle - R, \quad (2.61)$$

$$\langle \hat{A}_{12} \rangle = \frac{-i\Omega_R}{V}(1 - 2\langle \hat{A}_{22} \rangle). \quad (2.62)$$

Now we can apply the same formalism as in free space by splitting the term for $\langle \hat{A}_{21} \rangle = \langle \hat{A}_{12} \rangle^*$ into real and imaginary part and inserting it into $\langle \hat{A}_{22} \rangle$.

$$\Im \langle \hat{A}_{21} \rangle = \frac{\Omega_R}{|V|^2} \Re[V](1 - 2\langle \hat{A}_{22} \rangle), \quad (2.63)$$

$$\langle \hat{A}_{22} \rangle = \frac{2\Omega_R}{\Gamma|V|^2} \Re[V](1 - 2\langle \hat{A}_{22} \rangle) - R. \quad (2.64)$$

We can define a new quantity \tilde{z} akin to the free-space variable z as

$$\tilde{z} = \frac{2\Omega_R^2}{\Gamma|V|^2} \Re[V]. \quad (2.65)$$

Again, the deviations of these parameters from free-space values stem from $g \neq 0$. For the parameters of our example, these correction are small, yielding $\Re[V] \approx \frac{\Gamma}{2}$, and therefore $\tilde{z} \approx z$. With these results we eventually obtain

$$\langle \hat{A}_{22} \rangle = \frac{z - R}{1 + 2z} < \frac{z}{1 + 2z}, \quad (2.66)$$

$$|\langle \hat{A}_{12} \rangle|^2 = \frac{z(1 + 2R)^2}{(1 + 2z)^2} > \frac{z}{(1 + 2z)^2}. \quad (2.67)$$

As argued above, due to the positivity of the purification rate R , the excitation of the SPE is reduced, while the coherence is increased. The value of z can be controlled simply via tuning the SPE or changing the laser intensity, so that we can tailor our system to a cavity resonance. The method of choice would thus be to tune the parameters in such a way that the free-space SPE excitation would be slightly above the excitation for maximal optimized squeezing when at a cavity resonance. There, the quantum state of the SPE should be purified and the squeezing in the fluorescence optimized.

2.2.6. Stability against dissipative environments

With the physical background on how the purification works for general SPEs, let us turn to the more realistic description of a quantum dot in a semiconductor microcavity, by applying the different dissipative channels, compare Subsec. 2.1.1. We will consider pure dephasing, and incoherent pumping of dot or cavity mode [101, 102, 103] separately to analyze how much each channels affects the squeezing. Note that there are other descriptions of dissipative channels, see e.g. [71], which are not considered here. However, the ones to be discussed are well established as the main influences in semiconductor microcavities and, thus, yield a sufficiently realistic picture for our purpose.

Nonradiative dephasing

Nonradiative or pure dephasing of the quantum dot, described by the additional Lindblad term $\mathcal{L}_{\hat{A}_{22}}[\hat{\rho}]$ is a second decay channel for the quantum-dot coherence, but not for its excitation since $\text{Tr}\{\hat{A}_{22}\mathcal{L}_{\hat{A}_{22}}[\hat{\rho}]\} = 0$. The relation between coherence and excitation is essential for squeezing of the SPE fluorescence. Thus, dephasing is in general destructive for squeezing. Let us first study the analytically solvable case in free space [29], before comparing it with cavity-assisted squeezing. The rate of radiationless dephasing is given by Γ_D . Hence, the new master equation, compare Eq. (2.44), reads as

$$\frac{d\hat{\sigma}_{\text{fs}}}{dt} = \frac{1}{i\hbar}[\hat{H}_{\text{fs}}, \hat{\sigma}_{\text{fs}}] + \frac{\Gamma}{2}\mathcal{L}_{\hat{A}_{12}}[\hat{\sigma}_{\text{fs}}] + \frac{\Gamma_D}{2}\mathcal{L}_{\hat{A}_{22}}[\hat{\sigma}_{\text{fs}}]. \quad (2.68)$$

The excitation and coherence may again be described with a positive quantity z_D :

$$z_D = \left(1 + \frac{\Gamma_D}{\Gamma}\right) \frac{\Omega_R^2}{\left(\frac{\Gamma + \Gamma_D}{2}\right)^2 + \delta_x^2}, \quad (2.69)$$

$$\langle \hat{A}_{22} \rangle = \frac{z_D}{1 + 2z_D}, \quad (2.70)$$

$$|\langle \hat{A}_{12} \rangle|^2 = \frac{1}{1 + \frac{\Gamma_D}{\Gamma}} \frac{z_D}{(1 + 2z_D)^2}. \quad (2.71)$$

The structure of the solution of the excitation $\langle \hat{A}_{22} \rangle$ is equal to the case $\Gamma_D = 0$, but with the new quantity z_D as scaling parameter. Due to the large detuning $|\delta_x| \gg \Gamma_D$ in our

2. Quantum dots in semiconductor microcavities

example, z_D increases with increasing Γ_D as

$$z_D \approx \left(1 + \frac{\Gamma_D}{\Gamma}\right) \frac{\Omega_R^2}{\delta_x^2} = \left(1 + \frac{\Gamma_D}{\Gamma}\right) z. \quad (2.72)$$

The coherence on the other hand decreases due to the prefactor, yielding

$$|\langle \hat{A}_{12} \rangle|^2 \approx \frac{z}{(1 + 2z_D)^2}. \quad (2.73)$$

The limit for vanishing squeezing is given for $\Gamma_D = \Gamma$, where

$$\frac{\langle : (\Delta \hat{E})^2 : \rangle_{\text{fs}}}{|\chi|^2} = \left(\frac{2z_D}{1 + 2z_D} \right)^2 > 0. \quad (2.74)$$

From a physical point of view, the average time until a photon is emitted, $T_1 = \frac{1}{\Gamma}$, becomes as long as the average coherence time of the photon $T_2 = \frac{2}{\Gamma + \Gamma_D}$. Hence, on average, emitted photons have no coherence at the time they are emitted, and the light can not be squeezed.

Dephasing is considered a strong dissipative effect in semiconductor microcavities, compare, e.g., fit-parameters for Γ_D in [101]. Therefore, squeezed-light emission from a quantum dot seems very difficult in comparison with atomic fluorescence in free space. However, the cavity-induced purification process also stabilizes the emission against dephasing as shown in the following. We apply the formalism from Eqs. (2.54)-(2.67) to the master equation

$$\frac{d\hat{\rho}}{dt} = \frac{1}{i\hbar} [\hat{H}', \hat{\rho}] + \frac{\Gamma}{2} \mathcal{L}_{\hat{A}_{12}}[\hat{\rho}] + \frac{\kappa}{2} \mathcal{L}_{\hat{a}}[\hat{\rho}] + \frac{\Gamma_D}{2} \mathcal{L}_{\hat{A}_{22}}[\hat{\rho}], \quad (2.75)$$

where \hat{H}' is given by Eq. (2.30). As in the free-space case with dephasing, the values of V and z change to

$$V_D = V + \frac{\Gamma_D}{2}, \quad z_D = \frac{2\Omega_R^2}{\Gamma|V_D|^2} \Re[V_D]. \quad (2.76)$$

The value V_D is only slightly different from its free-space counterpart (with dephasing). As the dephasing terms do not couple to the cavity mode or $\langle \hat{A}_{22} \rangle$, the purification rate R remains the same. The values for the quantum-dot parameters become

$$\langle \hat{A}_{22} \rangle = \frac{z_D - R}{1 + 2z_D}, \quad (2.77)$$

$$|\langle \hat{A}_{12} \rangle|^2 = \frac{1}{1 + \frac{\Gamma_D}{\Gamma}} \frac{z_D(1 + 2R)^2}{(1 + 2z_D)^2}. \quad (2.78)$$

As in the case without radiationless dephasing, Eqs. (2.57) and (2.58), we see the purification of the quantum dot based on a decrease of $\langle \hat{A}_{22} \rangle$ and an increase of $|\langle \hat{A}_{12} \rangle|^2$. The overall squeezing now reads as

$$\frac{\langle : (\Delta \hat{E})^2 : \rangle_{\text{cav}}}{|\chi|^2} = \frac{\langle : (\Delta \hat{E})^2 : \rangle_{\text{fs}}}{|\chi|^2} - \frac{2R}{1 + 2z_D} \left(1 + \frac{1}{1 + \frac{\Gamma_D}{\Gamma}} \frac{8(1 + R)}{1 + 2z_D} \right). \quad (2.79)$$

From inspecting Eq. (2.79), we might expect the purification effect to be bounded, as R was small compared to 1 in the previous discussion. However, the increase of Γ_D also increases $\langle \hat{A}_{22} \rangle$ while suppressing the quantum-dot coherence $|\langle \hat{A}_{12} \rangle|^2$. It does not suppress the Rabi-coupling via g . Hence, by increasing the pure dephasing rate, we also increase $\langle \hat{a}^\dagger \hat{a} \rangle$ and, therefore, R . This increase is further enhanced substantially near the cavity resonance. In Fig. 2.7, the purification rate can be seen for different dephasing rates Γ_D . Near the cavity resonance its increase becomes more pronounced when Γ_D increases. We note, that for $\Gamma_D = 8\Gamma$, R is about 30 times bigger at the cavity resonance, than for $\Gamma_D = 0$, making the second term in Eq. (2.79) significant.

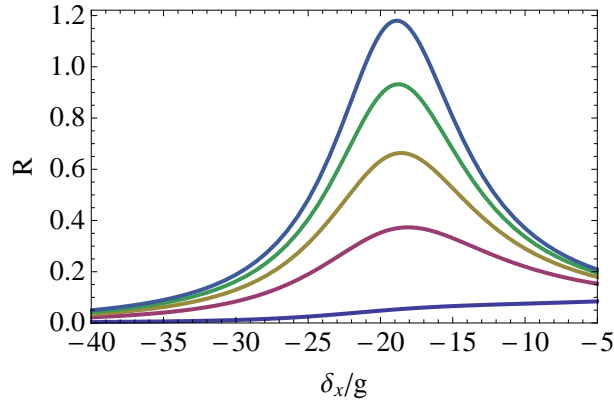


Figure 2.7.: Rate of purification R shown for different dephasing rates Γ_D . From bottom to top: $\Gamma_D/\Gamma = 0, 2, 4, 6, 8$. All other parameters are the same as in Fig. 2.6; after [IV].

The quantum-dot excitation decreases due to the increase of R , while the coherence near the resonance is almost insensitive to Γ_D , due the terms $(1+2R)^2$ and $1+\Gamma_D/\Gamma$ in Eq. (2.78) canceling each other. In Fig. 2.8, we plot the squeezing for the same dephasing rates as in Fig. 2.7. For increasing Γ_D , the scope of the cavity resonance and thus purification and optimized squeezing become narrower but much more pronounced. Within that spectral region, squeezing persists even for large dephasing. The free-space maximal value for squeezing, obtained only for $\Gamma_D = 0$, is now achievable for Γ_D up to around 3.24Γ . Keep in mind, in free-space fluorescence, squeezing vanishes for $\Gamma_D = \Gamma$. In our optimized scenario the limit for vanishing squeezing is $\Gamma_D = 7.47\Gamma$. By tailoring a semiconductor microcavity to parameters preferential for optimized squeezing, it seems reasonable to assume, that pure dephasing as an obstacle to the observation of squeezing can be overcome.

Incoherent pumping of the quantum dot

The coupling of a quantum dot to phonons enhances incoherent pumping to the dot. Incoherent driving does not create any coherence while increasing the excitation, which

2. Quantum dots in semiconductor microcavities

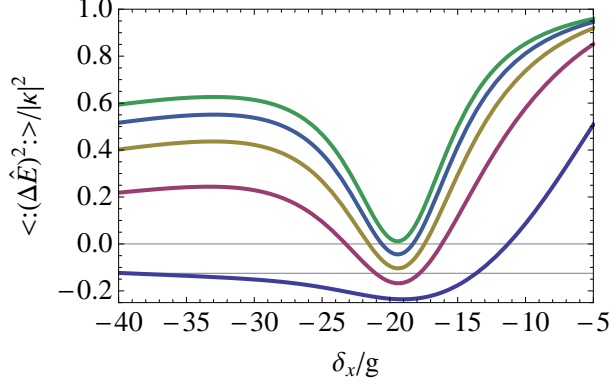


Figure 2.8.: Phase-optimized, normally-ordered field variance of the quantum-dot fluorescence for the same radiationless dephasing rates Γ_D as in Fig 2.7 (again from bottom to top). All other parameters are the same as in Fig. 2.6. Maximal free space squeezing ($-1/8$) and vanishing squeezing are indicated by the horizontal lines; after [IV].

resembles a depurification process, similar to pure dephasing. Assuming a rate of incoherent pumping P_x , we can analyze the fluorescence squeezing under coherent and incoherent pumping both in free space and in the cavity.

In the free space scenario, Eq (2.44), we supplement it with the Lindblad-term for incoherent pumping,

$$\frac{d\hat{\sigma}_{\text{fs}}}{dt} = \frac{1}{i\hbar}[\hat{H}_{\text{fs}}, \hat{\sigma}_{\text{fs}}] + \frac{\Gamma}{2}\mathcal{L}_{\hat{A}_{12}}[\hat{\sigma}_{\text{fs}}] + \frac{P_x}{2}\mathcal{L}_{\hat{A}_{21}}[\hat{\sigma}_{\text{fs}}]. \quad (2.80)$$

The system can again be solved analytically and its steady state reads as

$$z_x = \frac{\Omega_R^2}{(\frac{\Gamma+P_x}{2})^2 + \delta_x^2} \approx z, \quad (2.81)$$

$$\langle \hat{A}_{22} \rangle = \frac{z_x + \frac{P_x}{\Gamma+P_x}}{1 + 2z_x}, \quad (2.82)$$

$$|\langle \hat{A}_{12} \rangle|^2 = \frac{z_x}{(1 + 2z_x)^2} \left(\frac{\Gamma - P_x}{\Gamma + P_x} \right)^2 = \frac{z_x(1 - 2\frac{P_x}{\Gamma+P_x})^2}{(1 + 2z_x)^2}. \quad (2.83)$$

The structure of the solution surprisingly resembles the solution for the parameters in a cavity, Eqs. (2.66) and (2.67). Defining $P = P_x/(\Gamma + P_x) > 0$, we obtain the same equations with $P = -R$. Thus, the incoherent pumping acts directly as a depurification with rate P and counteracts the purification of the cavity.

To analyze the scenario in the cavity, we again follow the steps of the calculations in Eqs. (2.54)-(2.67) for the master equation

$$\frac{d\hat{\rho}}{dt} = \frac{1}{i\hbar}[\hat{H}', \hat{\rho}] + \frac{\Gamma}{2}\mathcal{L}_{\hat{A}_{12}}[\hat{\rho}] + \frac{\kappa}{2}\mathcal{L}_{\hat{a}}[\hat{\rho}] + \frac{P_x}{2}\mathcal{L}_{\hat{A}_{21}}[\hat{\rho}]. \quad (2.84)$$

The prefactor V and the purification rate R change in this case to V_x and R_x , respectively, while z stays almost the same, yielding

$$V_x = i\delta_x + \frac{\Gamma + P_x}{2} + \frac{g^2}{i\delta_c + \frac{\kappa}{2}} = V + \frac{P_x}{2}, \quad (2.85)$$

$$z_x = \frac{2\Omega_R^2 \Re[V_x]}{\Gamma + P_x |V_x|^2} \approx \frac{\Omega_R^2}{|V_x|^2} \approx z, \quad (2.86)$$

$$R_x = \frac{\kappa}{\Gamma + P_x} \langle \hat{a}^\dagger \hat{a} \rangle, \quad (2.87)$$

$$\langle \hat{A}_{22} \rangle = \frac{z_x + P - R_x}{1 + 2z_x}, \quad (2.88)$$

$$|\langle \hat{A}_{12} \rangle|^2 = \frac{z_x(1 - 2P + 2R_x)^2}{(1 + 2z_x)^2}. \quad (2.89)$$

The solution is similar to the case of no incoherent pumping with R_x and P defining the new purification rate

$$\tilde{R}_x = R_x - P = \frac{\kappa \langle \hat{a}^\dagger \hat{a} \rangle - P_x}{\Gamma + P_x}. \quad (2.90)$$

The steady-state averages of the quantum dot are now identical to Eqs. (2.66) and (2.67) with \tilde{R}_x instead of R . Consequently, they have the same behavior, but with \tilde{R}_x not limited to positive values. Hence, by tuning through the cavity resonance, when \tilde{R}_x changes sign, the cavity-induced effect changes from depurification to purification and back.

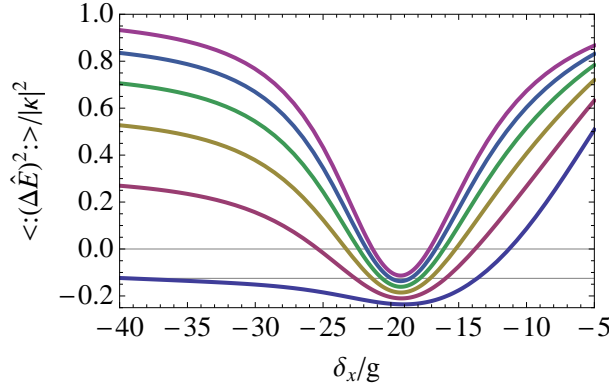


Figure 2.9.: Squeezing of the quantum-dot fluorescence for different incoherent pumpings P_x . From bottom to top: $P_x/\Gamma = 0, 0.2, 0.4, 0.6, 0.8, 1$. All other parameters and the horizontal lines are the same as in Fig. 2.6; after [IV].

Incoherent pumping within our model description is limited to $P_x \leq \Gamma$, with $P_x = \Gamma$ being the saturation case. In free space saturation means $\langle \hat{A}_{22} \rangle = 1/2$ and $|\langle \hat{A}_{12} \rangle|^2 = 0$. In our case however, even for $P_x = \Gamma$, we find purification for $\tilde{R}_x > 0$. Furthermore, due to $\kappa \gg \Gamma \geq P_x$, near the cavity resonance $R_x \gg P$ and $\tilde{R}_x \approx R_x$. Therefore, even in saturated scenario, we can expect strong field-noise suppression in a narrow spectral region.

2. Quantum dots in semiconductor microcavities

The phase-optimized, normally-ordered field variance is depicted in Fig. 2.9 for different incoherent pumping rates $P_x \leq \Gamma$. As expected, the squeezing persists around the cavity resonance even for the saturation case and is almost as strong (-0.113) as the free-space maximal squeezing (-0.125). Outside the resonance on the other hand, the incoherent pumping destroys the coherence very fast yielding an incoherent emission. For comparison, we note, that in free space for saturation, $\langle : (\Delta \hat{E})^2 : \rangle_{\text{fs}} / |\chi|^2 = 1$.

Incoherent pumping of the cavity

In difference to the quantum dot, the cavity mode only indirectly couples to the phonons via the quantum dot, compare Eq. (2.6). Hence, as experienced in thermal experiments, a quantum-dot resonance shifts through a cavity resonance, which is almost unaffected by the temperature variation [104, 101]. An incoherent pumping of the cavity mode, described by rate P_c , is also limited by the cavity dissipative decay, $P_c \leq \kappa$. Due to the small coupling between cavity mode and phonons via the dot, it is justified to assume $P_c \ll \kappa$, compare [101].

As cavity pumping does not occur in free space, we limit the discussion to the cavity-assisted scenario, applying the methods of Eqs. (2.54)-(2.67) to the master equation

$$\frac{d\hat{\rho}}{dt} = \frac{1}{i\hbar}[\hat{H}', \hat{\rho}] + \frac{\Gamma}{2}\mathcal{L}_{\hat{A}_{12}}[\hat{\rho}] + \frac{\kappa}{2}\mathcal{L}_{\hat{a}}[\hat{\rho}] + \frac{P_c}{2}\mathcal{L}_{\hat{a}^\dagger}[\hat{\rho}]. \quad (2.91)$$

The changes of z and V are negligible, while R_c is significantly different to R . Overall, we find

$$V_c = i\delta_x + \frac{\Gamma}{2} + \frac{g^2}{i\delta_c + \frac{\kappa - P_c}{2}} \approx V, \quad (2.92)$$

$$z_c = \frac{2\Omega_R^2 \Re[V_c]}{\Gamma |V_c|^2} \approx \frac{\Omega_R^2}{|V_c|^2} \approx z, \quad (2.93)$$

$$R_c = \frac{\kappa - P_c}{\Gamma} \langle \hat{a}^\dagger \hat{a} \rangle, \quad (2.94)$$

$$\langle \hat{A}_{22} \rangle = \frac{z_c + P_c/\Gamma - R_c}{1 + 2z_c} = \frac{z_c - \tilde{R}_c}{1 + 2z_c}, \quad (2.95)$$

$$|\langle \hat{A}_{12} \rangle|^2 = \frac{z_c(1 - 2P_c/\Gamma + 2R_c)^2}{(1 + 2z_c)^2} = \frac{z_c(1 + 2\tilde{R}_c)^2}{(1 + 2z_c)^2}, \quad (2.96)$$

$$\tilde{R}_c = R_c - \frac{P_c}{\Gamma} = \frac{(\kappa - P_c)\langle \hat{a}^\dagger \hat{a} \rangle - P_c}{\Gamma}, \quad (2.97)$$

where in the last line we defined an effective purification rate, similar to \tilde{R}_x as in the previous case. Though the structure of the quantum-dot excitation and coherence look identical to the case before, the effective purification rates \tilde{R}_x and \tilde{R}_c are different. In contrast to P_x , P_c is limited by κ but not by Γ . Due to $\kappa \gg \Gamma$ it is possible to have parameters, where $\kappa \gg P_c > \Gamma$ holds. In that case, the incoherent cavity pumping can

suppress the squeezing substantially. Furthermore, the effect is especially visible near the cavity resonance. On the other hand, spectrally detuned from the cavity resonance the quantum-dot-cavity coupling is weak, yielding the free-space case. Thus, incoherent cavity pumping is an effect which is emphasized, like the purification, in the cavity resonance, and suppressed outside. In this sense, it is different from the other dissipative effects considered here and a limit for the purification itself.

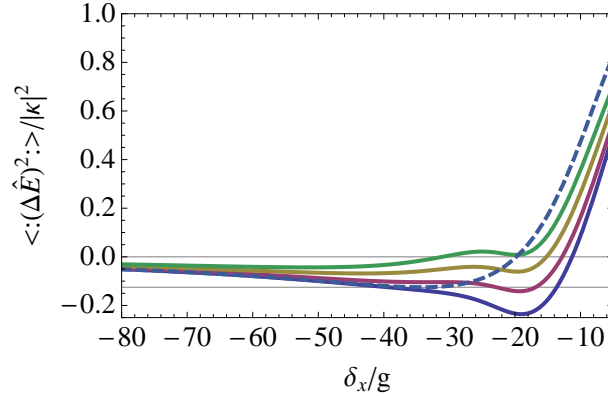


Figure 2.10.: Squeezing of the quantum-dot fluorescence for different incoherent pumpings P_c . From bottom to top (solid lines): $P_c/\Gamma = 0, 1, 2, 3$. The dashed line is the free space fluorescence squeezing. All other parameters and horizontal lines are as in Fig. 2.6; after [IV].

The squeezing under incoherent cavity pumping is shown in Fig. 2.10. Near the cavity resonance, squeezing becomes suppressed for increasing P_c , while outside the resonance we mainly observe the free-space behavior. However, it should be stressed, that we still find significant squeezing near the cavity-resonance for $P_c = 2\Gamma$, whereas in free space there would be no squeezing in that spectral region.

2.2.7. A method for observing single-photon-emitter-fluorescence squeezing

Despite the possibility of optimizing the squeezing in SPE fluorescence, detecting it remains a challenging task. So far, direct observation of the squeezing of SPEs, whether from atoms, quantum dots or other systems, remained elusive. As stated above, the main problem lies with the small collection efficiency of SPE fluorescence, which becomes critical in a balanced homodyne setup. A proposed solution to this problem is to apply a homodyne correlation setup [86, 87, 89]. In the following we consider a possible setup to determine the squeezing of the fluorescence with this method.

Consider the homodyne cross correlation setup from [87], depicted in Fig. 2.11. We superimpose the signal field \hat{E}_{SI} with a local oscillator E_{LO} , which is a coherent cw-light

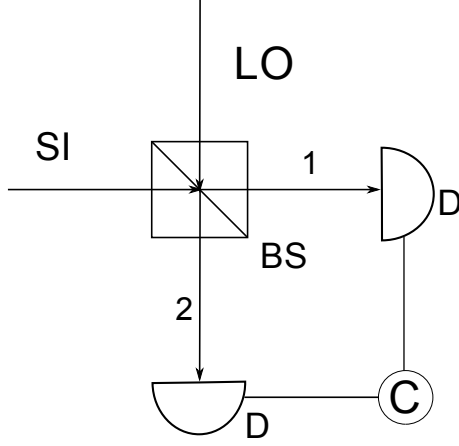


Figure 2.11.: Homodyne cross-correlation setup to measure the signal field SI, with LO the local oscillator [87]. After combining the fields in the beam splitter BS, the superimposed fields 1 and 2 are measured by correlating the two detector outputs D in C; after [IV].

source, in a 50:50 beam splitter. The two detectors record the output fields \hat{E}_1 and \hat{E}_2 , which are then cross-correlated. The detected cross-correlation reads as

$$\mathcal{G}^{(2,2)}(t_1, t_2) = \eta^2 \langle \hat{E}_1^{(-)}(t_1) \hat{E}_2^{(-)}(t_2) \hat{E}_2^{(+)}(t_2) \hat{E}_1^{(+)}(t_1) \rangle, \quad \text{with} \quad (2.98)$$

$$\hat{E}_1^{(+)} = \mathcal{T} \hat{E}_{\text{SI}} + \mathcal{R} E_{\text{LO}}, \quad \hat{E}_1^{(-)} = \left[\hat{E}_1^{(+)} \right]^\dagger, \quad (2.99)$$

$$\hat{E}_2^{(+)} = \mathcal{R} \hat{E}_{\text{SI}} + \mathcal{T} E_{\text{LO}}, \quad \hat{E}_2^{(-)} = \left[\hat{E}_2^{(+)} \right]^\dagger. \quad (2.100)$$

The transmission and reflection coefficients, \mathcal{T} and \mathcal{R} , respectively, include the complex phase induced by the beam splitter, while η describes the equal quantum efficiency for the two detectors, as well as the small collection efficiency.

The explicit form of $\mathcal{G}^{(2,2)}(t_1, t_2)$ for arbitrary beam splitter relations and times t_1, t_2 is decomposed into orders of E_{LO} in [87]. We are interested in steady state correlations, where only the time difference $\tau = t_2 - t_1$ is relevant. For equal times ($\tau = 0$) and applying the 50:50 beam-splitter property, the correlation function reduces to

$$\mathcal{G}^{(2,2)}(0) = \frac{\eta^2}{4} [\langle : \hat{I}_{\text{SI}}^2 : \rangle + I_{\text{LO}}^2 - 2I_{\text{LO}} \Re(\langle \hat{E}_{\text{SI}}^{(+2)} \rangle)]. \quad (2.101)$$

Here we used the intensities $\hat{I}_{\text{SI}} = \hat{E}_{\text{SI}}^{(-)} \hat{E}_{\text{SI}}^{(+)}$ and $I_{\text{LO}} = E_{\text{LO}}^2$. On the other hand, for $\tau \rightarrow \infty$ we obtain the decorrelated fields in the form

$$\mathcal{G}^{(2,2)}(\infty) = \frac{\eta^2}{4} \left[\langle \hat{I}_{\text{SI}} \rangle^2 + I_{\text{LO}}^2 - 2I_{\text{LO}} \left(\Re(\langle \hat{E}_{\text{SI}}^{(+)} \rangle^2) + |\langle \hat{E}_{\text{SI}}^{(+)} \rangle|^2 - \langle \hat{I}_{\text{SI}} \rangle \right) \right]. \quad (2.102)$$

Both correlations can be measured with the same setup.

The difference between the two correlations is

$$\Delta \mathcal{G}^{(2,2)} = \mathcal{G}^{(2,2)}(0) - \mathcal{G}^{(2,2)}(\infty) = \frac{\eta^2}{4} \left(\langle : \hat{I}_{\text{SI}}^2 : \rangle - \langle \hat{I}_{\text{SI}} \rangle^2 - I_{\text{LO}} \langle : (\Delta \hat{E}_{\text{SI}})^2 : \rangle \right). \quad (2.103)$$

The third term on the right hand side is proportional to the normally-ordered variance of the signal field, we are interested in. At this point we can turn to the light source under study. Due to the inability of a SPE to emit two photons at the same time, the second order moment $\langle : \hat{I}_{\text{SI}}^2 : \rangle$ is zero, leaving only

$$\Delta\mathcal{G}^{(2,2)} = -\frac{\eta^2}{4} \left(\langle \hat{I}_{\text{SI}} \rangle^2 + I_{\text{LO}} \langle : (\Delta\hat{E}_{\text{SI}})^2 : \rangle \right). \quad (2.104)$$

The first term in the brackets on the right hand side is obviously positive and the second only becomes negative for squeezed signal field, $\langle : (\Delta\hat{E}_{\text{SI}})^2 : \rangle < 0$. Therefore, positivity of $\Delta\mathcal{G}^{(2,2)}$ is proof of a squeezed signal field. Note, that even for weak squeezing, the amplitude of the second term may be enhanced by the local-oscillator intensity and only needs to be higher than the signal field intensity.

An implication from Eq. (2.104) seems to be to use a strong local oscillator to optimize chances for detecting squeezing. This is, however not true, as the given setup is not balanced and classical fluctuations of the local oscillator are not compensated [106]. A more complex balanced homodyne correlation setup overcoming this limitation was discussed in [88]. Consider the dominant classical fluctuation term in our setup, which is

$$\Delta\mathcal{G}_{\text{cl}}^{(2,2)} = \eta^2 I_{\text{LO}} \overline{(\delta E_{\text{LO}})^2}, \quad (2.105)$$

with $\overline{(\delta E_{\text{LO}})^2}$ being the variance of the classical field amplitude of the local oscillator E_{LO} . It can be experimentally determined if the signal channel is blocked and only the local oscillator enters the beam splitter. The classical noise may shift the correlation in Eq. (2.104) to the positive side. Accordingly the squeezing term must be stronger than the classical noise and our final squeezing condition reads as

$$\Delta\mathcal{G}^{(2,2)} > \Delta\mathcal{G}_{\text{cl}}^{(2,2)}. \quad (2.106)$$

3. Excitons in quantum wells

In a semiconductor quantum well multiple excitons can be excited. For not too strong excitation, the formalism in Eq. (1.15) applies. In quantum wells, the excitons are confined to two dimensions and restricted in the third. Therefore they can not couple freely to incoming light fields. The formation of polaritons in the restricted direction is suppressed, and the 'bare' excitons are the light-field emitters. Due to the roughness of the well boundary, excitons form localized structures, exciton spots (ESs), which can be seen as a group of multiple excitons in a near identical quantum state. Consequently, the excitons can act collectively, thus enhancing the coupling to the laser field modes. In [V] the fluorescence of these collective excitations in a GaAs quantum well was analyzed. The experiments on the respective probe have been provided by the group of Prof. Stolz. Combining an effective description of the exciton dynamics with the input-output formalism for the light propagation in the medium, and the medium's response, we can reobtain the exciton emission spectra and the quantum well emission spectra. From the results of these calculations and the comparison with experimental spectra, we are able to study the quantum properties of the light fields.

3.1. Experiments on the multiple-quantum-well sample

A quantum well is a quasi two-dimensional structure of a given semiconductor material. The confining third dimension is much smaller than the electronic transition wavelengths of the excitonic systems that are studied. Hence, the quantum well does not act as a cavity as possible standing waves are far offresonant. Due to this confinement the dipole of excitons is fixed in a plane. On both sides of the well a second semiconductor medium is coated with similar lattice constant (to avoid deforming the active layer crystal structure), but larger band gap (to suppress exciton excitations in the passive layers). All these structures are deposited, layer by layer on a substrate to form the quantum-well structure. The quantum well under study was created via molecular beam epitaxy [109] in Bochum [110]. Molecules of the specific layer are shot onto a substrate with a known growth rate, until the expected thickness is reached. Because of the statistical nature

3. Excitons in quantum wells

of the procedure, the surface of the well is rough, yielding localization centers for the excitons [111, 112, 113].

This quantum well has been the focus of extensive experimental research before [111, 112, 113, 114, 41]. Its structure is sketched in Fig. 3.1, on the left. It consists of multiple active GaAs layers of different well thickness, each separated by a spacer of 13 alternating layers of AlAs and GaAs. These separation layers suppress the generation of exciton states outside the active GaAs layers, as the band gap of AlAs is 3.13 eV compared to the 1.52 eV of GaAs [115].

In the following we will shortly review the experiments, performed in the group of Prof. Stolz, that are relevant to our analysis. The details of the experimental setup are documented in [114, 41]. With a specially developed 4π -microscope-cryostat the sample was contained in a liquid He-circle. This allowed to achieve a high collection efficiency of the emitted light. The performed experiments were threefold:

- i) Using either a He-Ne-laser for photoluminescence or a tunable semiconductor cw-laser for resonance fluorescence, the emission spectra of the emitted light fields were recorded very accurately. The limitation of the spectral resolution is given by the detector resolution, revealed in the width of the Rayleigh peak.
- ii) Applying a cooled CCD-chip, the spatial intensity distribution was observed with a spatial resolution of 350 nm FWHM, compare Fig. 3.1, on the right.
- iii) By varying the temperature of the He in the cryostat the emission properties were studied at different sample temperatures. Hence, the increasing influence of thermal fluctuations and phonon-coupling could be analyzed.

The spatial studies showed, that within the broad laser spot, the exciton spots arise as strong intensity fluctuations. The patterns are random as the surface roughness forming them is also random [113]. The advantage of this origin of the ES formation is, that the spatial fluctuations are reproducible for different experimental setups. With increasing temperature, the ESs become larger, until they start combining, forming even larger, inhomogeneously broadened, ESs.

Applying a pinhole, spectral studies on a single ES have been performed, yielding fluorescence spectra such as given in Fig. 3.2. The spectra are plotted for different laser powers at constant laser frequency and fixed temperature. One can see the sharp Rayleigh-peak at the laser resonance, which is given due to the spectral width of the camera being at about $10 \mu\text{eV}$. It represents the coherent scattering part of the exciton emission and is discussed in the literature under the term resonant Rayleigh scattering [116, 117, 118, 119, 120]. The resonant Rayleigh scattering of a speckle structure has also been studied [121, 122].

3.1. Experiments on the multiple-quantum-well sample

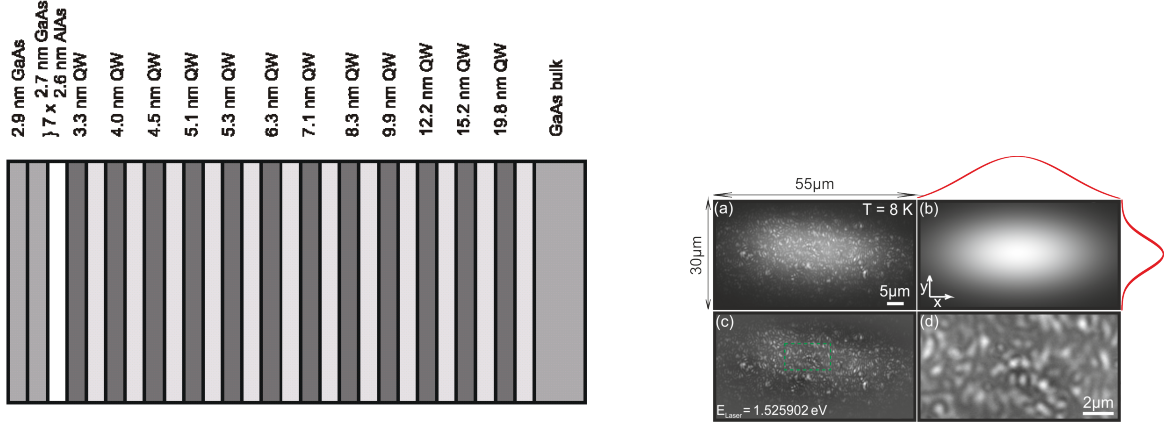


Figure 3.1.: Left: Structure of the quantum well probe. Right: Spatial intensity distribution of the quantum well fluorescence, both taken from [41]. (a) raw data; (b) calculated laser background (2D-Gaussian as indicated by red curves); (c) data without background; (d) magnified part of (c).

However, these analyses are limited to the coherent part of the radiation, underestimating the incoherent contribution.

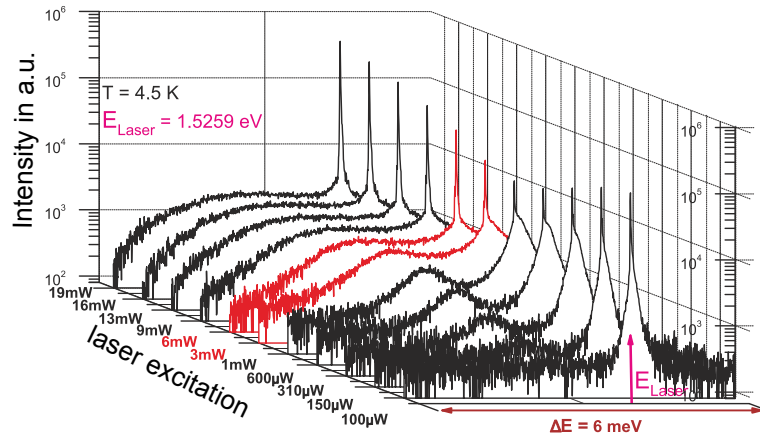


Figure 3.2.: Optical fluorescence spectra for one ES and different excitation strengths. The bright (red) lines indicate the Mott-transition; after [114].

As can be clearly seen from the logarithmic scale, a significant incoherent emission, a much broader resonance from the excitons, appears. When increasing the laser power, this resonance shifts away from the laser frequency and broadens further. While the maximum spectral intensity of this incoherent emission is small compared to the Rayleigh peak, it does contribute substantially to the total emission, compare [41]. Hence, it can not be ignored in interpreting the spectra.

There has been some theoretical discussion concerning the spectra in Fig. 3.2, see [113, 41, 123, 124, 122]. In [123, 124], on the one hand, the Greens function technique was

3. Excitons in quantum wells

applied to demonstrate the spectral shifting of the imaginary part of the quantum-well-susceptibility resonance. For very thin films, this resonance is proportional to the absorption of the medium, which is assumed to be represented by the incoherent emission spectrum, compare [125]. It was argued, that the resonance shift is based on screening effects of the excitons. Based on this interpretation the resonance should shift in different spectral directions, depending on the sample temperature. This temperature dependence was indeed observed in the experiments [114, 41], but with much lower magnitude of the shift, than predicted by theory in [123]. The mentioned publications mainly focused however on the Mott transition of the excitons, which is not discussed in this thesis.

The susceptibility of the medium does not include the resonant Rayleigh scattering, and hence, not the full emission. Therefore, in [113], a quantum-optical model for exciton fluorescence was proposed and analyzed. In this model, the exciton spot was described by a two-level atom, coupling to the laser light, and generating a coherent and an incoherent emission spectrum. The model of a two-level atom was based on previous considerations [121, 111], as well as the assumption of single excitons within the small spots. If the exciton would be bosonic (very low density limit) a coherent pumping would only yield a coherent state, and thus only resonant Rayleigh scattering. The problem that arises with this model is two-fold. From a many-body description, the resonance shift is an indicator of increasing exciton density. Hence, even if for the lowest intensity we have only one exciton, for higher densities the model should be flawed. From a quantum-optical perspective, the shift can not occur at all. Due to energy conservation, the model requires, that the fluorescence spectrum is symmetric with respect to the laser frequency. Hence, if the excitons shift – which can be simply modeled as a variable resonance frequency of the medium – we would obtain first a broadening on both sides of the laser frequency, and later a splitting, comparable, but not equal to Rabi splitting of strong light-matter coupling, see [3, 4].

In general, a many-body approach to calculate the spectra would be to solve the semiconductor Bloch equations for the system, see [38] for details. These equations lead to an infinite hierarchy of coupled correlations, which need to be truncated [126]. Examples for this method include the luminescence (incoherent pumping) of a quantum dot [127] or a quantum well [128]. Considering our interest in quantum phenomena, this method has the limitation of cutting off correlations, which might be of significant relevance for the quantum behavior. A purely quantum-optical description on the other hand, starting from an exciton Hamiltonian as Eq. (1.15) does not in itself consider the medium's response. A first approach to this problem was done in [129], where quantum light fields passing through an excited semiconductor have been analyzed applying both the quantum-optical input-output formalism to obtain field-correlation functions, as well as the Greens- function

methods to relate these correlations to the excitons.

Overall, the theoretical interpretations of the quantum-well spectra are unsatisfying. Yet, they give the following hints: the response of the medium, given by its susceptibility, is partly responsible for the incoherent emission, as it describes the resonant shift in the correct direction. It also indicates the increase in exciton numbers within one spot. The occurrence of an incoherent spectrum proves, that the excitons can not be noninteracting bosons, while the asymmetry between coherent and incoherent spectrum is not explained at all. In [V] we applied these hints and the concepts from [129] to interpret the quantum-well spectra.

3.2. Theoretical description of emission spectra

3.2.1. Exciton Hamiltonian

Let us start with a model for the excitons. In the low density (i.e. low pumping) limit, the excitons can be considered as interacting bosons. They are described by creation and annihilation operators \hat{a}_n^\dagger and \hat{a}_n , respectively, $[\hat{a}_n, \hat{a}_k^\dagger] = \delta_{n,k}$, and are driven by a cw-laser of frequency ω_L . All excitons acquire a nearly identical state within one ES yielding the following reasonable approximations. For all N excitons of the spot the transition frequency $\omega_x = \omega_L + \delta$ is the same, where many-body induced resonance shifts are included. They have a negligible momentum due to their localization. As the exciting laser spot is much larger than the ES size, compare Fig. 3.1 on the right, every exciton is coupled to the laser field with the same Rabi-frequency Ω_R . Likewise, also the exciton-exciton interaction described by a Kerr-nonlinear contribution, should have the same strength G for all excitons [130, 131, 132].

The Hamiltonian of the excitons coupled to the laser field in the frame rotating with ω_L reads as

$$\hat{H} = \hbar \sum_{n=1}^N \{ \delta \hat{a}_n^\dagger \hat{a}_n + \Omega_R \hat{a}_n e^{i\phi_n} + \Omega_R^* \hat{a}_n^\dagger e^{-i\phi_n} \} + \hbar G \sum_{n,k=1}^N \hat{a}_n^\dagger \hat{a}_k^\dagger \hat{a}_k \hat{a}_n. \quad (3.1)$$

Furthermore, the energy relaxation of each exciton is modeled via a Lindblad-term with rate Γ , yielding the master equation

$$\dot{\hat{\rho}} = \frac{1}{i\hbar} [\hat{H}, \hat{\rho}] + \frac{\Gamma}{2} \mathcal{L}[\hat{\rho}], \quad \mathcal{L}[\hat{\rho}] = \sum_{n=1}^N \mathcal{L}_{\hat{a}_n}[\hat{\rho}] = \sum_{n=1}^N (2\hat{a}_n \hat{\rho} \hat{a}_n^\dagger - \hat{a}_n^\dagger \hat{a}_n \hat{\rho} - \hat{\rho} \hat{a}_n^\dagger \hat{a}_n). \quad (3.2)$$

This system is difficult to analyze, as we have no knowledge about the phases ϕ_n and the exciton number N . Hence, we will transform it into an effective master equation describing a collective N -exciton state.

3. Excitons in quantum wells

The size of the exciton spot can become comparable to the optical wavelength due to the limited resolution of the camera (FWHM = 350 nm). Thus, the relative phases ϕ_n have to be taken into account for our considerations. We may define an overall average Rabi frequency,

$$\overline{\Omega_R} = \left(\frac{1}{N} \sum_{n=1}^N e^{i\phi_n} \right) \Omega_R. \quad (3.3)$$

By adjusting a global phase, we assume $\overline{\Omega_R}$ to be real and positive. The ratio between the overall average Rabi frequency and the single exciton Rabi frequency, $\overline{\Omega_R}/|\Omega_R| \leq 1$ is now a measure of the degree of phase matching between the different excitons. For uncorrelated ϕ_n -values, the ratio decreases due to destructive interference from the emission of the individual excitons. However, if all excitons couple with the same phase ϕ , $\overline{\Omega_R} = |\Omega_R|$ would be independent of N . In that case, the excitons collectively couple to the laser mode and thus establish a scenario called steady-state superfluorescence [133, 134, 135, 136, 137]. We will reconsider the question of phase matching after simulating the fluorescence spectra and obtaining data for this ratio.

With the average Rabi frequency, we can define an effective Hamiltonian H_{eff} for our system, that reads as

$$\hat{H}_{\text{eff}} = \hbar \sum_{n=1}^N \{ \delta \hat{a}_n^\dagger \hat{a}_n + \overline{\Omega_R} (\hat{a}_n + \hat{a}_n^\dagger) \} + \hbar G \sum_{n,k=1}^N \hat{a}_n^\dagger \hat{a}_k^\dagger \hat{a}_k \hat{a}_n. \quad (3.4)$$

Now, let us introduce a transformation, which describes the excitons by a single collective bosonic excitation:

$$\hat{A} = \frac{1}{\sqrt{N}} \sum_{n=1}^N \hat{a}_n, \quad [\hat{A}, \hat{A}^\dagger] = 1. \quad (3.5)$$

We can derive the commutators

$$[\hat{A}, \sum_{n=1}^N \hat{a}_n^\dagger \hat{a}_n] = [\hat{A}, \hat{A}^\dagger \hat{A}], \quad (3.6)$$

$$[\hat{A}, \sum_{n,k=1}^N \hat{a}_k^\dagger \hat{a}_n^\dagger \hat{a}_k \hat{a}_n] = N[\hat{A}, \hat{A}^{\dagger 2} \hat{A}^2]. \quad (3.7)$$

Keep in mind, that the source field of the emission is coupled the excitation of the internal emitters, i.e. $\hat{E}_S^{(+)} \propto \hat{A}$ in dipole coupling. Thus, the correlation properties of the emitted light are characterized by the correlation properties of collective exciton operators \hat{A} . Therefore the commutators in Eqs. (3.6,3.7) can be used to describe the source field correctly with an effective, collective Hamiltonian

$$\hat{H}' = \hbar \delta \hat{A}^\dagger \hat{A} + \hbar \Omega'_R (\hat{A} + \hat{A}^\dagger) + \hbar G' \hat{A}^{\dagger 2} \hat{A}^2 \quad (3.8)$$

with $\Omega'_R = \sqrt{N} \overline{\Omega_R}$ and $G' = NG$. Thus, we reobtained for the Hamiltonian the same form as in Eq. (1.18). However, due to the increasing interaction of cooperative excitons, the nonlinear contribution as well as the Rabi frequency scale with the number of emitters.

Similarly, it can be shown that, using the commutation relation [29]

$$[\hat{A}^\ell, \hat{a}_n^\dagger] = \frac{\ell}{\sqrt{N}} \hat{A}^{\ell-1} \quad (3.9)$$

for $\ell \in \mathbb{N}$, the Lindblad term shows the equivalence

$$\text{Tr}[\hat{A}^{\dagger m} \hat{A}^k \mathcal{L}(\hat{\rho})] = \text{Tr}[\hat{A}^{\dagger m} \hat{A}^k (2\hat{A}\hat{\rho}\hat{A}^\dagger - \{\hat{A}^\dagger \hat{A}, \hat{\rho}\})] = -(m+k) \langle \hat{A}^{\dagger m} \hat{A}^k \rangle. \quad (3.10)$$

With the same argument for the field properties, we can state, that the total system of interest can be described by the effective master equation

$$\dot{\hat{\rho}} = \frac{1}{i\hbar} [\hat{H}', \hat{\rho}] + \frac{\Gamma}{2} \mathcal{L}_{\hat{A}}[\hat{\rho}], \quad (3.11)$$

with H' given in Eq. (3.8) and $\mathcal{L}_{\hat{A}}[\hat{\rho}]$ according to Eq. (2.4). Hence, the full cooperative dynamics of our system is identical to the single exciton case – but with modified coupling constants, depending on the number N of excitons in the spot. Note that Γ and δ do not scale with N . Thus, the effects of multiple excitons only enhance the pumping and the nonlinear contribution. Broadening of the resulting linewidth and increased detuning are based on many-body effects of the medium.

With this effective master-equation (3.11), the light fields emitted from the excitons, i.e. the exciton fluorescence can be determined. Specifically, the spectral density $S(\omega)$ at frequency ω of the fluorescence is given via the Wiener-Khintchine theorem [138] to be

$$S_W(\omega) \propto \Re \left[\int_0^\infty d\tau e^{-\left(i\omega + \frac{\Gamma_f}{2}\right)\tau} \lim_{t \rightarrow \infty} \langle \hat{A}^\dagger(t) \hat{A}(t + \tau) \rangle \right], \quad (3.12)$$

where Γ_f is the spectral width of the detector resolution. It is necessary to include this term in order to obtain a finite Rayleigh-Peak, with Γ_f being its linewidth. Furthermore, all correlation properties of the fields can be calculated to study nonclassical phenomena [139, 140]. However, the exciton emission spectrum $S_W(\omega)$ is not equal to the spectrum of the quantum well emission. The well itself acts as a dispersive and absorptive medium, which interacts with the incoming fields. Hence, the inclusion of the effects of light propagation through medium is necessary to obtain the correct fluorescent emission.

3.2.2. Input-output formalism and quantum-well-emission spectrum

A medium, which is irradiated, responds to the light fields, either by passively manipulating the traversing fields or by absorbing the photons and emitting an own light field.

3. Excitons in quantum wells

To account for these effects, an input-output formalism for light fields impinging onto a dielectric medium was developed [129]. It is based on the earlier Huttner-Barnett quantization [31]. There, it was shown, that for a nondispersive, nonabsorptive medium, Maxwell's equations can be directly quantized. The extension to the case of dispersive, absorptive medium was discussed in [32]. As dispersion and absorption change the fields on a quantum level, quantum noise is generated, to account for the commutation relations, compare [29, 30]. The noise operators that were included in the quantized Maxwell-equations act as noise sources. In [129], it was argued, that in case of semiconductor structures these noise operators are actually the polaritons, which are excited, by absorbing and then emitting the incoming light fields.

A basic aspect of the above discussions was the (quasi-)equilibrium state of the bosonic noise operators. This property was based on the fact, that the internal excitations in the medium represent a bath, to which the light fields couple. In our case of resonance fluorescence, the scenario is quite different. The quantum well is excited by the incoming light field itself, and the excitons are driven by the laser light, generating the emission spectrum (3.12). Consequently, the bosonic dynamics of the noise operators is substituted with the master equation (3.11). Furthermore, as the laser is the only light impinging on the quantum well, no other incoming signal is given.

With the knowledge about the influence of the medium, how does it affect the emission spectrum from the quantum well? When there is no incoming light field, the response of the medium reduces to the spontaneous emission of the excitons, which is the spectrum, scaled by the medium's absorption spectrum $a(\omega)$. From a physical point the interpretation is quite simple. The Wiener-Khintchine spectral density $S_W(\omega)$ describes the spectral density of emitted photons for the given excitons. However, the excitons must first be created by absorption of photons, meaning higher absorption rates will generate more excitons. The Wiener-Khintchine spectral density $S_W(\omega)$ can be seen as a potential for emission, the absorption spectrum $a(\omega)$ as the threshold for the emitters. Overall, we find, that the spectrum emitted from the quantum well can be given by

$$S(\omega) = a(\omega)S_W(\omega). \quad (3.13)$$

In order to clearly separate the two spectra, we will call them from now on emission spectrum of the excitons ($S_W(\omega)$) and the quantum well ($S(\omega)$). Correlations analyzed in Sec. 3.3 will also be subject to this notation.

The absorption spectrum follows from the transmission spectrum and reflection spectrum $t(\omega)$ and $r(\omega)$, respectively, as

$$a(\omega) = 1 - |t(\omega)|^2 - |r(\omega)|^2. \quad (3.14)$$

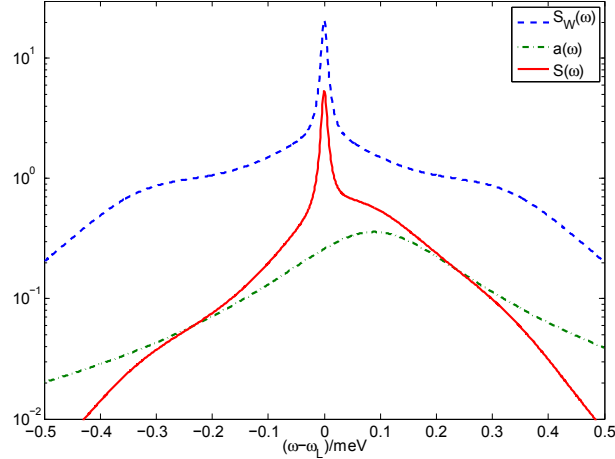


Figure 3.3.: Theoretical emission spectrum of the excitons (dashed) and the quantum well (solid). The dash-dotted line gives the absorption spectrum. The parameters are $\Gamma = 0.22$ meV, $G' = 0.45$ meV, $\Omega'_R = 0.16$ meV, $\delta = 0.1$ meV and the detector bandwidth $\Gamma_f = 0.0107$ meV; after [V].

The latter two, in turn, can be derived from the response of the medium. In the low density regime we consider a linear response, with the susceptibility $\chi(\omega)$ given by an oscillator model, compare [V],

$$\chi(\omega) = \frac{f}{\omega - \omega_X - i\frac{\Gamma}{2}} = \frac{f}{\omega - \omega_L - \delta - i\frac{\Gamma}{2}}. \quad (3.15)$$

Here f is the oscillator strength. The width Γ and resonance frequency ω_X of this oscillator model are equal to the exciton parameters in Eq. (3.2), as the excitons are the origin of the resonance in the medium.

Fig. 3.3, shows the different spectra, $S_W(\omega)$, $a(\omega)$, and $S(\omega)$ for the parameters given in the caption. The exciton spectrum is symmetric with respect to the laser frequency ω_L . This is a consequence of energy conservation. The incoherent part of this spectrum is due to the Kerr-nonlinearity. For even larger values of G' or δ , it would produce Rabi-splitting, see [141]. The absorption spectrum, on the other hand, is symmetric with respect to the exciton resonance at ω_X . Hence, the emission spectrum of the quantum well, $S(\omega)$ is asymmetric with an apparent incoherent spectrum shifted from the laser resonance. A few remarks on the spectrum. The apparent detuning of the exciton resonance from the laser frequency in $S(\omega)$ goes in the same direction (here to higher frequencies) as the actual detuning. However, its magnitude is substantially lower, indicating that such energy shifts appear suppressed in experiments. It thus resembles the observed phenomenon in experiments [114] where the laser-exciton shift seemed smaller than the susceptibility shift. The Rayleigh peak does not appear asymmetric, as the detector width Γ_f is much smaller than the absorption width Γ , $\Gamma_f \ll \Gamma$.

3. Excitons in quantum wells

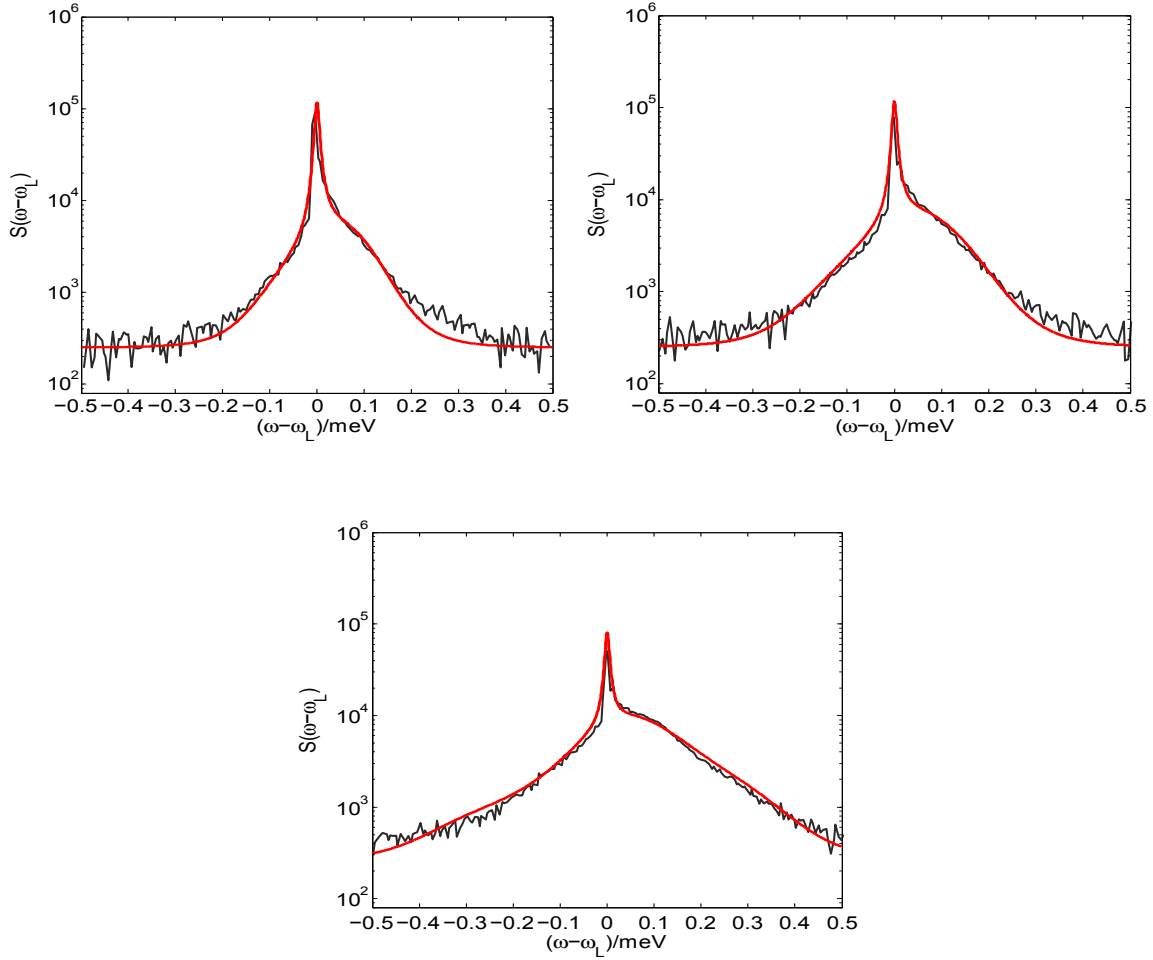


Figure 3.4.: Quantum well fluorescence spectra, comparison of theory (red) with experiment (black) for different laser powers P_L . From left to right: $P_L = 100 \mu\text{W}$, $150 \mu\text{W}$, $310 \mu\text{W}$; after [V].

We compare the experiments for the three laser powers $P_L = 100, 150$ and $310 \mu\text{W}$ with our theoretical model in Fig. 3.4. The fit parameters are given in Table 3.1. To compare the values for the different spectra, we added the index i to all quantities, to number the respective measurement. The ordering of the spectra is by increasing laser power P_L , so that $P_{L,i+1} > P_{L,i}$. The theoretical spectra are supplemented with a constant background to account for the detection noise in the experiment. This noise combined with the weak absorption $a(\omega)$ outside the absorption resonance ω_x suppresses physical effects at frequencies outside that resonance.

The detector width for all powers is $\Gamma_f = 0.0107 \text{ meV}$, much smaller than $\Gamma \geq 0.15 \text{ meV}$. The apparent smaller shift of the quantum-well spectrum compared to the shift of the absorption resonance occurs. However, the increase of the detuning δ with increasing laser power is very small, which yields two conclusions: On one hand the majority of the shift is based on the detuning of the laser from the absorption resonance, not on many-body

measurement i	1	2	3
$P_{L,i}/\mu\text{W}$	100	150	310
$\hbar G'_i/\text{meV}$	0.10	0.205	0.45
$\hbar\Omega'_{R,i}/\text{meV}$	0.045	0.075	0.16
$\hbar\delta_i/\text{meV}$	0.08	0.08	0.09
$\hbar\Gamma_i/\text{meV}$	0.15	0.20	0.22
$f_i/\text{a.u.}$	1.0	1.0	0.9
$\frac{G'_i}{G'_{i-1}}$	—	2.050	2.195
$\frac{P_{L,i-1}}{P_{L,i}} \left(\frac{\Omega'_{R,i}}{\Omega'_{R,i-1}} \right)^2$	—	1.852	2.202

Table 3.1.: Fit parameters for the different measured spectra and relations of these parameters concerning the phase matching of the exciton emission.

effects shifting the resonance itself. The apparent shifting with increased laser power is mainly due to the increase of the incoherent linewidth. As stated above, this increase is based on many-body effects and is not included within our Hamiltonian. On the other hand the data hints at a density of excitons, much lower than estimated in theory [123]. The increase of the linewidth Γ and detuning δ , as well as the decrease of the oscillator strength f for increasing laser power is comparably small. That indicates that many-body effects are not strong in this regime.

3.2.3. Superfluorescence of the quantum well

As a first implication of our simulation, let us analyze the degree of phase matching and steady-state superfluorescence. For that purpose, we analyze the two N dependent quantities Ω'_R and G' , for which we now have fit parameters, see Table 3.1. Besides the collective increase with \sqrt{N} , the single-exciton Rabi-frequency Ω_R also increases with the root of the laser power P_L . Hence, the pure N -dependence of the collective Rabi-frequency is given by $\Omega'_R/\sqrt{P_L}$. We consider the ratio

$$\frac{\overline{\Omega_R}}{|\Omega_R|} = \frac{1}{N} \left| \sum_{n=1}^N e^{i\phi_n} \right|. \quad (3.16)$$

In case of perfect phase matching, the right hand side of Eq. (3.16) becomes unity, leading to

$$\Omega'_R = \sqrt{N} \overline{\Omega_R} = \sqrt{N} |\Omega_R|, \quad (3.17)$$

which is equivalent to

$$\frac{(\Omega'_R)^2}{P_L} \propto G' \propto N. \quad (3.18)$$

3. Excitons in quantum wells

To compare with our simulated data, we again add an index $i = 1, 2$ to the quantities above, indicating different fluorescence spectra 1 and 2. This yields

$$\frac{P_{L,1}}{P_{L,2}} \left(\frac{\Omega'_{R,2}}{\Omega'_{R,1}} \right)^2 = \frac{G'_2}{G'_1} = \frac{N_2}{N_1}, \quad (3.19)$$

where N_i are the numbers of excitons involved in the respective spectrum.

The criterion for superfluorescence from an N -emitter system is the intensity increasing with N^2 [134, 137]. From Eq. (3.17), the fluorescence intensity I of the fields can be given as

$$I \propto \langle \hat{E}_S^{(-)} \hat{E}_S^{(+)} \rangle = N \langle \hat{A}^\dagger \hat{A} \rangle, \quad (3.20)$$

where the scaling with N stems from the normalization of \hat{A} in Eq. (3.5). For weak pumping and using Eq. (3.8), we obtain $\langle \hat{A}^\dagger \hat{A} \rangle \propto (\Omega'_R)^2$. This yields

$$I \propto N(\Omega'_R)^2 = N(\sqrt{N})^2 |\Omega_R|^2 \propto N^2 I_1, \quad (3.21)$$

with I_1 being the single exciton intensity, which is proportional to $|\Omega_R|^2$. Hence, the criterion for superfluorescent emission is fulfilled.

Likewise, we can estimate the dynamics for a random configuration of excitons without phase matching. A collective dipole coupling of the excitons to the pump field is suppressed due to destructive interference:

$$\left| \sum_{n=1}^N e^{i\phi_n} \right|^2 = \sum_{n,k=1}^N e^{i(\phi_n - \phi_k)} = \sum_{n=1}^N e^{i0} + \sum_{n \neq k}^N e^{i(\phi_n - \phi_k)} \approx N. \quad (3.22)$$

From the statistical distribution and Eq.(3.16), it follows, that

$$\Omega'_R = \sqrt{N} \overline{\Omega_R} = |\Omega_R|, \quad (3.23)$$

and, contrary to Eq. (3.19), $\frac{(\Omega'_R)^2}{P_L} = \text{constant}$, and

$$\frac{P_{L,1}}{P_{L,2}} \left(\frac{\Omega'_{R,2}}{\Omega'_{R,1}} \right)^2 = 1. \quad (3.24)$$

No N -dependence of $\Omega'_R = |\Omega_R|$ arises for such a random configuration. The intensity now reads as, in contrast to Eq. (3.21),

$$I \propto N |\Omega_R|^2 \propto N I_1, \quad (3.25)$$

which is only the incoherent increase of the intensity.

The last two lines in Table 3.1 give the left hand sides of Eqs. (3.19,3.24), respectively. The relative increase of G' and thus N is roughly two for each increase in laser power. From Eqs. (3.19,3.24) we can conclude, that the ratio in the last line of the table should

be unity for random phases, but the same value as the increase of G' for the case of superfluorescence. Intermediate values indicate a partial phase matching. The ratio in the last line significantly exceeds unity and, in particular, from the second to the third measurement its value is very close to the relative increase of G' . The phase matching is hence very good, and the excitons do emit steady-state superfluorescent light.

3.3. Quantum correlations

With the data from our simulation, we are able to compute arbitrary correlation functions of the exciton fields and the quantum-well fields. We will in the following analyze, how the quantum-well correlations follow from the exciton correlations and the absorption. Furthermore, we consider some specific nonclassical effects for the given quantum well [VI].

3.3.1. General correlations

In order to analyze field correlations, we have to consider how the internal fields of the excitons transform to the quantum-well-emission fields. The input-output formalism in [31, 32, 129] considers mode densities in the continuum of frequencies. For such field creation and annihilation operators, $\hat{b}^\dagger(\omega)$ and $\hat{b}(\omega)$, respectively, we have continuous commutation relations

$$[\hat{b}(\omega), \hat{b}^\dagger(\omega')] = \delta(\omega - \omega') \quad (3.26)$$

in comparison to the discrete mode decomposition used for the collective exciton operators \hat{A}^\dagger and \hat{A} , Eq. (3.5). In the discrete mode picture expectation values and correlations of the fields are integrals over the spectral densities of these field correlations. The simplest example is the commutation relation itself:

$$\int_{-\infty}^{\infty} d\omega' [\hat{b}(\omega), \hat{b}^\dagger(\omega')] = [\hat{A}, \hat{A}^\dagger] = 1. \quad (3.27)$$

Similarly, we find for the spectral density of the excitons

$$S_W(\omega) = \langle \hat{b}^\dagger(\omega) \hat{b}(\omega) \rangle = \frac{1}{2\pi} \int_{-\infty}^{\infty} d\tau e^{-i\omega\tau} \langle \hat{A}^\dagger(0) \hat{A}(\tau) \rangle = \langle \hat{A}^\dagger(0) \hat{\hat{A}}(\omega) \rangle. \quad (3.28)$$

In the second line we omitted the convolution with the detector resolution, set the stationary time argument $t = 0$ and performed the Fourier-transform on the Heisenberg-operator $\hat{A}(\tau)$ to obtain $\hat{\hat{A}}(\omega)$. $S_W(\omega)$ is the spectral intensity density of the exciton field and its integral gives simply the exciton intensity I_{Exc}

$$I_{\text{Exc}} = \langle \hat{A}^\dagger \hat{A} \rangle = \int_{-\infty}^{\infty} d\omega S_W(\omega). \quad (3.29)$$

3. Excitons in quantum wells

Due to the input-output formalism, the quantum-well spectral intensity density is scaled with the absorption spectrum, thus yielding for the measurable quantum-well intensity

$$I_{\text{QW}} = \int_{-\infty}^{\infty} d\omega S(\omega) = \int_{-\infty}^{\infty} d\omega a(\omega) S_{\text{W}}(\omega). \quad (3.30)$$

From this example we can conclude the formalism to obtain general normally-ordered field correlations. For simplicity we limit ourselves to steady-state correlations. We start from a correlation $f(0)$ of the exciton dynamics calculated by solving the master equation Eq. (3.11). The time-dependent function $f(t)$ is defined by assigning different time arguments t_j to all field operators in $f(0)$. We want to use the general rule of Fourier-transforms, that

$$f(0) = \frac{1}{2\pi} \int_{-\infty}^{\infty} d\omega \int_{-\infty}^{\infty} dt e^{-i\omega t} f(t), \quad (3.31)$$

in order to express $f(0)$ as the integral over a density. By performing a multi-dimensional Fourier-transform for each time argument with different frequencies ω_j , we obtain $\tilde{f}(\omega)$. This density correlation function is then scaled with a factor of $\sqrt{a(\omega_j)}$ for every field operator. The overall spectral correlation is now the spectral density of the correlation outside the quantum well. Finally, this correlation is integrated over all frequencies to obtain the correlation of the emitted fields $f_{\text{out}}(0)$. The last step is a Fourier-back transform at $t_j = 0 \forall j$. Therefore, the explicit prefactors for the Fourier-transformation are irrelevant, as the overall transformation has the prefactor $(2\pi)^{-n}$ for n field operators in $f(0)$.

In case of the intensity the steps above are as follows (all integrals are from $-\infty$ to ∞):

$$f(0) = \langle \hat{A}^\dagger \hat{A} \rangle \rightarrow f(t_1, t_2) = \langle \hat{A}^\dagger(t_1) \hat{A}(t_2) \rangle \quad (3.32)$$

$$\tilde{f}(\omega_1, \omega_2) = \int dt_1 \int dt_2 e^{i(\omega_1 t_1 - \omega_2 t_2)} \langle \hat{A}^\dagger(t_1) \hat{A}(t_2) \rangle \quad |\tau := t_2 - t_1 \quad (3.33)$$

$$= \int dt_1 e^{i(\omega_1 - \omega_2)t_1} \int d\tau e^{-i\omega_2 \tau} \langle \hat{A}^\dagger(t_1) \hat{A}(t_1 + \tau) \rangle \quad |t_1 \rightarrow 0 \text{ in } f \quad (3.34)$$

$$= 2\pi \delta(\omega_1 - \omega_2) \int d\tau e^{-i\omega_2 \tau} \langle \hat{A}^\dagger(0) \hat{A}(\tau) \rangle \quad (3.35)$$

$$= (2\pi)^2 \delta(\omega_1 - \omega_2) S_{\text{W}}(\omega_2) \quad (3.36)$$

$$f_{\text{out}}(0) = \frac{(2\pi)^2}{(2\pi)^2} \int d\omega_1 \int d\omega_2 \sqrt{a(\omega_1)} \sqrt{a(\omega_2)} \delta(\omega_1 - \omega_2) S_{\text{W}}(\omega_2) \quad (3.37)$$

$$= \int d\omega_1 a(\omega_1) S_{\text{W}}(\omega_1). \quad (3.38)$$

The last line is identical to the above result Eq. (3.30).

3.3.2. Examples of correlations

Before we start analyzing special correlations for the exciton and quantum-well fields, let us introduce an interpolation for the simulation data. Due to the limited number of spectra, we only have three data sets which would mean only three points for each correlation. In order to illustrate better the evolution of correlations with increasing laser power, we will therefore interpolate the system quantities between the measurements 1 and 3, compare Table 3.1, using quadratic polynomials for Γ , Ω'_R , G' , δ and f . Extrapolation beyond the region of these three points is of limited value. As we interpolate three points with a quadratic polynomial (three degrees of freedom) the simulation data will be exactly obtained in the interpolation, obscuring possible physical effects due to inaccurate data.

Intensity and coherence

We have dealt with the intensity of the quantum-well emission above. Very similar and easy to obtain is the coherence $|\langle \hat{A} \rangle|^2$. As we only consider one operator \hat{A} in the expectation value $\langle \hat{A} \rangle$ and in the steady-state regime, we obtain

$$\langle \hat{A} \rangle_{\text{out}} = \frac{1}{2\pi} \int d\omega \sqrt{a(\omega)} \int dt e^{-i\omega t} \langle \hat{A}(0) \rangle = \sqrt{a(0)} \langle \hat{A}(0) \rangle. \quad (3.39)$$

The frequency zero in the absorption is the laser frequency ω_L , as we work in the frame rotating with ω_L . The coherence itself then follows as

$$|\langle \hat{A} \rangle_{\text{out}}|^2 = a(0) |\langle \hat{A} \rangle|^2, \quad (3.40)$$

which is again identical to our considerations when analyzing the height of the Rayleigh-peak.

In Fig. 3.5 we compare the intensity of the emission and its coherence. For better comparability, we scaled the quantum-well emission by a factor of 3.5, as the absorption is always far below 1. Both the exciton- and the quantum-well coherence decrease with increasing laser power, but the decrease of the latter is enhanced by the decreasing absorption at ω_L . Thus, the observation of a decreased Rayleigh-peak is a combined effect of the decrease of the exciton coherence, and the decrease of the absorption at ω_L . The exciton intensity on the other hand increases almost linearly, with increasing laser power. Hence, the emission for higher excitation becomes more and more incoherent. The quantum-well intensity, however, has a maximum and decreases after a certain excitation. Therefore, the relative coherence $|\langle \hat{A} \rangle|^2 / \langle \hat{A}^\dagger \hat{A} \rangle \leq 1$, is higher for the quantum-well emission, than for the exciton emission. Coherence is necessary for certain nonclassical features, so this result is very interesting for further considerations.

3. Excitons in quantum wells

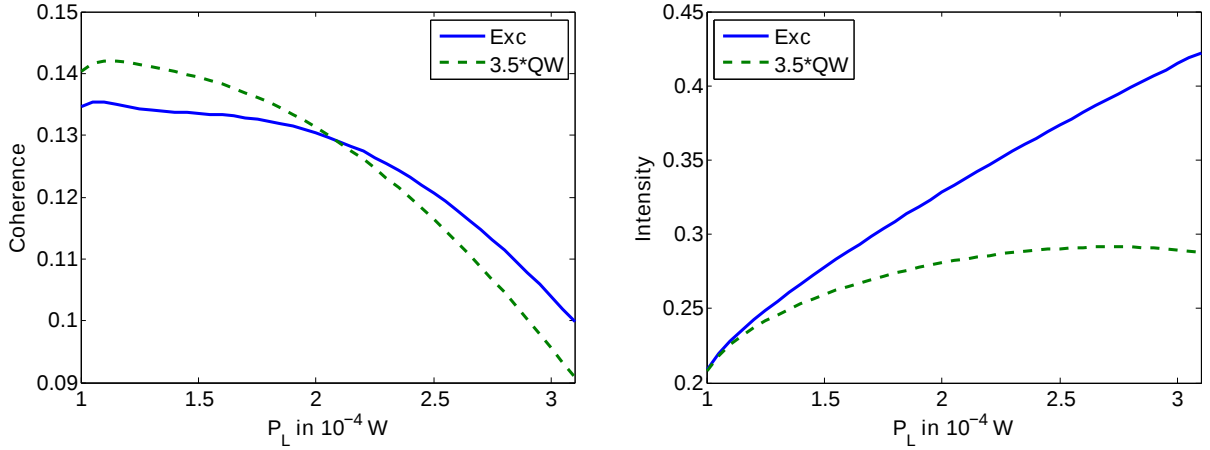


Figure 3.5.: Left: Coherence of the exciton (solid) and quantum well emission (dashed) for increasing P_L . Right: Intensity of the exciton (solid) and quantum well emission (dashed) for increasing P_L .

Squeezing

With the intensity and the coherence given, a possible nonclassical effect to study would be squeezed emission. Squeezing is given, if the normally-ordered field variance falls below zero, see Chap. 2. Scaling the coupling between the source fields and the operator \hat{A} again with χ , the phase-optimized, normally-ordered field variance of the excitons becomes

$$\langle : (\Delta \hat{E}_X)^2 : \rangle / |\chi|^2 = 2(\langle \hat{A}^\dagger \hat{A} \rangle - |\langle \hat{A} \rangle|^2 - |\langle A \rangle|^2 - \langle \hat{A}^2 \rangle). \quad (3.41)$$

The only missing contribution to be analyzed is the second moment $\langle \hat{A}^2 \rangle$. For this term, we have to be more careful when applying the quantum-regression theorem, because we have to keep a normally- and time-ordered structure [29, 142] to avoid free fields becoming relevant to the correlation. Furthermore, the theorem requires a positive time argument. The second moment of the quantum well can be computed as

$$f(t_1, t_2) = \langle \circ \hat{A}(t_1) \hat{A}(t_2) \circ \rangle \quad (3.42)$$

$$\begin{aligned} \tilde{f}(\omega_1, \omega_2) &= \int_{-\infty}^{\infty} dt_2 e^{-i(\omega_1 + \omega_2)t_2} \int_{-\infty}^{\infty} d\tau e^{-i\omega_1\tau} \langle \circ \hat{A}(\tau) \hat{A}(0) \circ \rangle \\ &= 4\pi\delta(\omega_1 + \omega_2) \int_0^{\infty} d\tau \cos(\omega_1\tau) \langle \hat{A}(\tau) \hat{A}(0) \rangle \end{aligned} \quad (3.43)$$

$$\langle \hat{A}^2 \rangle_{\text{out}} = \frac{1}{\pi} \int_{-\infty}^{\infty} d\omega_1 \sqrt{a(\omega_1)a(-\omega_1)} \int_0^{\infty} d\tau \cos(\omega_1\tau) \langle \hat{A}(\tau) \hat{A}(0) \rangle. \quad (3.44)$$

The notation $\circ \dots \circ$ means time- and normal ordering of the correlations, where, additionally to the normal ordering, the time arguments of positive and negative-frequency

parts of the fields are ordered [29]. The absorption frequencies are now correlated symmetrically around ω_L .

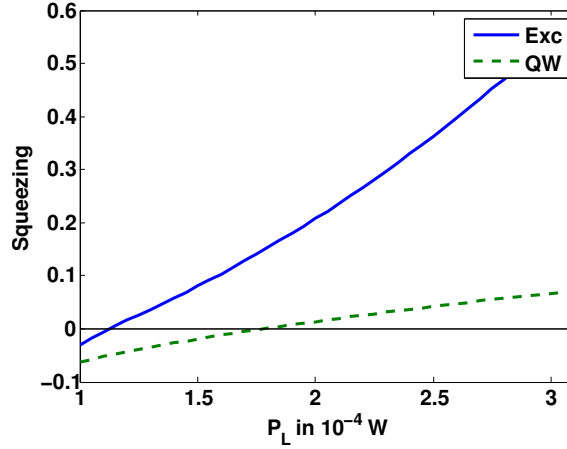


Figure 3.6.: Normally-ordered field variance of the exciton emission for increasing P_L and the corresponding quantum-well emission.

In Fig. 3.6 we compare the squeezing of the exciton emission and quantum-well emission. Squeezing of the exciton emission is limited to very low laser powers, as for higher exciton densities the incoherence of the emission becomes dominant. In the quantum-well emission, on the other hand, the squeezing persists up to a higher laser power. For the whole depicted range of laser powers, the normally-ordered variance stays below the corresponding variance of the exciton fields. This seems surprising at first. Consider again the formula for squeezing, Eq. (3.41), and the relative coherence mentioned above. The intensity is the only positive contribution to the normally-ordered field variance. Due to the different behaviour of the intensity of exciton- and quantum-well emission, the relative coherence of the quantum-well emission surpasses the relative coherence of the exciton emission. Furthermore, the second moment $\langle \hat{A}^2 \rangle_{\text{out}}$ of the quantum-well field is significantly less suppressed than coherence and intensity. This is due to the different structure of the absorption here, compare Eq. (3.44) and Eq. (3.30). Overall, the squeezing of the quantum-well emission is stronger than the squeezing of the exciton emission.

Sub-Poisson light

Another form of nonclassical light is sub-Poisson light, where the variance of the photon number in a given field is smaller than the average photon number, compare Eq. (2.32). The corresponding nonclassicality condition for the moments reads as

$$\langle : \hat{I}^2 : \rangle < \langle \hat{I} \rangle^2 \quad (3.45)$$

$$\langle \hat{A}^{\dagger 2} \hat{A}^2 \rangle < \langle \hat{A}^\dagger \hat{A} \rangle^2. \quad (3.46)$$

3. Excitons in quantum wells

Sub-Poisson light is a sufficient condition for photon-antibunching, compare Chap. 2. The computation of $\langle : \hat{I}^2 : \rangle$ for the quantum-well emission requires an eight-times integral (six, if we take into account the δ -function due to the steady-state scenario), which has not been performed yet. Therefore, we limit the discussion to the potential nonclassical emission, given by the exciton correlations and shown in Fig 3.7.

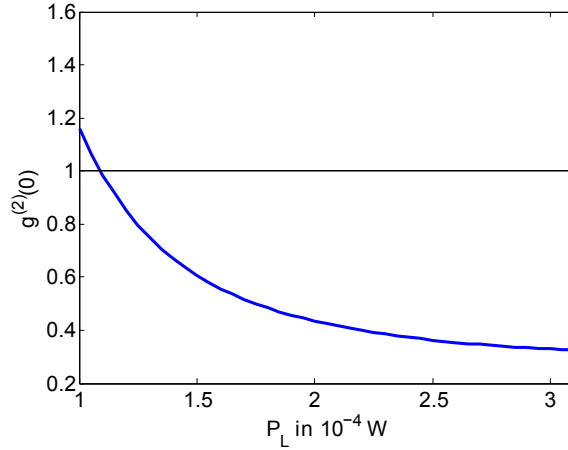


Figure 3.7.: $g^{(2)}(0) = \langle : \hat{I}^2 : \rangle / \langle \hat{I} \rangle^2$ of the exciton fields over increasing P_L . The horizontal line indicates the border between super-Poisson and sub-Poisson light.

We see, that $g^{(2)}(0)$ strictly decreases with increasing laser power P_L . This is due to the strong increase of G' in the exciton emission. For $G' = 0$, the effective master equation Eq. (3.11) describes a bosonic particle driven by a coherent light source and couple to the electromagnetic vacuum by Γ . For this case, independent of the actual values of Γ , Ω'_R , and δ , the steady state of the system would be a coherent state and $g^{(2)}(0) = 1$ for all laser powers. Hence, the nonlinearity G' is responsible for the deviation of the intensity-intensity correlation from 1. As G' increases linearly with the number of excitons N , the influence of the nonlinearity also increases substantially. For very large values of $G' \gg |\delta|, \Gamma$, density matrix elements $\varrho_{m,n} = \langle m | \hat{\varrho} | n \rangle$ with $m \neq n$ and $\max(m, n) > 1$ are suppressed, including the simultaneous excitation of two photons described by \hat{A}^2 . Therefore, the intensity-intensity correlation decreases with increasing G' .

Entanglement

Finally, let us consider the question of entangled-light emission. If squeezed light is sent through a beam splitter, the two spatially separated modes become entangled [105, 106, 107, 108]. Nonclassical correlations in the original field prevail in the two, now spatially separated modes. A consequence of this effect is, that for multimode fields with nonclassical correlations, the different modes are potentially entangled. This is very interesting for our quantum-well scenario, as we not only have a light source with a broad

emission angle, but also a detection system able to collect a large part of that emission capturing the different information [41].

It was analyzed in [I], under what conditions the different spatial modes of a single light source become entangled, using the Shchukin-Vogel criteria for bipartite negative partial transposition (NPT) entanglement [143]. The NPT or Peres-Horodecki criterion [144, 145] argues, that for a bipartite separable (non-entangled) system, after transposing one of the two subsystems, the overall system must still be a quantum state. Thus, the expectation value of $\langle \hat{f}^\dagger \hat{f} \rangle$ in the partially transposed state has to be positive for any function \hat{f} . Violation of this positivity requirement indicates entanglement, that is, it is a sufficient, but not necessary criterion for entanglement. The criterion was later reformulated by Shchukin and Vogel into a hierarchy of bipartite correlation inequalities for the field moments [143]. If one of these inequalities, based on determinants of minors of a matrix of partially transposed moments, becomes negative, entanglement is detected.

In [I] we studied the case where the two subsystems are constituted by two spatial modes of the same light source. In particular the system was comprised of many non-interacting two-level atoms. As our scenario here is different, we will keep the argumentation general and apply it to the quantum-well fields. For only a single source the field operator structure for both modes is the same, while the classical spatial modes are different. In this way, the hierarchy resembles to some extent the hierarchy of moment inequalities showing nonclassicality [139, 143, 146, 88, 140]. In those hierarchies the correlations are normally ordered. As they are field correlations, the normal ordering is also important for our correlations, to neglect free fields. However, the partially transposed correlations in [88] are not necessarily normally ordered, and hence, free fields can be excited. The calculation of the influence of free fields is complicated [29] and should be avoided. Therefore, we may only use minors of correlations, which are already in normal ordering.

Consider the following operator function

$$\hat{f} = c_1 + c_2 \hat{E}_2^{(+)} \hat{E}_1^{(+)} \quad (3.47)$$

from [I] for the fields \hat{E}_1 and \hat{E}_2 . The corresponding minor

$$\begin{aligned} d &= \begin{vmatrix} 1 & \langle \hat{f}^{\text{PT}} \rangle \\ \langle \hat{f}^{\dagger \text{PT}} \rangle & \langle (\hat{f}^\dagger \hat{f})^{\text{PT}} \rangle \end{vmatrix} = \begin{vmatrix} 1 & \langle \hat{E}_2^{(-)*} \hat{E}_1^{(+)} \rangle \\ \langle \hat{E}_1^{(-)} \hat{E}_2^{(+)*} \rangle & \langle \hat{E}_1^{(-)} \hat{E}_2^{(-)} \hat{E}_2^{(+)} \hat{E}_1^{(+)} \rangle \end{vmatrix} \\ &= \langle : \hat{I}_1 \hat{I}_2 : \rangle - |\langle \hat{E}_1^{(-)} \hat{E}_2^{(+)*} \rangle|^2 < 0 \end{aligned} \quad (3.48)$$

fulfills all the above conditions. Excluding the spatial-mode prefactors χ_1, χ_2 , the inequality can be written solely with the single source field to obtain as entanglement condition

$$\langle : \hat{A}^{\dagger 2} \hat{A}^2 : \rangle < \langle \hat{A}^\dagger \hat{A} \rangle^2. \quad (3.49)$$

3. Excitons in quantum wells

This is exactly the condition for sub-Poisson light. As we did not include any specifics about the single light source, this result is a general statement. For any sub-Poisson light source, with multiple spatial modes, these modes are entangled. In our specific case of excitons in a quantum well, we can say, that the exciton emission is entangled for sufficiently large laser power.

4. Filtering of broadband light fields

So far we have investigated the emitted fields of excitons in different structures, and how these fields are influenced by their environments. One important result in all cases was the broad-band nature of the quantum fields. This broad-band emission of excitons is a prerequisite for example for the Mollow sidebands, where the quantum-dot fluorescence is purified, or the discrepancy between the exciton emission in a quantum well and the quantum-well emission itself. The transmission spectrum of a microcavity affects the quantum-dot spectrum detected through the cavity walls in a similar way to the absorption in a quantum well affects the exciton emission [96]. In an experiment with spectrally broad quantum fields, spectral filtering is required to suppress noise from experimental limitations as well as unwanted sideband contributions to the signal field under study. There are two main methods for filtering a phase sensitive quantum signal. Either a spectral filter is used to directly filter the fields before they are detected, or the photoelectric current signal generated by the detector is electronically filtered afterwards. The difference between the two methods is obvious, as the first filters the quantum fields before, and the second the classical current after the measurement. In the first case the filtering generates quantum noise to account for the field commutation relations again, compare [29, 30], in the latter not. The question is, considering our aim of obtaining information about the quantum state of light, which method is preferable to filter the signal. Based on a method to determine general quantum correlations [88], a formalism was developed to obtain filtered correlation functions for both methods of filtering [147], which can be applied to a given incoming signal field [VII]. We will outline the calculation of the filtered correlations in the following chapter.

4.1. Spectrally filtered light

In order to recover spectral information about a given light field, the latter is sent through a frequency sensitive device, a spectral filter, before the actual measurement. In classical physics, the filtered light field is described by the convolution between the unfiltered light and the filter response function. In the quantum-optical theory of photodetection, quantum noise is added to the filtered signal by the filtering procedure. Therefore, the

4. Filtering of broadband light fields

filtered fields must be analyzed on the basis of this additional noise.

The theory of passive optical filters and their influence on correlation properties of filtered quantum light was developed in Refs. [148, 149, 150]. In Ref. [88] a universal measurement scheme has been proposed to measure the quantum correlation functions of light. A simple example of such a setup is shown in Fig. 4.1 on the left. The main idea of the measurement scheme is to obtain the k -th power of the quadrature operator \hat{X}

$$\langle : \hat{X}^k(\varphi) : \rangle = \langle : (\hat{a}e^{i\varphi} + \hat{a}^\dagger e^{-i\varphi})^k : \rangle, \quad (4.1)$$

by combining different measurable normally-ordered intensity correlation functions $\Gamma_\ell^{(k)}$ in a binomial sum. Keep in mind, that for normal ordering free and source fields can be split, with the former becoming irrelevant in a suitable detection scheme. The k -th power of the quadrature operator is related to a quantity $F^{(k)}$, given by

$$F^{(k)} = \sum_{\ell=0}^k (-1)^{k-\ell} \binom{k}{\ell} \Gamma_\ell^{(k)}, \quad (4.2)$$

where $2k$ is the total number of detectors and ℓ is the number of detectors chosen on the left side of the first beam splitter.

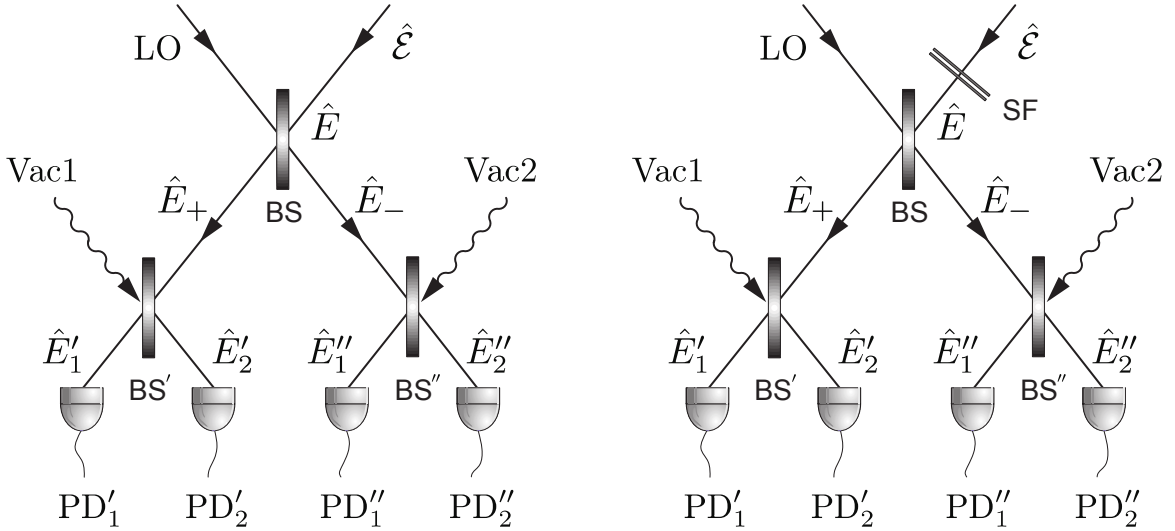


Figure 4.1.: The setup for four-detector correlation measurements without (left) and with (right) spectral filter SF. The filtered signal field \hat{E} is mixed with the local oscillator (LO) by a beam splitter (BS). The resulting field components \hat{E}_\pm pass through two beam splitters BS' and BS'', and are detected by the four photodetectors (PD'_1 – PD''_2).

4.1.1. Spectral filtering of light with a single filter

We will first consider a single filter in front of the first beam splitter and extend the scheme in the next subsection. Consider the measurement scheme as in Fig. 4.1 on the right. With

the superimposed fields after the second line of beam splitters and the different detectors it is possible to measure the second-order intensity correlation functions of the signal field superimposed with the local oscillator (LO) after the first beam splitter, cf. Eq. (4.2) for $k=2$. The setup allows measuring the intensity, and the first and second order moments of the fields, and, consequently, the detection of the squeezing, compare Subsec. 2.2.7. The main difficulty in adding a filter is to preserve the possibility to combine the measured data in a binomial form as in Eq. (4.2).

In Fig. 4.1, $\hat{\mathcal{E}}$ refers to the signal field before passing through the spectral filter. The filtered field is given by \hat{E} , the filter response function by T_f , and the vacuum noise added by the filtering procedure by \hat{E}_n . The filtered field and the LO are superimposed via the beam splitter BS which yields [149]

$$\hat{E}_{\pm}^{(+)}(t) = \frac{e^{i\phi_{\pm}}}{\sqrt{2}} \left[\int dt' T_f(t-t') \hat{\mathcal{E}}^{(+)}(t') + \hat{E}_n^{(+)}(t) \pm i \hat{\mathcal{E}}_{\text{LO}}^{(+)}(t) \right], \quad \hat{E}_{\pm}^{(-)}(t) = \left[\hat{E}_{\pm}^{(+)}(t) \right]^{\dagger}. \quad (4.3)$$

Here, the upper indices (\pm) refer to positive(negative) frequency components of the fields, and the lower indices \pm refer to transmitted(reflected) parts of the incident light after the first beam splitter (cf. Fig. 4.1). The two phases ϕ_{\pm} that correspond to the fields \hat{E}_{\pm} are connected via $\phi_+ - \phi_- = \pi/2$. The noise fields, generated by the filtering procedure, are described by $\hat{E}_n^{(\pm)}(t)$.

After propagation through the other two beam splitters BS' and BS'', the fields at the photodetectors are

$$\hat{E}_j^{(\pm)'} = \frac{e^{\pm i\phi_j}}{\sqrt{2}} \left(\hat{E}_{\pm}^{(\pm)} + \hat{\mathcal{E}}_{\text{vac}1} \right), \quad j = 1, 2, \quad (4.4)$$

$$\hat{E}_j^{(\pm)''} = \frac{e^{\pm i\phi_j}}{\sqrt{2}} \left(\hat{E}_{\pm}^{(\pm)} + \hat{\mathcal{E}}_{\text{vac}2} \right), \quad j = 1, 2, \quad (4.5)$$

where $\phi_{1,2}$ are the phase differences caused by the beam splitters. The terms $\hat{\mathcal{E}}_{\text{vac}1,2}$ describe the vacuum contributions in the unused input ports, not affecting time- and normally ordered correlations [148]. Here symmetric 50:50 beam splitters are assumed. The LO is a strong coherent field with amplitude E_{LO} , described by a classical field amplitude

$$\hat{\mathcal{E}}_{\text{LO}}^{(-)}(t) = E_{\text{LO}} e^{i(\omega_{\text{LO}} t - \phi_{\text{LO}})}, \quad \hat{\mathcal{E}}_{\text{LO}}^{(+)} = \left[\hat{\mathcal{E}}_{\text{LO}}^{(-)} \right]^*. \quad (4.6)$$

The intensity-correlation function to be determined, $\Gamma^{(2)}$, is given by

$$\Gamma^{(2)}(t, t') = \left\langle \circ \hat{E}^{(-)}(t) \hat{E}^{(+)}(t) \hat{E}^{(-)}(t') \hat{E}^{(+)}(t') \circ \right\rangle. \quad (4.7)$$

For that purpose, let us define the following analogs of the photon number operator

4. Filtering of broadband light fields

(cf. [88]):

$$\begin{aligned}\hat{\mathcal{N}}_{\pm} &= \hat{E}_{\pm}^{(-)} \hat{E}_{\pm}^{(+)} \\ &= \frac{1}{2} \left[\int dt'_1 dt'_2 T_f^*(t-t'_1) T_f(t-t'_2) \hat{\mathcal{E}}^{(-)}(t'_1) \hat{\mathcal{E}}^{(+)}(t'_2) \right. \\ &\quad \left. + \hat{E}_n^{(-)} \hat{E}_n^{(+)} + \hat{E}^{(-)} \hat{E}_n^{(+)} + \hat{E}_n^{(-)} \hat{E}^{(+)} + E_{\text{LO}}^2 \pm E_{\text{LO}} (\hat{\mathcal{X}}_{\varphi} + \hat{\mathcal{X}}_{n,\varphi}) \right],\end{aligned}\quad (4.8)$$

where $\varphi = \varphi_{\text{LO}} + \pi/2$ and

$$\hat{\mathcal{X}}_{\varphi} = \hat{E}^{(+)} e^{-i\varphi} + \hat{E}^{(-)} e^{i\varphi}, \quad (4.9)$$

$$\hat{\mathcal{X}}_{n,\varphi} = \hat{E}_n^{(+)} e^{-i\varphi} + \hat{E}_n^{(-)} e^{i\varphi}, \quad (4.10)$$

$$\hat{E}^{(\pm)} = \hat{E}^{(\pm)} e^{\pm i\omega_{\text{LO}} t}, \quad \hat{E}_n^{(\pm)} = \hat{E}_n^{(\pm)} e^{\pm i\omega_{\text{LO}} t}, \quad (4.11)$$

$$\hat{E}^{(+)} = \int dt' T_f(t-t') \hat{\mathcal{E}}^{(+)}(t'). \quad (4.12)$$

Here and in the following the tilde denotes slowly varying field amplitudes. We can now describe the field correlation functions of $\hat{\mathcal{N}}_{\pm}$ similar to the case in [88], cf. Eq. (4.2) with $k = 2$. For $0 \leq \ell \leq 2$ photodetectors on the left side of the setup in Fig. 4.1 and $2 - \ell$ on the right side, we get the correlation functions

$$\Gamma_{\ell}^{(2)} = 2^{-2} \left\langle \circ \hat{\mathcal{N}}_+^{\ell} \hat{\mathcal{N}}_-^{2-\ell} \circ \right\rangle \quad 0 \leq \ell \leq 2. \quad (4.13)$$

Combining them in a binomial sum we obtain the spectral filtered version of the quantity $F^{(2)}$ defined in Eq. (4.2), which reads as

$$F_{\text{spectral}}^{(2)} = 2^{-2} \sum_{\ell=0}^2 (-1)^{2-\ell} \binom{2}{\ell} \left\langle \circ \hat{\mathcal{N}}_+^{\ell} \hat{\mathcal{N}}_-^{2-\ell} \circ \right\rangle = \frac{1}{2^2} \left\langle \circ (\hat{\mathcal{N}}_+ - \hat{\mathcal{N}}_-)^2 \circ \right\rangle = \frac{E_{\text{LO}}^2}{2^2} \left\langle \circ \hat{\mathcal{X}}_{\varphi}^2 \circ \right\rangle. \quad (4.14)$$

The time- and normal ordering made the application of the binomial summation possible, leading to higher order correlations of the spectrally filtered field quadrature $\hat{\mathcal{X}}_{\varphi}$. Using Eq. (4.9), we may write Eq. (4.14) explicitly as

$$\begin{aligned}F_{\text{spectral}}^{(2)} &= \frac{E_{\text{LO}}^2}{2^2} \int dt'_1 \int dt'_2 \times \\ &\quad \left\langle \circ \prod_{j=1}^2 \left[T_f(t-t'_j) \hat{\mathcal{E}}^{(+)}(t'_j) e^{i(\omega_{\text{LO}} t - \varphi)} + T_f^*(t-t'_j) \hat{\mathcal{E}}^{(-)}(t'_j) e^{-i(\omega_{\text{LO}} t - \varphi)} \right] \circ \right\rangle.\end{aligned}\quad (4.15)$$

The different moments of field operators up to order of k can be constructed from the Fourier-transform of Eq. (4.14) with respect to the phase φ according to

$$\int_0^{2\pi} d\varphi F_{\text{spectral}}^{(n+m)} e^{-i(n-m)\varphi} \propto \left\langle \circ \hat{E}^{(-)n} \hat{E}^{(+m)} \circ \right\rangle, \quad (4.16)$$

with m and n being integers. Specifically for our case $k = 2$, we get the following three field correlations functions

$$\int_0^{2\pi} d\varphi F_{\text{spectral}}^{(2)} e^{-i2\varphi} = \frac{\pi}{2} E_{\text{LO}}^2 \left\langle \circ \hat{E}^{(-)2} \circ \right\rangle, \quad (4.17)$$

$$\int_0^{2\pi} d\varphi F_{\text{spectral}}^{(2)} = \pi E_{\text{LO}}^2 \left\langle \circ \hat{E}^{(-)} \hat{E}^{(+)} \circ \right\rangle, \quad (4.18)$$

$$\int_0^{2\pi} d\varphi F_{\text{spectral}}^{(2)} e^{i2\varphi} = \frac{\pi}{2} E_{\text{LO}}^2 \left\langle \circ \hat{E}^{(+2)} \circ \right\rangle. \quad (4.19)$$

These moments, when expressed in terms of the signal fields, are for the case of Eq. (4.19) of the form

$$\left\langle \circ \hat{E}^{(+2)} \circ \right\rangle = \int dt'_1 \int dt'_2 T_f(t-t'_1) T_f(t-t'_2) \left\langle \circ \hat{\mathcal{E}}^{(+)}(t'_1) \hat{\mathcal{E}}^{(+)}(t'_2) \circ \right\rangle e^{2i\omega_{\text{LO}} t}. \quad (4.20)$$

We obtained the connection between the incident light fields, the filter functions and the fields at the detector in terms of the corresponding correlation functions.

4.1.2. Spectral filtering of light with two filters

In order to resolve the squeezing spectrum, we need to calculate the correlations of optical fields with different frequencies. Therefore we also need two different spectral filters instead of one. Again the configuration of the filters is required to allow the binomial summation of the different correlations. The arrangement of the setup is given in Fig. 4.2.

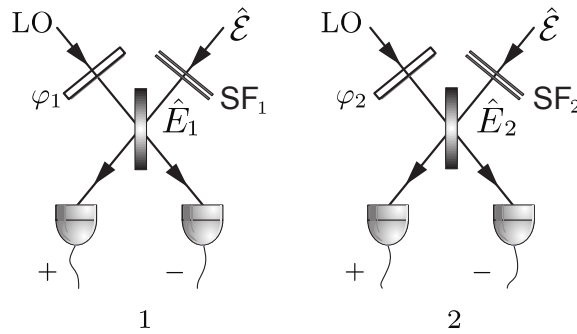


Figure 4.2.: The four-detector measurement scheme for correlations of fields with different frequencies and phases. The signal field $\hat{\mathcal{E}}$ in the j -th arm of the setup ($j = 1, 2$) passes through the corresponding spectral filter SF_j , before being mixed with the phase-controlled LO.

The signal field $\hat{\mathcal{E}}$ is split in two parts, each of which entering a different homodyning setup. At the spectral filters SF_1 and SF_2 the signal field $\hat{\mathcal{E}}$ transforms into the fields \hat{E}_1 and \hat{E}_2 . Each field is mixed with a LO of different relative phase φ_j and the resultant four fields impinge on the detectors. These fields read as

$$\hat{E}_{j,\pm}^{(+)} = \frac{e^{i\phi_{\pm}}}{\sqrt{2}} \left(\hat{E}_j^{(+)} \pm i\hat{\mathcal{E}}_{j,\text{LO}}^{(+)} \right), \quad (4.21)$$

4. Filtering of broadband light fields

where each detector is numbered by the index $\{j, \pm\}$, $j = 1, 2$. Similar to Eq. (4.3), the filtered fields \hat{E}_j relate to the unfiltered fields by

$$\hat{E}_j^{(+)} = \int dt'_j T_{f_j}(t - t'_j) \hat{\mathcal{E}}^{(+)}(t'_j) + E_{j,n}^{(+)}, \quad (4.22)$$

with the response functions $T_{f_j}(t - t'_j)$ of the j -th filter device. The number operators Eq. (4.8) read as

$$\begin{aligned} \hat{\mathcal{N}}_{j,\pm} &= \hat{E}_{j,\pm}^{(-)} \hat{E}_{j,\pm}^{(+)} \\ &= \frac{1}{2} \left(\hat{E}_j^{(-)} \hat{E}_j^{(+)} + \hat{E}_{j,n}^{(-)} \hat{E}_{j,n}^{(+)} + \hat{E}_j^{(-)} \hat{E}_{j,n}^{(+)} + \hat{E}_{j,n}^{(-)} \hat{E}_j^{(+)} + E_{j,LO}^2 \pm E_{j,LO} (\hat{\mathcal{X}}_{j,\varphi} + \hat{\mathcal{X}}_{j,n,\varphi}) \right), \end{aligned} \quad (4.23)$$

with noise operators and quadratures analog to the single-filter case in Eqs.(4.9)-(4.12). Note that $\varphi_j = \varphi_{j,LO} + \pi/2$.

As we now correlate two homodyne setups, we have two free parameters ℓ and j with $0 \leq \ell, j \leq 1$ for the two setups. The normally-ordered correlation functions of the photodetectors are

$$\Gamma_{\ell,j}^{(1,1)} = \left\langle \circ \hat{\mathcal{N}}_{1,+}^{\ell} \hat{\mathcal{N}}_{1,-}^{1-\ell} \hat{\mathcal{N}}_{2,+}^j \hat{\mathcal{N}}_{2,-}^{1-j} \circ \right\rangle. \quad (4.24)$$

Here, the upper indices $(1, 1)$ of the correlation function indicate the depth levels of the measurement in each homodyning setup. Since in our case both indices are equal to one we can use this setup to measure second order correlation functions of two frequencies.

Applying the formalism from Eq. (4.2) to Eq. (4.24), we can define the spectral function

$$F_{\text{spectral}}^{(1,1)} = \sum_{\ell=0}^1 \sum_{j=0}^1 (-1)^{1-\ell} (-1)^{1-j} \Gamma_{\ell,j}^{(1,1)}. \quad (4.25)$$

This function reads in extended form as

$$\begin{aligned} F_{\text{spectral}}^{(1,1)} &= \left\langle \circ \left(\hat{\mathcal{N}}_{1,+} - \hat{\mathcal{N}}_{1,-} \right) \left(\hat{\mathcal{N}}_{2,+} - \hat{\mathcal{N}}_{2,-} \right) \circ \right\rangle = E_{LO}^2 \left\langle \circ \hat{\mathcal{X}}_{1,\varphi_1} \hat{\mathcal{X}}_{2,\varphi_2} \circ \right\rangle \\ &= E_{LO}^2 \int dt'_1 \int dt'_2 \\ &\quad \times \left\langle \circ \prod_{j=1}^2 \left[T_{f_j}(t - t'_j) \hat{\mathcal{E}}^{(+)}(t'_j) e^{i(\omega_{j,LO} t - \varphi_j)} + T_{f_j}^*(t - t'_j) \hat{\mathcal{E}}^{(-)}(t'_j) e^{-i(\omega_{j,LO} t - \varphi_j)} \right] \circ \right\rangle. \end{aligned} \quad (4.26)$$

Finally, performing a two-dimensional Fourier-transform, we can again select specific moments of the fields such as

$$\begin{aligned} \left\langle \circ \hat{E}_1^{(\pm)} \hat{E}_2^{(\pm)} \circ \right\rangle &= \int dt_1 \int dt_2 \times \\ &\quad T_{f_1}^{(\pm)}(t-t_1) T_{f_2}^{(\pm)}(t-t_2) e^{i(\pm\omega_{1,LO} \pm \omega_{2,LO})t} \left\langle \circ \hat{\mathcal{E}}^{(\pm)}(t_1) \hat{\mathcal{E}}^{(\pm)}(t_2) \circ \right\rangle, \end{aligned} \quad (4.27)$$

where $T_f^+(t) = T_f(t)$ and $T_f^- = [T_f^+]^*$. This formula is the two-filter correspondence to Eq. (4.20).

4.2. Photocurrent filtering

Filtering the photoelectric current generated from the light field incident on a photodetector is more common in experiments than spectral filtering of light. It can be easier controlled than optical filter devices and the light field itself is not modified by the filter. Moreover, from a quantum-optical point, the filtering is classical, as the current is the observable in this scenario. However, as the incident light field is now still broadband at the detector, the detector response becomes relevant. Therefore an additional filtering occurs due to the detector, which influences the measured correlation functions.

4.2.1. Photocurrent filtering with one filter frequency

As was done in the case of spectral filtering, we want to distinguish a single-filter four-detector setup and two two-detector setups with individual filter response functions. Consider the four-detector setup shown in Fig. 4.3. The unfiltered light fields are mixed in the beam splitters and enter the detectors before four identical electronic filters analyze the photocurrents.

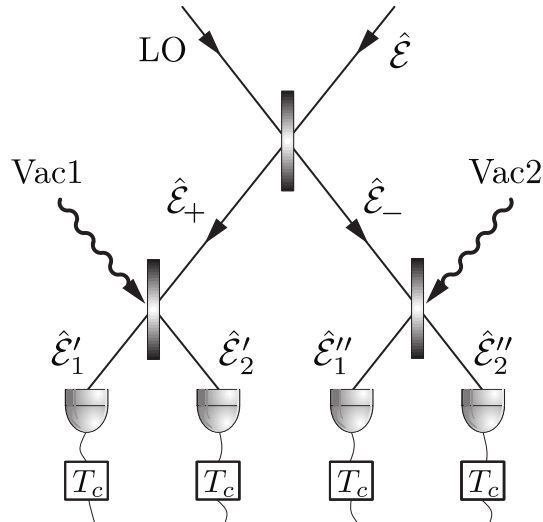


Figure 4.3.: Four-detector setup with current filtering. The outcomes of the photodetection measurement are filtered by the current filters T_c .

The operation of photodetectors is described in [29], based on quantum and classical statistics. We define the operator $\hat{\Gamma}$

$$\hat{\Gamma}(t, \Delta t) = N \int_t^{t+\Delta t} d\tau \int_t^{t+\Delta t} d\tau' S(\tau-\tau') \hat{\mathcal{E}}^{(-)}(\tau) \hat{\mathcal{E}}^{(+)}(\tau'), \quad (4.28)$$

which corresponds to the intensity measured by a single detector. Here we assume a small-volume detector with N identical atoms that absorb the incoming photons. The

4. Filtering of broadband light fields

light irradiates the detector in the time interval $[t, t + \Delta t]$. $S(\tau)$ is the mentioned detector response function.

With these $\hat{\Gamma}$ -operators, we can now describe the correlation between the number n of generated photoelectrons, or 'clicks' of the detector setup. Following [29], we obtain for the correlation of two detectors $j = 1, 2$, starting from different times t_j , measuring over the same interval Δt ,

$$\overline{n(t_1, \Delta t)n(t_2, \Delta t)} = \sum_{m_1, m_2=0}^{\infty} m_1 m_2 P_{m_1, m_2}(t_1, \Delta t, t_2, \Delta t) = \left\langle \circ \hat{\Gamma}^{(1)}(t_1, \Delta t) \hat{\Gamma}^{(2)}(t_2, \Delta t) \circ \right\rangle. \quad (4.29)$$

Here, $n(t_j, \Delta t)$ is the number of 'clicks' in the detector j and $P_{m_1, m_2}(t_1, \Delta t, t_2, \Delta t)$ is the joint probability of emission of m_1 photoelectrons within the time interval $[t_1, t_1 + \Delta t]$ in detector 1 and m_2 photoelectrons within $[t_2, t_2 + \Delta t]$ in detector 2. We assume that both time intervals do not overlap, as otherwise, shot-noise terms have to be included [29].

For $n(t, \Delta t)$ generated photoelectrons sent through a classical amplifier the outgoing photocurrent can be given by $i(t) = g e n(t, \Delta t) / \Delta t$ with g being the gain factor, which is assumed to be constant and e the elementary charge. Each current is now filtered with a filter response function $T_c(t)$,

$$i_f(t) = \int dt' T_c(t-t') i(t'), \quad (4.30)$$

so that the correlation function of two filtered currents becomes

$$\overline{i_{1f}(t_1) i_{2f}(t_2)} = \left(\frac{g e}{\Delta t} \right)^2 \int dt'_1 T_c(t_1 - t'_1) \int dt'_2 T_c(t_2 - t'_2) \left\langle \circ \hat{\Gamma}^{(1)}(t'_1, \Delta t) \hat{\Gamma}^{(2)}(t'_2, \Delta t) \circ \right\rangle. \quad (4.31)$$

For the special scheme in Fig. 4.3 the appropriate $\hat{\Gamma}$ -operators describing each detector read as

$$\hat{\Gamma}'_j(t, \Delta t) = N \int_t^{t+\Delta t} d\tau \int_t^{t+\Delta t} d\tau' S(\tau - \tau') \hat{\mathcal{E}}_j^{(-)'}(\tau) \hat{\mathcal{E}}_j^{(+)' }(\tau'), \quad (4.32)$$

$$\hat{\Gamma}''_j(t, \Delta t) = N \int_t^{t+\Delta t} d\tau \int_t^{t+\Delta t} d\tau' S(\tau - \tau') \hat{\mathcal{E}}_j^{(-)''}(\tau) \hat{\mathcal{E}}_j^{(+)' }(\tau'). \quad (4.33)$$

Here again, one and two primes denote left and right arm of the homodyne setup, respectively. The fields entering the detectors are linear combinations of the fields after the first beam splitter $\hat{\mathcal{E}}_-$ and $\hat{\mathcal{E}}_+$ and vacuum contributions. Taking into account, that each detector only gets half of the intensity of the latter fields due to the second level of beam splitters, we can define the correlation functions of the fields after the first beam splitter,

$$\hat{\Gamma}_{\pm}(t'_j, \Delta t) = \frac{N}{2} \int_{t'_j}^{t'_j + \Delta t} d\tau \int_{t'_j}^{t'_j + \Delta t} d\tau' S(\tau - \tau') \hat{\mathcal{E}}_{\pm}^{(-)}(\tau) \hat{\mathcal{E}}_{\pm}^{(+)}(\tau'). \quad (4.34)$$

It follows, after some algebra, that $\langle \circ \hat{\Gamma}_+^\ell \hat{\Gamma}_-^{2-\ell} \circ \rangle = \langle \circ \hat{\Gamma}_j^{\ell'} \hat{\Gamma}_k^{2-\ell'-\ell} \circ \rangle$, with $j, k = 1, 2$ and $\ell = 0, 1, 2$, and consequently for the (equal time) current-correlation functions

$$\overline{i_+(t)^\ell i_-(t)^{2-\ell}} = \left(\frac{ge}{\Delta t}\right)^2 \int dt'_1 T_c(t-t'_1) \int dt'_2 T_c(t-t'_2) \left\langle \circ \hat{\Gamma}_+^\ell \hat{\Gamma}_-^{2-\ell} \circ \right\rangle. \quad (4.35)$$

The subscript \pm again refers to the side of the first beam splitter, where the field was detected.

Now we can construct the correlation function $F_{\text{current}}^{(k)}$ [cf. Eq. (4.2)]

$$F_{\text{current}}^{(k)} = \sum_{\ell=0}^k (-1)^{k-\ell} \binom{k}{\ell} \overline{n_+^\ell n_-^{k-\ell}}, \quad (4.36)$$

with $n_\pm = (\Delta t/ge)i_\pm$. For $k = 2$, as in Fig. 4.3 this expression reduces to

$$\begin{aligned} F_{\text{current}}^{(2)} &= \overline{n_-^2} - \overline{2n_+n_-} + \overline{n_+^2} \\ &= \int dt_1 T_c(t-t_1) \int dt_2 T_c(t-t_2) \left\langle \circ \prod_{i=1}^2 \left(\hat{\Gamma}_+(t_j) - \hat{\Gamma}_-(t_j) \right) \circ \right\rangle. \end{aligned} \quad (4.37)$$

Applying Eq. (4.6) and the form of the fields after the first beam splitter in Fig. 4.3, the difference of two correlation functions occurring in Eq. (4.37) can be shown to be equal to

$$\hat{\Gamma}_+(t_j) - \hat{\Gamma}_-(t_j) = \frac{NE_{\text{LO}}}{2} \int_{t_j}^{t_j+\Delta t} d\tau \int_{t_j}^{t_j+\Delta t} d\tau' S(\tau-\tau') \left[\hat{\mathcal{E}}^{(-)}(\tau) e^{-i\omega_{\text{LO}}\tau'+i\varphi} + \hat{\mathcal{E}}^{(+)}(\tau') e^{i\omega_{\text{LO}}\tau-i\varphi} \right], \quad (4.38)$$

with $\varphi = \varphi_{\text{LO}} + \pi/2$. The current-correlation function $F_{\text{current}}^{(2)}$ reads as

$$\begin{aligned} F_{\text{current}}^{(2)} &= \frac{N^2 E_{\text{LO}}^2}{2^2} \int dt_1 T_c(t-t_1) \int dt_2 T_c(t-t_2) \\ &\left\langle \circ \prod_{j=1}^2 \int_{t_j}^{t_j+\Delta t} d\tau_j \int_{t_j}^{t_j+\Delta t} d\tau'_j S(\tau_j-\tau'_j) \left[\hat{\mathcal{E}}^{(-)}(\tau_j) e^{-i\omega_{\text{LO}}\tau'_j+i\varphi} + \hat{\mathcal{E}}^{(+)}(\tau'_j) e^{i\omega_{\text{LO}}\tau_j-i\varphi} \right] \circ \right\rangle. \end{aligned} \quad (4.39)$$

Comparing the result with Eq. (4.15) for the radiation filtering case, we may identify the essential difference between radiation and current filtering. For spectral filtering, the filter process is performed before the quantum mechanical averaging procedure; for the current filtering after the averaging. On the other hand, an additional filtering from the detector response has to be considered, which is relevant for broad-band light fields.

4.2.2. Filtered current using two filter frequencies

Finally, let us extend the current filtering scheme to the case of two current-filters tuned on different frequencies. This is, analog to the case of spectral filtering, necessary to

4. Filtering of broadband light fields

detect the squeezing spectrum of the incident light field. Therefore, we adopt the scheme depicted in Fig. 4.4.

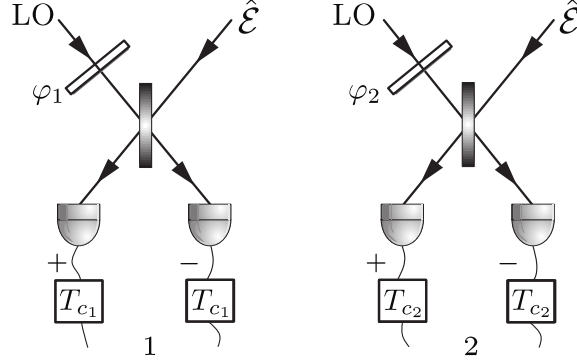


Figure 4.4.: Modified scheme of Fig. 4.2 with current filtering responses T_{c_j} for the j -th arm of the setup.

The current-correlation function $F_{\text{current}}^{(1,1)}$ that can be constructed from this setup, has the form

$$\begin{aligned}
 F_{\text{current}}^{(1,1)} &= \sum_{\ell=0}^1 \sum_{j=0}^1 (-1)^{1-\ell} (-1)^{1-j} \overline{n_{1,+}^{\ell} n_{1,-}^{1-\ell} n_{2,+}^j n_{2,-}^{1-j}} \\
 &= \overline{n_{1,-} n_{2,-} - n_{1,+} n_{2,-} - n_{1,-} n_{2,+} + n_{1,+} n_{2,+}} \\
 &= \int dt_1 T_{c_1}(t-t_1) \int dt_2 T_{c_2}(t-t_2) \left\langle \circ \hat{\Gamma}_{1,-} \hat{\Gamma}_{2,-} - \hat{\Gamma}_{1,+} \hat{\Gamma}_{2,-} - \hat{\Gamma}_{1,-} \hat{\Gamma}_{2,+} + \hat{\Gamma}_{1,+} \hat{\Gamma}_{2,+} \circ \right\rangle.
 \end{aligned} \tag{4.40}$$

where the indices 1, 2 correspond to the different homodyne setups. The sum on the right hand side can be simplified to

$$\begin{aligned}
 &\prod_{j=1}^2 \left[\hat{\Gamma}_{j,+}(t_j) - \hat{\Gamma}_{j,-}(t_j) \right] = \\
 &N E_{\text{LO}} \prod_{j=1}^2 \int_{t_j}^{t_j+\Delta t} d\tau \int_{t_j}^{t_j+\Delta t} d\tau' S(\tau-\tau') \left[\hat{\mathcal{E}}^{(-)}(\tau) e^{-i(\omega_j, \text{LO}\tau' - \varphi_j)} + \hat{\mathcal{E}}^{(+)}(\tau') e^{i(\omega_j, \text{LO}\tau - \varphi_j)} \right],
 \end{aligned} \tag{4.41}$$

where $\varphi_j = \varphi_{j,\text{LO}} + \pi/2$. This yields for $F_{\text{current}}^{(1,1)}$

$$\begin{aligned}
 F_{\text{current}}^{(1,1)} &= N^2 E_{\text{LO}}^2 \int dt_1 T_{c_1}(t-t_1) \int dt_2 T_{c_2}(t-t_2) \\
 &\left\langle \circ \prod_{j=1}^2 \int_{t_j}^{t_j+\Delta t} d\tau_j \int_{t_j}^{t_j+\Delta t} d\tau'_j S(\tau_j - \tau'_j) \left[\hat{\mathcal{E}}^{(-)}(\tau_j) e^{-i(\omega_j, \text{LO}\tau'_j - \varphi_j)} + \hat{\mathcal{E}}^{(+)}(\tau'_j) e^{i(\omega_j, \text{LO}\tau_j - \varphi_j)} \right] \circ \right\rangle.
 \end{aligned} \tag{4.42}$$

Comparing with the corresponding case of spectral filtering, Eq. (4.26), we can again see the different positions of the filtering procedure for the two methods of filtering.

In general both, spectral and current filtering, can be applied simultaneously within one experimental setup. Then, the theoretical description of each method is combined in a linear, but lengthy way. An interesting topic for further research is, whether one method is preferable over the other for certain experiments and their aims [VII].

5. Conclusions

5.1. Summary

In this thesis, we studied the quantum-optical properties of light fields emitted from different semiconductor micro- and nanostructures. Excitons form the dipoles, which couple to the electromagnetic fields. Based on models for the excitons in different structures, and including several influences due to the medium, we could derive the theoretical description of the quantum light fields from the excitons.

In a quantum dot, only a single exciton gets excited, which behaves similar to an atom. For most optical processes only a single dipole between two energy levels is relevant for considerations, yielding a two-level structure for the exciton. However, the exciton is also subject to different dissipative channels. Inside a microcavity, a quantum dot may couple to different cavity modes, by exciting or relaxing an additional phonon. The correct resonance conditions of such a two-mode scenario become clear in the dressed state picture. These phonon-assisted Rabi transitions alter the dynamics of the emitted fields substantially and may lead to wrong interpretations of observations. We considered both, the rates of photon emission through the different decay channels, as well as the time-integrated spontaneous-emission spectrum to visualize the effects.

A microcavity of intermediate coupling strength can purify the quantum state of a single-photon emitter, which is coherently driven. This is due to the fact that the cavity acts as a second decay channel. It diminishes the excitation of the single-photon emitter and, simultaneously, increases its coherence. This yields an optimized squeezing of the quantum-dot fluorescence. We analyzed the robustness of the optimized squeezing against dissipative channels expected in quantum-dot-microcavity systems. The influence of non-radiative dephasing could be substantially limited. Incoherent pumping of the quantum dot is overcome by the purification procedure. However, incoherent pumping of the cavity mode is not suppressed by the purification, as it acts on the cavity mode and not the quantum dot. We proposed a method to detect the squeezing applying a balanced homodyne correlation setup.

In quantum wells multiple excitons in a low density regime act like a single bosonic excitation with a Kerr-nonlinear coupling. In case of a driven system of many excitons,

5. Conclusions

the nonlinearity and the laser-coupling strength increase with the number of excitons. The excitons are created by absorbing the incoming laser light. Hence, the emission spectrum also scales with the absorption spectrum. This allowed us to interpret the different fluorescence spectra of a given quantum well. We found, that the light is superfluorescent, based on a collective strong dipole of the excitons. With the knowledge of the fields generated in the quantum well, we are able to compute the different field correlations and study quantum properties. For low intensities, the quantum-well emission is squeezed. For higher intensities, the exciton emission is sub-Poisson. The different spatial modes of the fluorescent light are entangled, if the light fields are sub-Poisson.

Due to the spectral broadness of the emitted light fields, a filtering procedure has to be applied, before the fields can be analyzed. This can either be done by spectrally filtering the light, before it is detected, or by filtering the electronic current generated in a photodetector. We analyzed the basic principles for each filtering method and obtained general relations between the incoming light fields, the applied filters, and the measured correlations. In case of spectral filtering, quantum noise is generated, as the filtering occurs before the measurement. These noises would be avoided by filtering the photoelectric current. However, for broadband fields, the response of the detector becomes relevant and acts as an additional filter.

5.2. Outlook

The results of this thesis can be seen as promising for future applications of semiconductor micro- and nanostructures in terms of nonclassical light. We have considered different dynamical situations of excitons, included environmental influences (dissipation, dephasing, phonons, response of the medium) to obtain overall quantum fields, whose nonclassical properties could be studied. These nonclassical phenomena can be used for practical applications. Furthermore, we could describe the detected fields after a filtering procedure was included. A general limitation of the discussed research is the accuracy of the models at each step. The quantum-optical description of excitons is so far limited to either of two approximative situations. Describing dissipative processes within the Markov-approximation does not consider memory effects of the medium. The susceptibility of the semiconductor medium may be accurately calculated with many-body theory. In fact, according to our description, the response of the medium should also yield the exciton parameters in a self-consistent way. Besides these topics for further research, some specific remarks about each part of the thesis is appropriate.

The methods discussed in Sec. 2.1 are limited to a single phonon-excitation, modeled by a vibronic transition. This already indicated the possible manipulation of the spon-

taneous emission of a quantum dot. A more realistic treatment requires a broad exciton spectrum, which should yield a broad resonance on both the bare quantum dot and/or cavity resonances as well as the dressed state resonances. Furthermore, the dissipative processes mentioned need to be included, resulting in a plethora of free parameters to be determined from experiment. Another aspect that has to be considered is the cavity resonance. As stated, the quantum-dot emission is often detected through the cavity walls. Therefore, the light field is convoluted with the cavity transmission function. By shifting the quantum-dot resonance through the cavity resonance an increase will occur, which is independent of the actual exciton dynamics and dissipation. Note that the Purcell-effect always yields a decrease of the emission amplitude, in contrast to the transmission resonance.

When all the effects discussed above are considered, it should be possible to analyze a quantum dot inside a microcavity well enough to actually study its quantum properties. The optimized squeezing is an important example to be considered. Again, if the field is detected through the cavity walls, the effects of the cavity resonance need to be incorporated into the discussion. A totally different, but interesting question is the quantum properties of the cavity field itself. For a purified quantum state we found the intracavity field to be very incoherent. However, for other parameters, the cavity emission is also squeezed, independent of the quantum-dot fluorescence. Furthermore, as the Fock space of the cavity field is not limited as for the quantum dot, higher-order nonclassical features can be studied. The fluorescence is also a possible light field to set up the balanced correlation homodyne experiment.

With the prediction of squeezed quantum-well fluorescence, an experiment measuring the field variance is the obvious next step in experiments. Besides further analysis of quantum properties, other dissipative effects have so far been omitted from the consideration. Similar to the discussion of the sensitivity of the optimized quantum-dot-fluorescence squeezing, dissipative effects can then be analyzed with respect to their influence on the quantum properties.

For all the given structures, the filtered fields have to be determined, to obtain the actual measurement outcomes. In that case, we would have a full theoretical description, starting from the emitting dipoles, including their environmental influences until we have the light fields exiting this structure, and including the spectral limitations of the measurement process. This overall transformation from source-field operators to the eventually observed correlations would be the basis for actual discussions about applications of semiconductor micro- and nanostructures.

Appendix

A. Publications and Conference Contributions

A.1. List of own Publications

Published Articles

- [I] P. Grünwald and W. Vogel
Entanglement in atomic resonance fluorescence
Phys. Rev. Lett. **104**, 233602 (2010);
see also P. Grünwald and W. Vogel
Phys. Rev. Lett. **106**, 119903(E) (2011).

- [II] P. Grünwald, S. K. Singh, and W. Vogel
Raman-assisted Rabi resonances in two-mode cavity QED
Phys. Rev. A **83**, 063806 (2011).

- [III] P. Grünwald and W. Vogel
Optimal Squeezing in Resonance Fluorescence via Atomic-State Purification
Phys. Rev. Lett. **109**, 013601 (2012).

- [IV] P. Grünwald and W. Vogel
Optimal Squeezing in the Resonance Fluorescence of Single Photon Emitters
Phys. Rev. A **88**, 023837 (2013).

- [V] P. Grünwald, G. K. G. Burau, H. Stolz, and W. Vogel
Superfluorescence spectra of excitons in quantum wells
Phys. Rev. B **88**, 195308 (2013).

Articles in preparation

- [VI] P. Grünwald and W. Vogel
Nonclassical Light in Quantum-well Fluorescence

- [VII] J. Häggblad, D. Vasylyev, P. Grünwald, and W. Vogel
Filtering and Measurement of Broadband Nonclassical Light Fields

A.2. Conference Contributions

- [a] 17th Central European Workshop on Quantum Optics (CEWQO)
St. Andrews, United Kingdom, June 06 - 11, 2010
Contributed talk: P. Grünwald and W. Vogel
Entanglement in atomic resonance fluorescence.

- [b] 18th Central European Workshop on Quantum Optics (CEWQO)
Madrid, Spain, May 30 - June 03, 2011
Contributed talk: P. Grünwald, S. K. Singh, and W. Vogel
Raman-Assisted Rabi Resonances in Two-Mode Cavities.

- [c] International Conference on Correlation Effects in Radiation Fields (CERF2011)
Rostock, Germany, September 12 - 16, 2011
Poster: P. Grünwald, S. Singh, and W. Vogel
Raman-assisted Rabi resonances in two-mode cavities.

- [d] 19th Central European Workshop on Quantum Optics (CEWQO)
Sinaia, Romania, July 02 - 06, 2012
Contributed talk: P. Grünwald and W. Vogel
Atomic state purification and optimal squeezing in optical cavities.

- [e] 13th International Conference on Squeezed States and Uncertainty Relations
(ICSSUR)
Nuremberg, Germany, June 24 - 28, 2013
Contributed Talk: P. Grünwald and W. Vogel
Optimized Fluorescence Squeezing from Single Photon Emitters;
Poster: P. Grünwald, G. K. G. Burau, H. Stolz, and W. Vogel
Resonance Fluorescence Spectra from Semiconductor Quantum Wells.

- [f] 12th International Conference on Optics of Excitons in Confined Systems (OECS)
Rome, Italy, September 09 - 13, 2013
Poster: P. Grünwald, G. K. G. Burau, H. Stolz, and W. Vogel
Resonance Fluorescence Spectra from Semiconductor Quantum Wells.

Bibliography

- [1] E. C. G. Sudarshan, Phys. Rev. Lett. **10**, 277 (1963).
- [2] R. J. Glauber, Phys. Rev. **131**, 2766 (1963).
- [3] H. J. Carmichael and D. F. Walls, J. Phys. B **9**, L43 (1976).
- [4] H. J. Kimble and L. Mandel, Phys. Rev. A **13**, 2123 (1976).
- [5] H. J. Kimble, M. Dagenais, and L. Mandel, Phys. Rev. Lett. **39**, 691 (1977).
- [6] B. R. Mollow, Phys. Rev. **188**, 1969 (1969).
- [7] F. Schuda, C. R. Stroud, and M. Hercher, J. Phys. B **1**, L198 (1974).
- [8] R. J. Thompson, G. Rempe and H. J. Kimble, Phys. Rev. Lett. **68**, 1132 (1992).
- [9] Geo cooperation (corresponding author: R. Schnabel), Nature Physics **7**, 962 (2011).
- [10] R. Horodecki, P. Horodecki, M. Horodecki, and K. Horodecki, Rev. Mod. Phys. **81**, 865 (2009).
- [11] O. Gühne and O. Toth, Phys. Rep. **474**, 1 (2009).
- [12] M. Mehmet, S. Ast, T. Eberle, S. Steinlechner, H. Vahlbruch, and R. Schnabel, Opt. Exp. **19**, 25763 (2011).
- [13] F. Diedrich and H. Walther, Phys. Rev. Lett. **58**, 203 (1987).
- [14] M. Schubert, I. Siemers, R. Blatt, W. Neuhauser, and P. E. Toschek, Phys. Rev. Lett. **68**, 3016 (1992).
- [15] Z. H. Lu, S. Bali, and J. E. Thomas, Phys. Rev. Lett. **81**, 3635 (1998).
- [16] M. G. Raizen, L. A. Orozco, Min Xiao, T. L. Boyd, and H. J. Kimble, Phys. Rev. Lett. **59**, 198 (1987).
- [17] D. F. Walls and P. Zoller, Phys. Rev. Lett. **47**, 709 (1981).

Bibliography

- [18] K. Sebald, P. Michler, T. Passow, D. Hommel, G. Bacher, and A. Forchel, *Appl. Phys. Lett.* **81**, 2920 (2002).
- [19] P. Michler, *Single Semiconductor Quantum Dots*, (Springer, Berlin, 2009).
- [20] A. Muller, E. B. Flagg, P. Bianucci, X. Y. Wang, D. G. Deppe, W. Ma, J. Zhang, G. J. Salamo, M. Xiao, and C. K. Shih, *Phys. Rev. Lett.* **99**, 187402 (2007).
- [21] E. B. Flagg, A. Muller, J. W. Robertson, S. Founta D. G. Deppe, M. Xiao, W. Ma, G. J. Salamo, and C. K. Shih, *Nature Phys.* **5**, 203 (2009).
- [22] J. P. Reithmaier, G. Sek, A. Löffler, C. Hofmann, S. Kuhn, S. Reitzenstein, L. V. Keldysh, V. D. Kulakovskii, T. L. Reinecke, and A. Forchel, *Nature* **432**, 197 (2004).
- [23] T. Yoshie, A. Scherer, J. Hendrickson, G. Khitrova, H. M. Gibbs, G. Rupper, C. Ell, O. B. Shchekin, and D. G. Deppe, *Nature* **432**, 200 (2004).
- [24] F. P. Laussy, E. Valle, und C. Tejedor, *Phys. Rev. Lett.* **101**, 083601 (2008).
- [25] J. Kasprzak, S. Reitzenstein, E. A. Muljarov, C. Kistner, C. Schneider, M. Strauss, S. Höfling, A. Forchel, and W. Langbein, *Nature Mat.* **9**, 304 (2010).
- [26] Y. Yamamoto, S. Machida, and O. Nilsson, *Phys. Rev. A* **34**, 4025 (1986).
- [27] J. Kim, S. Somani, and Y. Yamamoto, *Nonclassical Light from Semiconductor Lasers and LEDs* (Springer, Heidelberg, 2001).
- [28] M. Kira and S. W. Koch, *Semiconductor Quantum Optics* (Cambridge University Press, 2011)
- [29] W. Vogel and D.-G. Welsch, *Quantum Optics* (Wiley-VCH, Berlin, 2006).
- [30] J. Vaccaro and D. T. Pegg, *Phys. Rev. A* **49**, 4985 (1994).
- [31] B. Huttner and S. M. Barnett, *Europhys. Lett.* **18**, 487 (1992).
- [32] T. Gruner and D.-G. Welsch, *Phys. Rev. A* **53**, 1818 (1996).
- [33] E. Hanamura, *J. Phys. Soc. Jap.* **29**, 50 (1970).
- [34] J. M. Blatt, K. W. Böer, and W. Brandt, *Phys. Rev.* **126**, 1691 (1962).
- [35] R. Schwartz, N. Naka, F. Kieseling, and H. Stolz, *New J. Physics* **14**, 023054 (2012).

- [36] R. Zimmermann, *phys. stat. sol. (b)* **146**, 371 (1988).
- [37] L. Kappei, J. Szczytko, F. Morier-Genoud, and B. Deveaud, *Phys. Rev. Lett.* **94**, 147403 (2005)
- [38] H. Haug and S. W. Koch, *Quantum Theory of the Optical and Electronic Properties of Semiconductors*, (World Scientific Pub Co, 2009).
- [39] C. Cohen-Tannoudji, B. Diu, and F. Laloë, *Quantum Mechanics I* (Wiley, Paris, 1977).
- [40] E. Rebhan, *Theoretische Physik II* (Spektrum, München, 2005).
- [41] G. K. G. Burau, *Räumliche und spektrale Untersuchung der Resonanzfluoreszenz von Halbleiterstrukturen* (PhD-Thesis, Rostock, 2010).
- [42] G. J. Milburn and M. J. Woolley, *acta phys. slov.* **61**, 483 (2011).
- [43] E. M. Purcell, *Phys. Rev.* **69**, 681 (1946).
- [44] H. J. Carmichael, *Statistical Methods in Quantum Optics 2*, (Springer, Heidelberg, 2008).
- [45] T. Werlang, A. V. Dodonov, E. I. Duzzioni, and C. J. Villas-Bôas, *Phys. Rev. A* **78**, 053805 (2008).
- [46] A. L. Grimsmo and S. Parkins, *Phys. Rev. A* **87**, 033814 (2013).
- [47] H. Walther, B. T. H. Varcoe, B.-G. Englert and T. Becker, *Rep. Prog. Phys.* **69**, 1325 (2006).
- [48] H. J. Carmichael, *Phys. Rev. Lett.* **55**, 2790 (1985).
- [49] C. M. Savage, *Phys. Rev. Lett.* **60**, 1828 (1988).
- [50] H. J. Carmichael, R. J. Brecha, M.G. Raizen, H. J. Kimble and P. R. Rice, *Phys. Rev. A* **40**, 5516 (1989).
- [51] M. D. Lukin, S. F. Yelin and M. Fleischhauer, *Phys. Rev. Lett.* **84**, 4232 (2000).
- [52] C. DiFidio, W. Vogel, M. Khanbekyan, and D.-G. Welsch, *Phys. Rev. A* **77**, 043822 (2008).
- [53] J. Bochmann, M. Mücke, G. Langfahl-Klabes, C. Erbel, B. Weber, H. P. Specht, D. L. Moehring, and G. Rempe, *Phys. Rev. Lett.* **101**, 223601 (2008).

Bibliography

- [54] M. Brune, S. Haroche, V. Lefevre, J.M. Raimond, and N. Zagury, *Phys. Rev. Lett.* **65**, 976 (1990).
- [55] M. Brune, S. Haroche, J.M. Raimond, L. Davidovich, and N. Zagury, *Phys. Rev. A* **45**, 5193 (1992).
- [56] S. Haroche and J. M. Raimond, *Adv. in Atomic, Molecular and Optical Physics* **20**, 347 (1985).
- [57] D. Meschede, H. Walther and G. Müller, *Phys. Rev. Lett.* **54**, 551 (1985).
- [58] G. R. Guthöhrlein, M. Keller, K. Hayasaka, W. Lange and H. Walther, *Nature (London)* **414**, 49 (2001).
- [59] M. Keller, B. Lange, K. Hayasaka, W. Lange, and H. Walther, *J. Phys. B* **36**, 613 (2003).
- [60] M. Keller, B. Lange, K. Hayasaka, W. Lange and H. Walther, *Nature (London)* **431**, 1075 (2004)
- [61] T. Niemczyk, F. Deppe, H. Huebl, E. P. Menzel, F. Hocke, M. J. Schwarz, J. J. Garcia-Ripoll, D. Zueco, T. Hummer, E. Solano, A. marx, and R. Gross, *Nature Phys.* **6**, 772 (2010).
- [62] A. A. Anappara, S. De Liberato, A. Tredicucci, C. Ciuti, G. Biasiol, L. Sorba, and F. Beltram, *Phys. Rev. B* **79**, 201303 (2009).
- [63] P. Forn-Díaz, J. Lisenfeld, D. Marcos, J. J. García-Ripoll, E. Solano, C. J. P. M. Harmans, and J. E. Mooij, *Phys. Rev. Lett.* **105**, 237001 (2010).
- [64] E. Yablonovitch, *Phys. Rev. Lett.* **58**, 2059 (1987).
- [65] J. M. Gérard, D. Barrier, J. Y. Marzin, R. Kuszelewicz, L. Manin, E. Costard, V. Thierry-Mieg, and T. Rivera, *Appl. Phys. Lett.* **69**, 449 (1996).
- [66] A. Kiraz, P. Michler, C. Becher, B. Gayral, A. Imamoglu, L. Zhang, E. Hu, W. V. Schoenfeld, and P. M. Petroff, *Appl. Phys. Lett.* **78**, 3932 (2001).
- [67] S. Reitzenstein and A. Forchel, *J. Phys. D: Appl. Phys.* **43**, 033001 (2010).
- [68] K. Huang and A. Rhys, *Proc. R. Soc. Lond.* **A 204**, 406 (1950).
- [69] E. T. Jaynes and F. W. Cummings, *Proc. IEEE* **51**, 89 (1963).
- [70] B. W. Shore and P. L. Knight, *J. Mod. Opt.* **40**, 1195 (1993).

- [71] A. Majumdar, E. D. Kim, Y. Gong, M. Bajcsy, and J. Vučković, *Phys. Rev. B* **84**, 085309 (2011).
- [72] W.-S. Li and K.-D. Zhu, *Chin. Phys. Lett.* **20**, 1568 (2003)
- [73] D. P. S. McCutcheon and A. Nazir, *New J. Phys.* **12**, 113042 (2010).
- [74] V. Bužek, G. Drobný, M. S. Kim, G. Adam and P. L. Knight, *Phys. Rev. A* **56**, 2352 (1997).
- [75] C. Di Fidio, S. Maniscalco, W. Vogel, and A. Messina, *Phys. Rev. A* **65**, 033825 (2002).
- [76] G. J. Papadopoulos, *Phys. Rev. A* **37**, 2482 (1988).
- [77] H. T. Dung and A. S. Shumovsky, *Quantum Opt.* **4**, 85 (1992).
- [78] B. R. Mollow, *Phys. Rev. A* **5**, 2217 (1972).
- [79] R. Guccione-Gush and H. P. Gush, *Phys. Rev. A* **10**, 1474 (1974).
- [80] F. Y. Wu, S. Ezekiel, M. Ducloy, and B. R. Mollow, *Phys. Rev. Lett.* **38**, 1077 (1977).
- [81] P. Thomann, *J. Phys. B* **13**, 1111 (1980).
- [82] R. Short and L. Mandel, *Phys. Rev. Lett.* **51**, 384 (1983).
- [83] W. Vogel and D.-G. Welsch, *Phys. Rev. Lett.* **54**, 1802 (1985).
- [84] A. Heidman and S. Reynaud, *J. Physique* **46**, 1937 (1985).
- [85] M. D. Reid and D. F. Walls, *Phys. Rev. A* **32**, 396 (1985).
- [86] W. Vogel, *Phys. Rev. Lett.* **67**, 2450 (1991)
- [87] W. Vogel, *Phys. Rev. A* **51**, 4160 (1995).
- [88] E. Shchukin and W. Vogel, *Phys. Rev. Lett.* **96**, 200403 (2006).
- [89] S. Gerber, D. Rotter, L. Slodička, J. Eschner, H. J. Carmichael, and R. Blatt, *Phys. Rev. Lett.* **102**, 183601 (2009).
- [90] A. Ourjoumtsev, A. Kubanek, M. Koch, C. Sames, P.W.H. Pinske, G. Rempe, and K. Murr, *Nature* **474**, 623 (2011).
- [91] P. Bowles, M. Guță, and G. Adesso, *Phys. Rev. A* **84**, 022320 (2011).

Bibliography

- [92] G. Kießlich, G. Schaller, C. Emary, and T. Brandes, *Phys. Rev. Lett.* **107**, 050501 (2011).
- [93] R. Filip, *Phys. Rev. A* **65**, 062320 (2002).
- [94] A. K. Ekert, C. M. Alves, D. K. L. Oi, M. Horodecki, P. Horodecki, and L. C. Kwek, *Phys. Rev. Lett.* **88**, 217901 (2002).
- [95] H. Nakazato, T. Tanaka, K. Yuasa, G. Florio, and S. Pascazio, *Phys. Rev. A* **85**, 042316 (2012).
- [96] D. Valente, J. Suffczyński, T. Jakubczyk, A. Dousse, A. Lemaître, I. Sagnes, L. Lanco, P. Voisin, A. Auffèves, and P. Senellart, *preprint at arXiv:1307.6152 [quant-ph]* (2013).
- [97] H. Freedhoff and T. Quang, *J. Opt. Soc. Am. B* **10**, 1337 (1993).
- [98] T. Quang and H. Freedhoff, *Opt. Comm.* **107**, 480 (1994).
- [99] S. Hughes and H. J. Carmichael, *Phys. Rev. Lett.* **107**, 193601 (2011).
- [100] C. J. Hood, M. S. Chapman, T. W. Lynn, and H. J. Kimble, *Phys. Rev. Lett.* **80**, 4157 (1998).
- [101] A. Laucht, N. Hauke, J. M. Villas-Bôas, F. Hofbauer, G. Böhm, M. Kaniber, and J. J. Finley, *Phys. Rev. Lett.* **103**, 087405 (2009).
- [102] G. Khitrova, H. M. Gibbs, M. Kira, S. W. Koch, and A. Scherer, *Nature Phys.* **2**, 81 (2006).
- [103] S. Reitzenstein and A. Forchel, in *Cavity QED in Quantum Dot-Micropillar Cavity Systems*, edited by P. Michler, Single Semiconductor Quantum Dots, (Springer, Berlin, 2009).
- [104] T. Ahrens, G.K.G. Burau, H. Stolz, S. Reitzenstein, and A. Forchel, *phys. stat. sol. (c)* **8**, 1239 (2011).
- [105] Y. Aharonov, D. Falkoff, E. Lerner, and H. Pendleton, *Ann. Phys. (N.Y.)* **39**, 498 (1966).
- [106] Z.Y. Ou, C.K. Hong, and L. Mandel, *Phys. Rev. A* **36**, 192 (1987).
- [107] M. S. Kim, W. Son, V. Buzek, and P. L. Knight, *Phys. Rev. A* **65**, 032323 (2002).
- [108] Wang Xiang-bin, *Phys. Rev. A* **66**, 024303 (2002).

- [109] K.-Y. Cheng, Proc. of the IEEE **85**, 1694 (1997).
- [110] S. Eshlaghi, *GaAs/Al_xGa_{1-x}As Quantentöpfe: MBE-Wachstum, Charakterisierung und laterale Modulation fokussierter Ionenstrahlen* (PhD-thesis, Bochum, 2000).
- [111] D. Schwedt, C. Nacke, H. Stolz, S. Eshlaghi, S. Reuter, and A. Wieck, Phys. Rev. B **67**, 195303 (2003).
- [112] D. Schwedt, R. Schwartz, H. Stolz, D. Reuter, and A. Wieck, phys. stat. sol. (c) **3**, 2477 (2006).
- [113] D. Schwedt, *Räumlich und spektral hochaufgelöste Spektroskopie der Resonanzfluoreszenz an Exzitonen in ungeordneten Halbleiterquantenfilmen* (PhD-thesis, Rostock, 2006).
- [114] G. K. G. Burau, G. Manzke, F. Kieseling, H. Stolz, D. Reuter, and A. Wieck, J. Phys.: Conf. Ser. **210**, 012017 (2010).
- [115] O. Madelung, *Semiconductors: Data Handbook* (Springer, Berlin, 2003).
- [116] R. C. Miller, D. A. Kleinman, A. C. Gossard, and O. Munteanu, Phys. Rev. B **25**, 6545 (1982).
- [117] J. Hegarty, M. D Sturge, C. Weisbuch, A. C. Gossard, and W. Wiegmann, Phys. Rev. Lett. **49**, 930 (1982).
- [118] H. Stolz, D. Schwarze, W. von der Osten, and G. Weimann, Superlattices and Microstruct. **9**, 511 (1991).
- [119] H. Stolz, D. Schwarze, W. von der Osten, and G. Weimann, Phys. Rev. B **47**, 9669 (1993).
- [120] V. Savona, S. Haacke, and B. Deveaud, phys. stat. sol. (a) **178**, 21 (2000).
- [121] G. Kocherscheidt, W. Langbein, U. Woggon, V. Savona, R. Zimmermann, D. Reuter, and A. D. Wieck, Phys. Rev. B **68**, 085207 (2003).
- [122] J. Kasprzak, B. Patton, V. Savona, and W. Langbein, Nature Photon. **5**, 57 (2011).
- [123] G. Manzke, F. Richter, D. Semkat, G. K. G. Burau, F. Kieseling und H. Stolz, phys. stat. sol (c) **8**, 1161 (2011).
- [124] G. Manzke, D. Semkat, and H. Stolz, New J. Phys. **14**, 95002 (2012).

Bibliography

- [125] F. Richter, M. Florian, and K. Henneberger, *Phys. Rev. B* **78**, 205114 (2008).
- [126] M. Kira and S. W. Koch, *Phys. Rev. A* **78**, 022102 (2008).
- [127] T. Feldtmann, L. Schneebeli, M. Kira, and S. W. Koch, *Phys. Rev. B* **73**, 155319 (2006).
- [128] S. Chatterjee, C. Ell, S. Mosor, G. Khitrova, H. M. Gibbs, W. Hoyer, M. Kira, S.W. Koch, J. P. Prineas, and H. Stolz, *Phys. Rev. Lett.* **92**, 067402 (2004).
- [129] D. Vasylyev, W. Vogel, K. Henneberger, T. Schmielau, and D.-G. Welsch, *Phys. Rev. A* **78**, 033837 (2008).
- [130] F. Tassone and Y. Yamamoto, *Phys. Rev. B* **59**, 10830 (1999).
- [131] C. Ciuti, P. Schwendimann, and A. Quattropani, *Phys. Rev. B* **63**, 041303 (2001).
- [132] D. Pagel, H. Fehske, J. Sperling, and W. Vogel, *Phys. Rev. A* **86**, 052313 (2012).
- [133] R. H. Dicke, *Phys. Rev.* **93**, 99 (1954).
- [134] R. Bonifacio and L. A. Lugiato, *Phys. Rev. A* **11**, 1507 (1975).
- [135] E. Hanamura, Y. Kawabe, and A. Yamanaka, *Quantum Nonlinear Optics* (Springer, Heidelberg, 2007).
- [136] Y. D. Jho, X. Wang, D. H. Reitze, J. Kono, A. A. Belyanin, V. V. Kocharovsky, Vl. V. Kocharovsky, and G. S. Solomon, *Phys. Rev. B* **81**, 155314 (2010).
- [137] G. R. M. Robb, N. Piovella, A. Ferraro, R. Bonifacio, P. W. Courteille, and C. Zimmermann, *Phys. Rev. A* **69**, 041403(R) (2004).
- [138] N. Wiener, *Acta Mathematica* **55**, 117 (1930).
- [139] E. Shchukin, Th. Richter, and W. Vogel, *Phys. Rev. A* **71**, 011802(R) (2005).
- [140] A. Miranowicz, M. Bartkowiak, X. Wang, Y.-x. Liu, F. Nori, *Phys. Rev. A* **82**, 013824 (2010).
- [141] Y. X. Liu, C. Q. Cao, and H. Cao, *Phys. Rev. A* **61**, 023802 (2000).
- [142] W. Vogel, *Phys. Rev. Lett.* **100**, 013605 (2008).
- [143] E. Shchukin and W. Vogel, *Phys. Rev. Lett.* **95**, 230502 (2005).
- [144] A. Peres, *Phys. Rev. Lett.* **77**, 1413 (1996).

- [145] M. Horodecki, P. Horodecki, and R. Horodecki, *Phys. Lett. A* **223**, 1 (1996) .
- [146] E. Shchukin and W. Vogel, *Phys. Rev. A* **74**, 030302(R) (2006).
- [147] J. Häggblad, *Quantum Correlations of Broadband Light Fields* (Master-thesis, Luleå, 2007).
- [148] L. Knöll, W. Vogel, and D.-G. Welsch, *Phys. Rev. A* **36**, 3803 (1987).
- [149] L. Knöll, W. Vogel, and D.-G. Welsch, *Phys. Rev. A* **42**, 503 (1990).
- [150] U. Leonardt, *J. Mod. Opt.* **40**, 1123 (1993).